FABRICATION OF AMORPHOUS METAL MATRIX COMPOSITES BY SEVERE PLASTIC DEFORMATION

A Dissertation

by

SUVEEN NIGEL MATHAUDHU

Submitted to the Office of Graduate Studies of
Texas A&M University
in partial fulfillment of the requirements for the degree of

DOCTOR OF PHILOSOPHY

August 2006

Major Subject: Mechanical Engineering

FABRICATION OF AMORPHOUS METAL MATRIX COMPOSITES BY SEVERE PLASTIC DEFORMATION

A Dissertation

by

SUVEEN NIGEL MATHAUDHU

Submitted to the Office of Graduate Studies of
Texas A&M University
in partial fulfillment of the requirements for the degree of

DOCTOR OF PHILOSOPHY

Approved by:

Chair of Committee, K. Ted Hartwig
Committee Members, Richard Griffin
Harry Hogan
Thomas Pollock
Head of Department, Sai Lau

August 2006

Major Subject: Mechanical Engineering

ABSTRACT

Fabrication of Amorphous Metal Matrix Composites by Severe Plastic Deformation.
(August 2006)
Suveen Nigel Mathaudhu, B.S., Walla Walla College;
M.S., Texas A&M University
Chair of Advisory Committee: Dr. K. Ted Hartwig

Bulk metallic glasses (BMGs) have displayed impressive mechanical properties, but the use and dimensions of material have been limited due to critical cooling rate requirements and low ductility. The application of severe plastic deformation by equal channel angular extrusion (ECAE) for consolidation of bulk amorphous metals (BAM) and amorphous metal matrix composites (AMMC) is investigated in this dissertation. The objectives of this research are a) to better understand processing parameters which promote bonding between particles and b) to determine by what mechanisms the plasticity is enhanced in bulk amorphous metal matrix composites consolidated by ECAE.

To accomplish the objectives BAM and AMMCs were produced via ECAE consolidation of Vitreloy 106a ($Zr_{58.5}Nb_{2.8}Cu_{15.6}Ni_{12.8}Al_{10.3}$-wt%), ARLloy #1 ($Hf_{71.3}Cu_{16.2}Ni_{7.6}Ti_{2.2}Al_{2.6}$ -wt%), and both of these amorphous alloys blended with crystalline phases of W, Cu and Ni. Novel instrumented extrusions and a host of post-processing material characterizations were used to evaluate processing conditions and material properties. The results show that ECAE consolidation at temperatures within the supercooled liquid region gives near fully dense (>99%) and well bonded millimeter scale BAM and AMMCs. The mechanical properties of the ECAE processed BMG are comparable to cast material: $\sigma_f = 1640$ MPa, $\varepsilon_f = 2.3\%$, E = 80 GPa for consolidated Vitreloy 106a as compared to $\sigma_f = 1800$ MPa, $\varepsilon_f = 2.5\%$, E = 85 GPa for cast Vitreloy 106, and $\sigma_f = 1660$ MPa, $\varepsilon_f = 2.0\%$, E = 97 GPa for ARLloy #1 as compared to $\sigma_f = 2150$ MPa, $\varepsilon_f < 2.5\%$, E = 102 GPa for $Hf_{52}Cu_{17.9}Ni_{14.6}Ti_5Al_{10}$. The mechanical properties of AMMCs are substandard compared to those obtained from melt-infiltrated composites due to non-ideal particle bonding conditions such as surface oxides and crystalline phase morphology and chemistry. It is demonstrated that the addition of a dispersed crystalline phase to an amorphous matrix by ECAE powder consolidation increases the plasticity of the amorphous matrix by providing locations for generation and/or arrest of adiabatic shear bands. The ability of ECAE to consolidated BAM and AMMCs with improved plasticity opens the possibility of overcoming the size and plasticity limitations of the monolithic bulk metallic glasses.

DEDICATION

This dissertation is lovingly dedicated to my mother Veena and my brother Suneel. Thank you for all your patience and support. .

ACKNOWLEDGMENTS

A big debt of gratitude goes out to Dr. K. Ted Hartwig for his wonderful advisement, sharing of knowledge, and friendship during this dissertation. His guidance has more than adequately prepared me for a life of service. He has been far more then a mentor and advisor, and is much more like a family member to me. He is truly appreciated. Drs. Richard B. Griffin, Harry Hogan, and Thomas C. Pollock are also commended for their support and advice while on my advisory committee. Dr. David Claridge deserves special recognition for attracting me to and paving the way for me to get into Texas A&M for graduate studies. I will always be thankful to him for giving me an opportunity that I may not otherwise have had. I've been here eight years and there are so many people to thank, but as all of you know, I'm a procrastinator, and I have a few hours to get the rest of my dissertation done. So I know you'll forgive me when I say "Thank you all!" You know who you are…

TABLE OF CONTENTS

Page

CHAPTER Page

LIST OF FIGURES

FIGURE Page

FIGURE Page

FIGURE Page

FIGURE Page

FIGURE Page

FIGURE Page

FIGURE Page

LIST OF TABLES

CHAPTER I

INTRODUCTION

Bulk amorphous metals (BAM) have received increasing interest during recent years because they are promising for use in engineering applications. BAMs exhibit excellent wear properties, a low coefficient of friction, almost theoretical strength, a large elastic limit, and high corrosion resistance [1-5]. As an example, cast Vitreloy alloys (a zirconium based metallic glass) have been shown to have a strain rate insensitive yield stress of ~2000 MPa and an elastic strain limit of ~2% [6]. These values are very high when compared to the values of conventional “high strength” crystalline metals such as titanium alloys (Ti6Al-4V: ~ 750 MPa, 0.6%), aluminum alloys (Al7075: ~280 MPa, 0.65%) and stainless steel (17-4SS: ~830 MPa, 0.55%). It has also been demonstrated that some bulk metallic glasses behave in a ductile, viscous manner in the supercooled liquid region, i.e. between the glass transition temperature (T_g) and the crystallization temperature (T_x). This allows the use of forming and manufacturing processes normally reserved for polymers, such as compression or injection molding, to be employed for the first time for metallic glasses [7]. The result is that bulk amorphous metal alloys can be cast or formed into high quality, net shape parts [8,9]. Because of these unique properties, many possible applications exist for bulk amorphous materials, such as biomedical implants, engine components, blades in cutting tools, corrosion resistant vessels, industrial coatings, and sporting goods.

This dissertation follows the style and format of Materials Science and Engineering A.

There are two basic approaches for the manufacture of BAMs: solidification and consolidation. Solidification techniques include water quenching, copper mold casting, high pressure die casting and squeeze casting. The maximum thickness for rapidly solidified (cast) BAM is ~10 mm for Ln- and Mg-based alloys, ~30 mm in Zr- based, ~6 mm in Fe- based and ~75 mm in Pd-based metallic glasses [10].

Consolidation techniques include warm area reduction extrusion (ARE) [11-14], hot isostatic pressing (HIPing) [15-18] and warm equal channel angular extrusion (ECAE) [19-22], of amorphous alloy particulate. The production of bulk amorphous metals from consolidation of amorphous powders is theoretically not confined by a minimum dimension limited by the critical cooling rate (CCR). The CCR is the minimum cooling rate needed to circumvent crystallization when casting an amorphous alloy from melt. The consolidation of glassy alloy powders is promising because it offers the opportunity of larger cross-section defect free structural components and utilization of compositions that cannot be cast with cm-scale dimension. Metallic glass powders with extended supercooled liquid regions allow for consolidation of bulk glass samples by utilizing viscous flow in the temperature range (ΔT) between T_g (glass transition temperature) and T_x (crystallization temperature). This consolidation approach has been accomplished with a number of alloy systems including Zr- [23,24], Fe-[25], Cu-[26], Co-[27], Al-[19], and Ni- [28,29] based powders.

While bulk glass formers have demonstrated impressive mechanical properties for structural applications, such as high yield strengths (~2 GPa) and hardness, high elastic strain limits (~2%) [1-6], good plane strain fracture toughness (20-55 MPa $\sqrt{m}$) [30-32], and good wear and corrosion resistance, practical applications have been hindered by limited plastic deformation in compression loading (0%-2%) and no plastic deformation in tensile loading [33-35] at temperatures below the glass transition temperature. Most metallic glasses loaded uniaxially or under plane stress fail catastrophically on one dominant shear band [36]. This behavior is different from crystalline structural metal alloys, which have significant plastic deformation and yielding before failure. Multiple shear bands are observed when the catastrophic instability is avoided via mechanical constraint [37]. Although precise flow mechanisms are unclear, computational studies suggest that localized slip bands are associated with localized atomic shear-rearrangements correlated to regions of either excess free volume or extreme shear stress concentration [38]. In addition, easy crack initiation decreases the strength of amorphous alloys due to the lack of microstructure/phase that would serve as a barrier to nucleation and propagation of small cracks and shear bands [39]. Countering the deleterious effects of shear band propagation involves a keen understanding of amorphous metal deformation and failure mechanisms, but the deformation mechanisms of amorphous, partially crystallized amorphous and amorphous metal matrix composites and micromechanisms of shear band-crystalline particle interaction are not well studied or understood.

To address this gap in knowledge, this research will focus on development of strategies for stabilizing plastic flow and increasing fracture resistance with dispersed secondary crystalline phase additions. Also, the mechanisms by which the material plasticity are increased will be determined. The fabrication of the materials will be accomplished by using equal channel angular extrusion (ECAE) to consolidate blends of amorphous metal and crystalline phase powders into amorphous metal matrix composites (AMMCs). Warm ECAE is a powder consolidation method that we believe could successfully consolidate AMMCs into a bulk sample with sizes and properties equivalent to cast alloy. The ECAE technique involves subjecting the powder to simple shear under compression in a die containing intersecting channels [40-44]. The effects of high hydrostatic compressive stress and simple shear working together lead to effective consolidation. A significant benefit of ECAE is the uniformity of strain throughout the cross-section of processed material. Furthermore, the severe shear associated with ECAE (strain of 1.15 for a 90° extrusion) enables consolidation of powders at temperatures lower than those required for HIP consolidation. Other benefits of ECAE powder consolidation include:

1. Elimination of porosity without reduction in workpiece cross-section. Near theoretical density is achieved after a single or at most two extrusion passes.
2. Large product cross-sections should be possible. High length/diameter ratio products are possible.
3. Easy incorporation of second phase components (other powder, filamentary, or wire/rod dispersoids), which would not be suitable for incorporation during a melting step.
4. Lower press loads are needed than are required for area reduction extrusion.

The objective of the research will be to determine if the plasticity is enhanced in bulk amorphous metal matrix composites consolidated by severe plastic deformation, and if so, by what deformation mechanisms. To accomplish this objective, several tasks (sub-objectives) will be accomplished.

1. Establish which, if any, processing parameters promote strong bonding between the amorphous metal and crystalline phases.
2. Obtain consolidated composite samples with bulk sizes on the millimeter scale by warm severe plastic deformation.
3. Ascertain the mechanical properties of the consolidated composite with hardness testing and under compressive and tensile loading to determine whether the plasticity is enhanced, decreased or similar when compared to a monolithic cast amorphous alloy.
4. Determine or confirm the mechanisms of enhanced/decreased/similar plasticity in the bulk consolidated composite specimens.

It is hypothesized that enhanced plasticity will stem from formation of multiple shear bands initiated at the interface between the reinforcing phase and the metallic glass matrix, and their confinement within the AMMC. The improved ductility of an AMMC may open the possibility of overcoming the limited applications of the monolithic bulk metallic glasses that fail catastrophically with little plastic deformation.

CHAPTER II

LITERATURE REVIEW

2.1. Bulk Metallic Glasses (BMGs)

2.1.1. History of Metallic Glasses

In the past, structural materials have been composed almost exclusively of polycrystalline materials. These materials are characterized by grains containing ordered, periodic atomic structures. The use of such materials is driven by the fact that in nature, the crystalline phase is generally the equilibrium state (i.e. the lowest free energy) under ambient conditions, and therefore is the most practical for common usage. The amorphous solid phase of the material is often metastable or thermodynamically unstable, and is characterized by no long range atomic order. Metals and common alloys are poor glass formers, and until recently, it has been very difficult to isolate a stable, solid amorphous state in such materials. However, it has recently become possible to kinetically constrain the amorphous metal into a metastable or unstable state that may not crystallize for long periods of time.

The first published record of kinetically constrained metallic glass fabrication was published by Duwez et al. in 1960. By rapidly cooling (10^4-10^7 K/s) $Au_{75}Si_{25}$ from the liquid state, he was able to produce thin films of amorphous metallic materials, but even these were fairly unstable and incurred significant crystallization within 24 hr at ambient temperatures [45]. Because of the high cooling rates involved, only thin films and melt spun ribbons of binary and ternary metallic glass alloys, including some Fe-,Co-, Pd-, Ptand Ni-based amorphous systems could be produced for the next ~20 years. These amorphous metals had thickness dimensions generally less than 50 μm [46]. The cooling rate requirements and limited dimension were impediments to practical applications of these early amorphous metal alloys [47].

As mentioned in the introduction, significant progress has been made in selection of amorphous alloy compositions. Empirical rules [10,48] have been developed for obtaining new and more stable compositions which have led to the discovery of many compositions which solidify as a glass with critical cooling rates (CRRs) of 10^2 K/s or less. It is also observed that the glass-forming ability of alloys increases with an increased width of the supercooled liquid region ($\Delta T= T_g-T_x$) and decreasing T_g [10], where T_g is the glass transition temperature and T_x is the crystallization temperature. Zr- [49], Mg- [50], Ni- [51,52], Fe- [53] and Hf- [54,55] alloys have all been developed with low CCRs , but not all have significant ΔT regions (some less than 5 °C). Low CRR alloys have been labeled “bulk” glass formers or “bulk” metallic glasses (BMGs) because they can be solidified with millimeter-centimeter dimensions.

2.1.2. Bulk Metallic Glass Properties and Applications

Because of their unique structure, BMGs have a number of unusual mechanical, and physical properties that are significantly different from their crystalline counterparts. As mentioned in the introduction, some properties, such as high strength, high elastic strain limit, and high corrosion resistance [1-5, 55] make it a good candidate material for structural applications. Table 2.1 shows properties of the most characterized BMG ($Zr_{41.2}Ti_{13.8}Cu_{12.5}Ni_{10.0}Be_{22.5}$ – Vitreloy 1) compared to other high strength structural materials [56]. Currently, Liquidmetal Technologies (www.liquidmetal.com) is using this particular alloy for a number of innovative applications such as cell phone cases, luxury goods, sporting goods (skis, tennis racquets, baseball bats), and research applications for defense, medical and space applications.

Table 2.1

Selected properties of Vitreloy 1 and other structural engineering materials

Material	Yield Strength (GPa)	Elastic Strain Limit (%)	Young's Modulus (GPa)	Poisson's Ratio	Density (g/cm^3)	Coeff. of Thermal Expansion (10^{-6}/K)	Thermal Conductivity (W/cm-K)	Melting Point (K)
Vitreloy 1	1.93	2.0	93	0.387	6.11	10.1	0.035	993
Steel 1080	0.979	0.5	210	0.293	7.84	11.6@473K	0.381@673K	1753
Tungsten	---	---	345	0.280	19.3	4.5	1.74	3422
Ti-6Al-4V	0.890	0.8	114	0.361	4.43	9.3	---	---

2.1.3. Consolidation of Gas Atomized Powders as a BMG Fabrication Technique

As mentioned in the introduction there are two basic approaches for the manufacture of BMGs: solidification and consolidation. Researchers have recently incorporated both methods in series to produce BMGs by consolidation of gas atomized amorphous metal powder. The slow cooling rates (1-100 K/s) and high glass-forming ability of recently discovered "bulk" metallic glass systems have enabled the use of high pressure gas atomization (HPGA) for production of high quality amorphous alloy powders [57-60]. Advances in high-pressure gas atomization (HPGA) processing, such as convergent-divergent (C-D) rocket nozzle designs, have resulted in increased efficiency and particle uniformity [61], facilitating the increased application of HPGA for production of amorphous alloy powders. Limitations of the HPGA approach include unavoidable impurities and oxidation that initiate heterogeneous crystal nucleation on the particle surface. With decreasing particle size comes increased surface area, resulting in an increased surface oxide layer area that may be detrimental to further processing. Nevertheless, many amorphous systems have been successfully fabricated by HPGA including Co-based [18], Mg-based [50], Al-based [57], Nd-Fe-B [58], Ti-based [59], Ni-based [51,52] and Zr-based [20,21,60] alloys.

Applications of the HPGA produced amorphous metal powder include surface coatings [60] and consolidation into bulk samples [62]. One successful example of this consolidation approach consisted of the consolidation of gas atomized Cu-based amorphous alloy ($Cu_{47}Ti_{34}Zr_{11}Ni_8$) by area reduction extrusion (ARE) using reduction ratios of five, nine and 13 at a temperature (T_{ex} = 465ºC) slightly below the crystallization temperature (T_z ~480ºC) [26]. However, partial devitrification at the bottom of the billet occurred for R = 5, and full devitrification for R = 9 and 13. This loss of amorphous character is attributed to the extended time in the furnace hot zone at temperatures close to the crystallization temperature.

Another experiment demonstrated that Zr-based alloys could be consolidated to full density by ARE. This resulted in samples with mechanical properties similar to those of melt spun ribbons and cast alloys [23,24,63]. The bulk modulus did not vary significantly from the cast alloy (~80 GPa), and for reduction ratios of three or more, the tensile strength of the consolidate (1520 MPa) was higher than melt spun ribbons (1440 MPa) and slightly less than the monolithic cast alloy (1570 MPa). A significant supercooled liquid region (ΔT = 105ºC) and powder produced and consolidated in a closed-processing environment aided in overcoming the difficulties associated with particle-to-particle bonding and crystallization during extrusion.

These consolidates may be larger in scale than the corresponding cast alloy, and have similar mechanical properties. This addresses a significant benefit of the powder consolidation approach, which is that powders of amorphous alloy systems that cannot be cast with sufficient size for structural applications may be consolidated to produce material with the required dimensions. In addition, the powder consolidation approach can be used to fabricate amorphous metal matrix composites (AMMCs). It will be seen in a later section that a dispersion of second phase crystalline particles or wires reinforces an amorphous metal matrix and can improve mechanical properties, including ductility. To better address issues relating to the consolidation of AMMC's, it is necessary to discuss the nature and properties of basic particulate reinforced metal matrix composites.

2.2. Composite Theory

2.2.1. Classification and Types of Composites

Composite materials result when two or more materials or phases are used simultaneously in a heterogeneous structure to give properties that cannot be obtained by either alone. While composite structures have been used for many centuries, the development in recent decades has been rapid to meet the high performance and standards of modern engineered structures and machines. Common properties of composites such as high strength, ductility, fracture toughness, high temperature applications, hardness and conductivity (thermal or electrical), weight and cost have made their applications ubiquitous in all areas of engineering. To give the desired balance of properties to the composite, the properties, volume fractions, and geometries of the materials used must be carefully considered.

Composites are generally classified by either the matrix material (continuous phase), which can be metal, ceramic or polymer, or they can be classified by the geometry of the dispersed phase. For structural and mechanical applications particulate, fiber and laminar dispersed phases are common. The main difference between fiber and laminar reinforced composites and particle reinforced composites, is that the properties are generally isotropic in particulate reinforced composites if the dispersed particulates are uniformly distributed. The two former types of composites are almost always anisotropic, except in fiber reinforced composites where short fibers are dispersed homogeneously.

Of particular interest to this research project are metal matrix particulate reinforced composites. Generally, this type of composite consists of a metallic matrix surrounding a spherical discontinuous second phase. Unlike other composites, strengthening of the material is not the primary objective of such composites since the dispersed phase is too large to effectively block slip. Examples of common applications for metal matrix composites include tungsten carbide cutting tool inserts, which consist of a cobalt matrix surrounding WC particles, diamond saw abrasive cutting wheels and electrical contacts (silver matrix for conductivity with tungsten dispersed phase for wear resistance) [64].

Metal matrix composites can be fabricated by many different techniques, but they fall under three general categories: powder metallurgy, mechanical alloying and ingot metallurgy. The powder metallurgy approach involves the consolidation of a powder-form matrix with the dispersed phase at some given temperature and pressure. The consolidation can be performed and subsequently shaped by many common deformation processing methods such as extrusion, drawing, rolling and forging. Mechanical alloying employs the powder metallurgy approach to alloy powders fabricated in a high energy ball mill [65]. Ingot metallurgy is done by melting the matrix phase and mixing it with a reinforcement phase and casting it into the desired shape, or by vacuum infiltrating/injection molding the melted matrix material into a reinforcement preform.

2.2.2. Models for Property Determination in Particulate Reinforced Composites

For isotropic particulate composites, some properties can be predicted by a simple rule of mixtures, for example, the density of the composite can be predicted by the equation:

$$\rho_C = \sum \left(f_i \rho_i \right) = f_1 \rho_1 + f_2 \rho_2 + \cdots + f_n \rho_n \qquad (2.1)$$

where ρ_i is the density of the composite, $\rho_1, \rho_2, \ldots, \rho_n$ are the densities of each phase in the composite, and f_1, f_2,…, f_n are the volume fractions of each phase.

Another set of simplified equations, based on micromechanics and developed by Mital et al. [66], predicts thermal and mechanical properties in terms of constituent properties as well. These equations give the composite modulus to be:

$$E_{pc} = \frac{V_f^{0.67} E_b}{1 - V_f^{0.33} \left(1 - \frac{E_b}{E_p} \right)} + (1 - V_f^{0.67}) E_b \qquad (2.2)$$

where V_f is the volume fraction particles, and E_{pc}, E_b and E_p are the normal moduli of the particulate composite, binder (matrix) and particles, respectively. The shear modulus is given by a similar expression which substitutes G_{pc}, G_b and G_p for the normal moduli in Eq. 2.2. If the properties are assumed to be isotropic, the Poisson's ratio can be computed from the relationship:

$$v_{pc} = \frac{E_{pc} - 2G_{pc}}{2G_{pc}} \qquad (2.3)$$

The thermal properties of the particular composites can be estimated from analogous expressions. The coefficient of thermal expansion (α_{pc}) for instance is given by:

$$\alpha_{pc} = \tilde{\alpha} V_f^{0.67} \frac{\tilde{E}_p}{E_{pc}} + \alpha_b \frac{E_b}{E_{pc}} - \alpha_b V_f^{0.67} \frac{E_b}{E_{pc}} \qquad (2.4)$$

where $$\tilde{\alpha} = \alpha_b - V_f^{0.33} (\alpha_b - \alpha_p) \qquad (2.5)$$

and $$\tilde{E}_p = \frac{E_b}{1 - V_f^{0.33} \left(1 - \frac{E_b}{E_p} \right)} \qquad (2.6)$$

The thermal conductivity of the particulate composite (K_{pc}) can be approximated by substituting in the individual thermal conductivities of the components (K_b and K_p) into Eq. 2.2, and the heat capacity of the composite (C_{pc}) can be approximated by:

$$C_{pc} = \frac{1}{\rho_{pc}} \left(\rho_b \cdot \left(1 - V_f \right) C_b + \rho_p V_f C_p \right) \qquad (2.7)$$

where ρ and V_f are the densities and volume fractions of the particulate phase, respectively.

While these Eqs. 2.1 to 2.7 have been shown to predict properties fairly well, there are important assumptions implicit to their derivations. Some of these are:

1. The composite is composed of only two component phases: a matrix and a dispersed reinforcement phase.
2. The properties of the individual phases are isotropic.
3. The interface between the matrix and the dispersed reinforcement is a perfect bond.

The last assumption is an important one since interfacial debonding is one of the most prevalent damage and failure mechanisms in particle reinforced metal matrix composites. Since the behavior of the composite is so highly dependent on the nature of the composite interface and the bond strength between the matrix and the dispersed phase, the role of bonding at the composite interfaces will be discussed next.

2.2.3. Role of Composite Interface

An interface is described as "the region of significantly changed chemical composition that consititutes the bond between the matrix and reinforcement for transfer of loads between these members of the composite structure" [67]. In a composite, the nature and strength of this region is critical to the intended performance and applications of the material. In metal matrix composites the two major types of bonding that occur at the interface are mechanical and chemical.

A pure mechanical bond occurs without any chemical bonding being present and is a result of mechanical interlocking between the matrix and dispersed phase morphologies, or by frictional interactions from the contraction of the matrix on the reinforcement phase [68]. In situations where the coefficient of thermal expansion differs greatly between the matrix and dispersed phase, one component will reduce in size more than the other causing “gripping” on cooling from higher temperatures. This leads to some level of mechanical bonding even if there is no chemical bonding.

The first example of this phenomenon was demonstrated by Hill et al. who did longitudinal tensile test experiments with W wires in an aluminum matrix [69]. Different degrees of interlocking were obtained by using smooth, smooth and graphite coated, and etched and graphite coated W wires and vacuum infiltrating them with an aluminum matrix. The smooth wires resulted in a chemical bond between the W and Al and the composite had a high strength (95% theoretical). The graphite coating on the smooth wire prevented a chemical reaction from taking place, so there was little, if any chemical bonding, and no mechanical bonding. This composite had poor strength (35% theoretical). The last case, which was the etched and graphite coated wires, showed no chemical bonding, but an interlocking effect from the etching and the strength was near that produced by the chemical bond alone (91% theoretical).

A chemical bond in metal matrix composites will involve atomic diffusion between the matrix and the dispersed phase. Therefore a chemical bond forms by the formation of some sort of solid solution compound or chemical compound at the reaction zone. The diffusion can be determined from the well known relationship for a planar interface:

$$x^2 = Dt \qquad (2.8)$$

where x is the thickness of the reaction zone, D is the diffusivity, and t is the time. The diffusivity is exponentially dependant on temperature:

$$D = D_0 e^{(-\Delta Q / kT)} \qquad (2.9)$$

where D_o is a constant, ΔQ is the activation energy, k is Boltzmann's constant ($1.3806503 \times 10^{-23}$ m^2 kg s^{-2} K^{-1}) and T is the temperature in Kelvin units. A factor that significantly affects the nature of the diffusion bond is the presences and thickness of impurities, such as an oxide coating on the surface of either composite phase. The high temperature resistance of an oxide layer prevents easy diffusion between two otherwise clean surfaces. The optimum bond strength is not achieved for this circumstance.

2.3. Metallic Glass Composites

2.3.1. Strength and Ductility Issues in BMGs

Bulk metallic glasses have shown limited plastic deformation in compression loading (0%-2%) and no plastic deformation in tensile loading [33-35] at temperatures below the glass transition temperature. This is different from conventional crystalline metals which show plastic deformation and yielding before failure. Indeed, the extreme slip instability and near-theoretical strengths of amorphous metals indicate that the deformation mechanisms for amorphous metals are much different than those of polycrystalline metals. The brittle failure of amorphous metals can be attributed to the rapid propagation of a localized shear band across the cross-section of the sample. This type of failure is evident from a typical fracture surface which shows a vein-like morphology and other evidence of localized melting during fracture. Existing theories such as Taylor instabilities [36], crack-tip softening due to adiabatic heating and strain softening explain the vein-like pattern development seen along the shear bands [37].

The most prevalent method of enhancing the plasticity has been the incorporation or nucleation of a crystalline second phase in the amorphous matrix. The development of these types of composites is aimed at providing enhanced plastic deformation in structural amorphous metals at temperatures below the glass transition temperature (T_g). Enhanced plasticity stems from formation of multiple shear bands initiated at the interface between the reinforcing phase and the metallic glass matrix, and their confinement within the amorphous metal matrix of the composite. Improved ductility may open the possibility of overcoming the limited applications of the monolithic bulk metallic glasses that fail catastrophically with little plastic deformation.

2.3.2. Composite Fabrication Techniques

With the understanding that second phase crystalline particles embedded in an amorphous matrix can lead to an increase in fracture stress and ductility compared to the homogeneous amorphous alloy due to the suppression of shear band propagation by these particles [13,70], researchers have devised a number of different methods for introducing secondary phases into an amorphous metal matrix. Some of the more common methods are precipitation of a secondary micro- or nanocrystalline phase through partial devitrification [14,71], addition of particles to a melt before casting [72-74], melt infiltration casting around a porous preform [75,76], mechanical alloying [77] followed by HIPing, consolidation of amorphous and crystalline powder blends [28], and atomization and subsequent consolidation of composite powders [60].

Efforts to reinforce Zr-based Vitreloy 106 were attempted by the addition of less than 20 vol.% WC, SiC, Ta and W particles [73,74]. These secondary phases were selected based on their limited reactivity with the amorphous matrix, similar thermal expansion coefficients, and the possibility of toughening and improving the fatigue properties of the material. Compression test results indicated that a 10 vol.% addition of W, WC, or Ta secondary phase increases the inelastic deformation from 0.5% in pure Vitreloy 106 to 3-7% in the composite. The compressive strength increased from 1.82GPa with no reinforcement to 1.96 GPa with 15 vol% W added.

The addition of a crystalline fiber phase to amorphous metallic matrix has been recently accomplished. Two examples are W-fibers (up to 80 vol.%) in Zr-based amorphous alloy [75,76] and brass fibers (up to 40 vol.%) formed by warm extrusion consolidation with Ni-based amorphous alloy [28]. For the Vitreloy 106 – W AMMC, the mechanical properties of the reinforced composite, as compared to the monolithic alloy, was significantly improved with the total strain to failure increasing by a factor of six (2.5% vs. 16.2%, respectively). The compressive strength increased significantly (~1800 MPa vs. ~2150 MPa, respectively) as did the elastic modulus (85GPa to 320GPa) [75,76]. The results correlate well with the rule-of-mixtures, indicating good wire-matrix bond strength.

Full density in an amorphous Ni-based/ 40 vol% brass consolidated composite with no devitrification of the amorphous matrix ($Ni_{59}Zr_{20}Ti_{16}Si_2Sn_3$) illustrates the successful application of area reduction extrusion for AMMC fabrication [28]. In the amorphous Ni-based brass composite some cracks were observed at the phase boundaries. The amorphous Ni-based alloy / brass composite demonstrated decreased strength and elastic moduli because of the lower properties of the brass reinforcement, but showed increased plasticity. It is hypothesized by the authors that closed processing would result in better particle-to-particle bonding, and properties would improve. This last example points to a key advantage of consolidation by extrusion for the fabrication of AMMCs. Consolidation can produce composites containing a dispersed particulate crystalline phase which may be difficult to produce by casting methods due to problems associated with particle solubility, density differences, and heterogeneous nucleation of crystalline phases from the undercooled liquid on particle surfaces.

In all cases, the crystalline particles effectively present a barrier to localized shear deformation of the amorphous matrix and provide additional ductility and/or strengthening. The increased plasticity and strengthening is attributed to multiple shear band interactions initiating at the crystal phase/amorphous matrix boundary, and confinement and interference of shear bands within the amorphous matrix.

2.4. Severe Plastic Deformation for Powder Consolidation

2.4.1. Conventional Powder Consolidation

Powder metallurgy (P/M) is a powerful tool used to consolidate metallic or ceramic powders into products of a given shape. Typical steps involved in powder metallurgy are powder production, compaction of the powders into a form, and sintering, which requires heating the compacted powder to a temperature at which the powder particles inter-diffuse and the required properties are produced [78]. Powder consolidation has the benefits of being environmentally clean, it conserves material, is not energy or labor intensive and the materials have reproducible properties. Some typical consolidation techniques are conventional powder extrusion, hot isostatic pressing (HIP), shock-wave consolidation, and powder injection molding (PIM).

Many limitations exist with conventional P/M compaction methods. Conventional extrusion requires high pressures and often imposes nonuniform deformation on the workpiece, and the machinery and tooling to exert such high pressures can be expensive. Many of the limitations involved with area reduction extrusion stem from the need for substantial extrusion ratios (>20) to achieve good interparticle bonding. Amorphous powder enclosed in large cross-sectional areas must be uniformly heated for properties and consolidation to be uniform through the consolidated sample. Even with uniform heating, non-uniform deformation may cause nonhomogenous flow and regional devitrification in consolidated samples.

HIPing requires high temperatures for long times that may alter microstructural properties and outweigh the benefits of the materials produced. These two processes also do not impart significant material shear strain helpful for breaking up surface oxides and contamination and for the bonding of certain powders. HIPing is limited in its ability to achieve adequate particle-to-particle bonding, remove all void space and accomplish full density without devitrification. Mechanical properties comparable to cast alloys are difficult to achieve in HIP consolidated amorphous metals.

2.4.2. Powder Consolidation by ECAE

Equal channel angular extrusion (ECAE) is a severe plastic deformation processing method that may be used to overcome some of the limitations of conventional consolidation methods. The ECAE process applies uniform simple shear to impart a large amount of plastic strain to bulk material as it is passed through a die containing two intersecting channels [41,79,80]. Advantages are: little change in the geometry of the workpiece, uniform plastic strain, relatively low extrusion loads, unlimited strain space, alternative product microstructures and textures, and relatively simple but elegant tooling. Further details concerning the ECAE process can be found in other publications [41,79,80].

It is believed that ECAE effectively consolidates powders as a result of the high hydrostatic compressive stress and simple shear working together. The extrusions can be performed over a wide range of temperatures, and with multiple passes if necessary. Benefits of ECAE for powder consolidation are expected to include: small heated cross-section (good heat transfer conditions) relative to conventional extrusion, large product cross-sections with uniform properties, and elimination of porosity without reduction in cross-section.

Work on ECAE consolidation of powders began in 1995 at Texas A&M University and continues today as an alternate method of powder consolidation. Full theoretical density from 6061 Al powder is achieved after at most two warm extrusions through a 90° tool. The tensile strength of the ECAE consolidated aluminum is comparable to that of wrought material [81]. Other materials successfully consolidated using ECAE have included Cu blended with Ag, Sn-8Cu blended with Al_2O_3 and SiO_2 [82], NbFeB blended with 304 stainless steel or pure Cu, WC blended with Co [83,84], micro- and nano-crystalline Cu [85], microcrystalline SS and amorphous Cu- and Zr-based alloys [20,21]. The consolidation of $Cu_{50}Ti_{32}Zr_{12}Ni_5Si_1$ (Vitreloy 102) metallic glass powders with ECAE resulted in bulk samples with largely amorphous character and a supercooled liquid region slightly narrower than that of initial powder [20]. The change in the supercooled liquid region, as well as the increase in hardness and brittleness after consolidation, was attributed to the high oxygen content of initial powder (>2000 ppmw) and crossing the time-temperature-transformation (crystallization) boundary during processing leading to partial devitrification. Preliminary work on high oxygen (1280 ppm O_2) Vitreloy 106a ($Zr_{58.5}Nb_{2.8}Cu_{15.6}Ni_{12.8}Al_{10.3}$ encapsulated in Cu cans showed good bonding and mechanical properties comparable to cast amorphous alloy (~1.6 GPa) [26]. These consolidates showed vein-like patterns on the fracture surfaces and exhibited only a small amount of nanocrystallization during the extrusion These experiments foretell the ability of ECAE to consolidate amorphous powder and will lead into the work performed for this research project.

CHAPTER III

EXPERIMENTAL SETUP AND PROCEDURES

3.1 Materials

3.1.1 Selection of Amorphous Alloy Compositions

For this study, two amorphous alloys were selected for examination: a Zr-based alloy ($Zr_{58.5}Nb_{2.8}Cu_{15.6}Ni_{12.8}Al_{10.3}$ -wt% - also known as Vitreloy 106a) and a Hf-based amorphous alloy ($Hf_{71.3}Cu_{16.2}Ni_{7.6}Ti_{2.2}Al_{2.6}$ -wt% - also known as ARLloy #1). As presented in the previous chapter, Zr-based alloys have typically been the most extensively researched amorphous alloys, while Hf-based alloys are relatively new and have not been significantly investigated. These powders were chosen based on a number of factors, most significantly the low glass transition temperature and the wide supercooled liquid region, which are necessary for the powder to remain predominatly amorphous during powder consolidation. All amorphous powders were fabricated at the Materials Processing Center of the Ames Laboratory (US DOE) by high pressure gas atomization (HPGA).

Two batches of Zr-based powder were fabricated by HPGA. The first batch of powder (Batch 1) was made from cast ingots containing ~950 ppmw oxygen. The second batch (Batch 2) was made from cast Vit106a buttons made by arc-melting pure elements, including low oxygen “crystal bar” Zr. The HPGA involved melting in graphite crucibles and Ar gas atomization. Inert gas fusion analysis shows the oxygen content of the Batch 1 powder to be approximately 1280 ppmw and the Batch 2 powder to be approximately 780 ppmw. The atomized amorphous particles were screened to obtain large particles (38μm-150μm) for the experiments (Figure 3.1). The larger particles minimize the total surface area of oxygen on the surface of the particles.

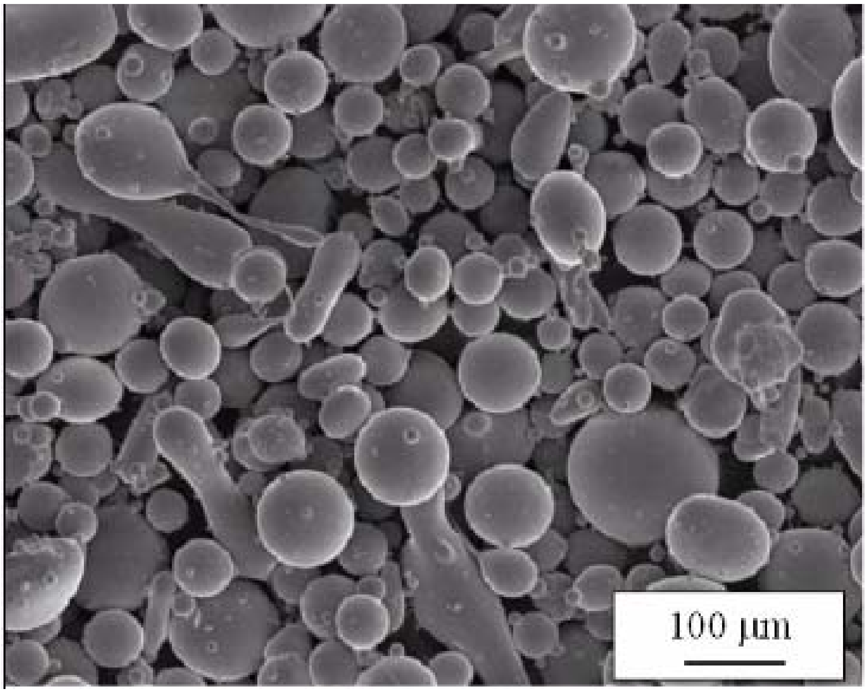

Figure 3.1 SEM image of batch 2 Vitreloy 106a. The spherical Vitreloy 106a powder ranges between 38μm - 150μm in diameter.

The amorphous Hf alloy was prepared by triple arc melting with 99.95% purity elements using crystal bar Hf from Wah Chang, Inc. The pre-alloyed buttons (50 grams each) were placed in a fine grain graphite crucible, remelted in an argon atmosphere and atomized at 1600°C using argon gas at 950 psi. The powder was handled in air. The oxygen content of the arc melt buttons was found to be ~65 ppmw oxygen. Oxygen and carbon and nitrogen content of the powder were found to be 459 ppmw, 163 ppmw, and

22 ppmw, respectively. These powders were also screened to obtain sizes suitable for consolidation experiments (-100/+325 Mesh 45-106 μm powder size) (Figure 3.2).

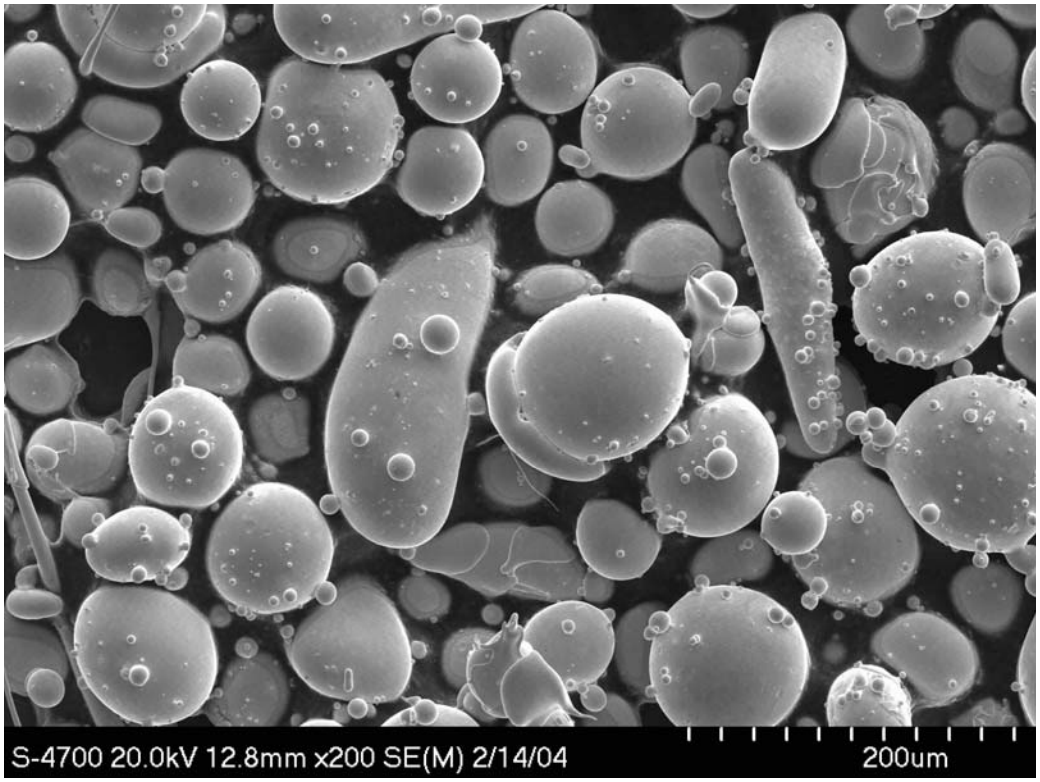

Figure 3.2 SEM image of HPGA ARLloy #1 powder. The spherical ARLloy #1 powder ranges between 45μm - 106μm in diameter.

3.1.2. Selection of Crystalline Reinforcement Phase

To investigate the fabrication of AMMC's three different elemental crystalline phases were selected: pure W, Cu and Ni. The initial material chosen was elemental tungsten. This material was selected due to the density requirements required by the initial project sponsor (DARPA-ARO) for kinetic energy penetrator applications. Cu and Ni were selected because they are known to bond with a variety of materials by powder metallurgy, and they were available at no cost from DOE Ames Laboratory. The initial W powder particles were supplied by Army Research Laboratory (Aberdeen, MD). This powder was composed of large particles, but they were contaminated by a nanoscale oxide surface later which, as will be shown later, proved to be detrimental to bonding (Figure 3.3).

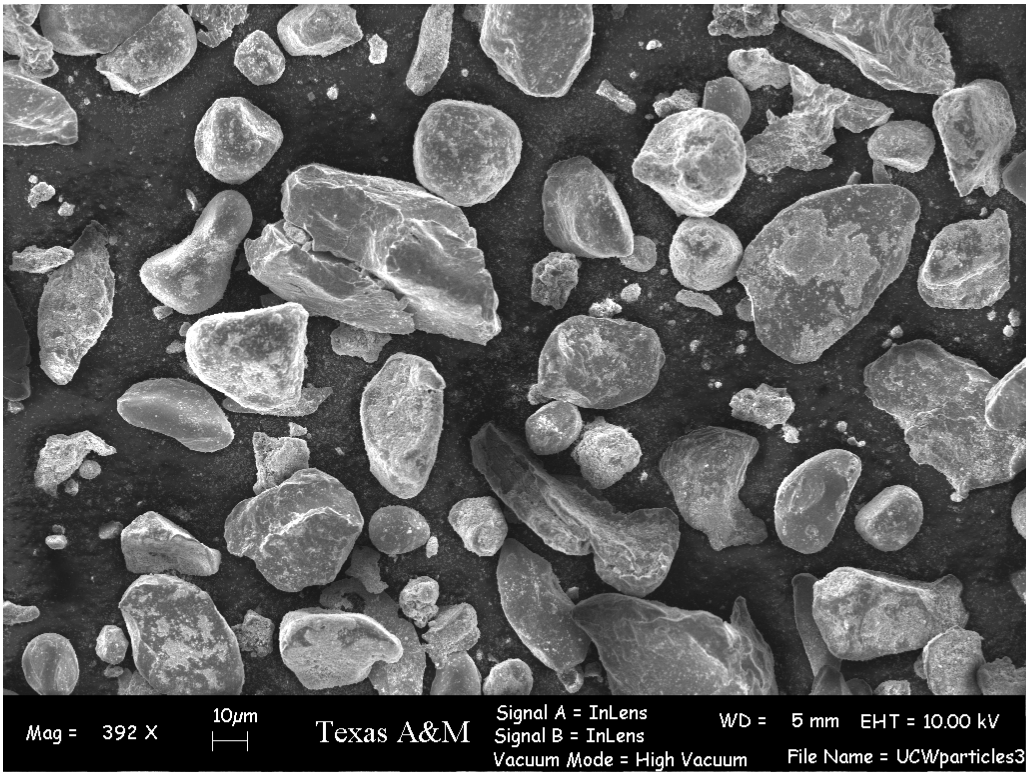

Figure 3.3 SEM image of W powder provided by Army Research Laboratory. Notice the oxide layer / contamination coating the surface of some particles.

A second batch of 99.98% pure W was provided by the Army Research Laboratory. This 99.98% pure W powder used was composed of 5-10 μm particles in 38 μm – 53 μm agglomerates (Figure 3.4) and the particles were coated with Ni in hopes of improving the bonds between W particles and W particles and the amorphous metal. The agglomerated W provided better results than the scale coated W, but bonding was still a problem. Suitable W powder, which had a minimal amount of agglomerates and no visible surface scale was provided by Alldyne, and used for subsequent experiments (Figure 3.5). The particle size of the 99.98% pure Alldyne W was -100/+325 mesh (45μm – 106μm). Pure Cu and Ni powders were obtained from commercial suppliers to test the consolidation characteristics of other crystalline phases with the amorphous particulates. Both the Cu and Ni powders were screened to -100/+325 mesh as well.

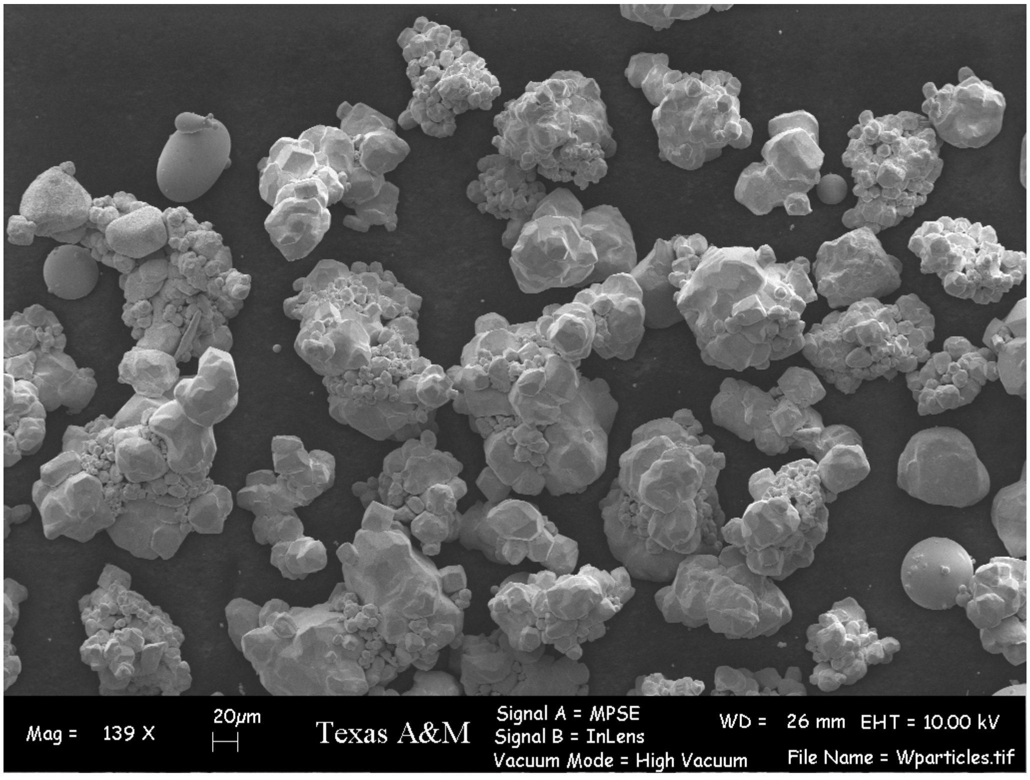

Figure 3.4 SEM image of Ni-coated W powder provided by Army Research Laboratory. The coating process likely results in the W particles agglomerating.

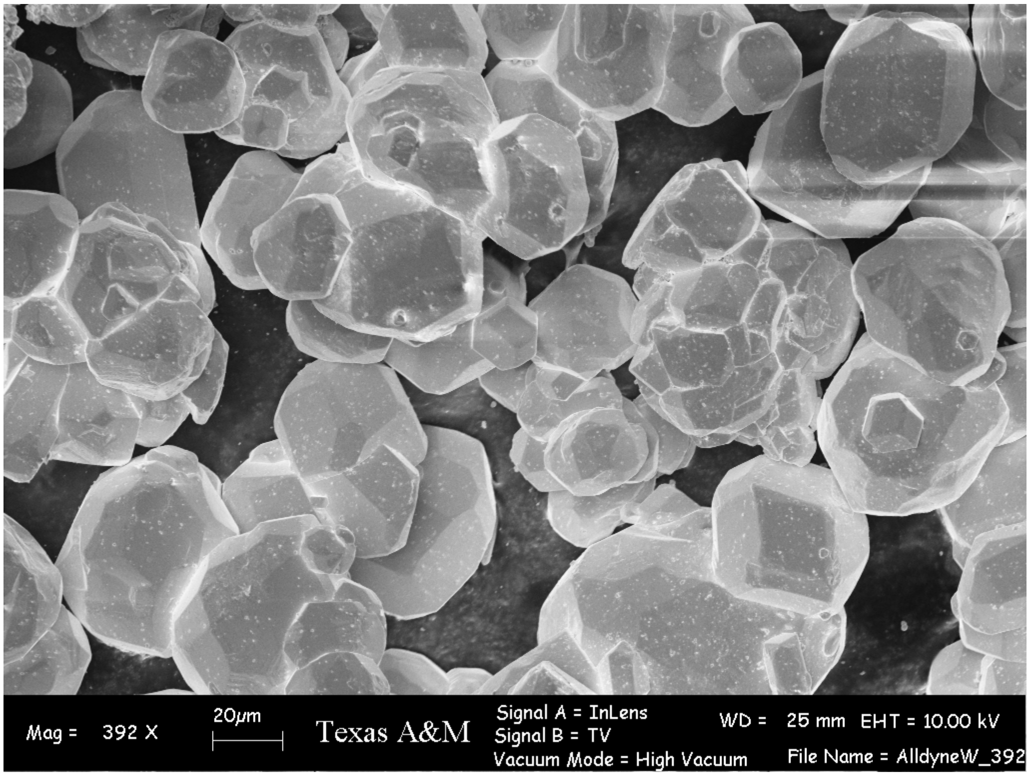

Figure 3.5 SEM image of clean W powder purchased from Alldyne.

3.2 ECAE Procedures

3.2.1. Tooling Characteristics

Two ECAE tools were built to perform the extrusions in this study. Both tools contained a 90° angle between the inlet and outlet channels, incorporated sliding side walls in the inlet channel, a bottom slider in the exit channel, and heater cartridges/bands to heat the tooling to the temperatures necessary for extrusions in the supercooled liquid regions of the amorphous powder phase. The first tool was constructed to extrude square billets with 19 mm x 19 mm cross-sections. The second tool accomodated 25 mm diameter cylindrical billets and used the "inlet channel slider" design.

3.2.2. Canning of the Materials and Instrumentation

The powders are placed uncompacted in Ni, Cu or Monel cans, vacuum outgassed at 150°C for 8 hrs, and electron beam welded shut. The can geometries and cavity sizes vary and will be given in a later section. In all cases, the cans were instrumented with one or two thermocouples approximately 10 mm from the top and bottom of the billets (Figure 3.6). The one at the bottom of the billet is under the powder chamber with leads coming out the tooling exit channel. The other is at the "top" of the can with leads entering from the tool punch. These thermocouples allowed the measurement of approximate time it takes for the powder to achieve a temperature suitable for extrusion, the adiabatic temperature rise during extrusion, and the time the billet is in a particular temperature range.

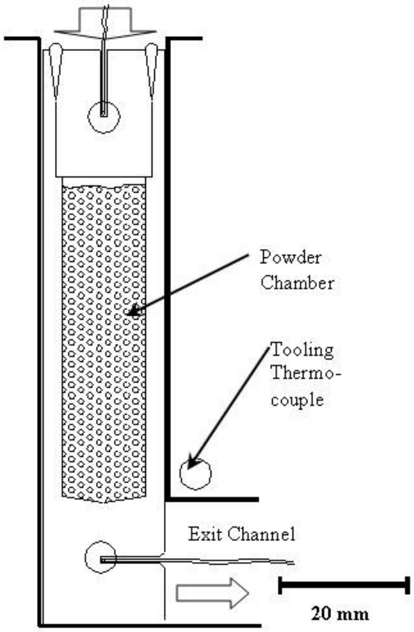

Figure 3.6 Schematic diagram of ECAE billet geometry, tooling and thermocouple positions in billet and tooling (indicated by circles on the diagram).

3.2.3. Extrusion Parameters

The main factors affecting the time and temperature available for extrusion are the broadness of the ΔT region (T_x - T_g) and time-temperature-transformation (TTT) behavior of the amorphous powder. The ΔT region determines the general temperature range that extrusions can be performed at while the TTT boundary establishes how much time is available at a particular temperature within that range before a crystallization event begins to occur. The determination and optimization of the time and temperatures needed for effective consolidation of the amorphous powders and composites required significant time and effort. As such, the procedures and results leading to how these parameters were obtained are given in the EXPERIMENTAL RESULTS section of the dissertation.

The time available for extrusion, combined with the can length, determine how fast the extrusion should be performed, e.g. the punch speed during extrusion. If enough time is available, multiple extrusions can be performed. In this study, up to two extrusions were performed according to ECAE route 2A (0° rotation before the second extrusion), route 2B (90° rotation before the second extrusion) or route 2C (180° rotation before the second extrusion). Tables giving the extrusion conditions for each billet will be given in the EXPERIMENTAL RESULTS section as well.

3.3. Thermal Characterization

3.3.1. Differential Scanning Calorimetry

Differential scanning calorimetry (DSC) analysis with a Perkin-Elmer Pyris 1 DSC was used to establish the range of undercooled liquid stability and to determine the temperature-time transformation (TTT) boundary beyond which crystallization is evident. The TTT boundary was determined by heating the amorphous powder at 20°C/min or 40°C/min to a temperature at or above T_g and then holding at a set temperature. The time to the first exothermic peak on the DSC trace (onset of crystallization) was measured at each set temperature and used to define the TTT boundary. Further details of this process will be given in the next chapter. DSC was also used to take measurements on the post-extruded specimens for changes in the glass transition and crystallization temperatures, and devitrification as evidenced by a decrease in the enthalpy of crystallization.

3.4. Microstructural Characterization

3.4.1. X-Ray Diffraction (XRD)

X-ray diffraction can be used to obtain a quantitative measurement of devitrification in the consolidated/processed amorphous powders when compared with the trace of the starting atomized amorphous powder. A Bruker-AXS D8 diffractometer was used with CuKα radiation ($\lambda = 0.1542$ nm) to examine the starting powders and ground particulates prepared from the consolidated samples. A θ-2θ goniometer configuration was used to scan over a 2θ range from 10° to 60°.

3.4.2. Light Microscopy

Light microscopy is a valuable tool for examining the consolidated microstructures. This tool was used to examine microstructures on the flow plane of the consolidated samples for porosity, uniformity of particle deformation (on etched samples), level of particle deformation (aspect ratio) and adiabatic shear banding from microhardness indents. Light microscopy was also used to examine the flow plane of fractured tensile test samples to observe whether fractures occurred primarily along prior particle boundaries or through particles. Etch to reveal the prior particle boundaries, the samples were swabbed with a solution of 10 vol% HF and 90 vol% distilled water for 3 s at room temperature, and rinsed/dryed. All light microscopy was done using a Leica MEF4M stereo wide-field metallograph equipped with a Leica DC200 digital camera and polarizing filter.

3.4.3. Scanning Electron Microscopy (SEM)

Microstructural analysis of the starting powders and the consolidated tension/compression sample fracture surfaces was performed with scanning electron microscopy (SEM). With this tool, high-resolution images with a depth-of-field not obtainable from standard light microscopy can be obtained from the nanoscale to the microscale. All samples were examined using a Zeiss 1530 VP FE-SEM scanning electron microscope operating at 10kV. Back-scattered electron (BSE) imaging was used on fracture surfaces. With BSE imaging, elements with a higher atomic number (or in the case of an amorphous alloy, average atomic number) appear darker, and therefore, contrast can be used to differentiate particular phases in the consolidated composites. SEM is also used to investigate deformation zones and shear bands present on bulk consolidated samples after Vickers microhardness indentations.

3.5 Material/Mechanical Property Characterization

3.5.1. Microhardness Measurement

Vickers microhardness measurements were performed with a Beuhler Microment II using loads from 300g - 1000g for ~13 seconds on the polished samples. Ten measurements were taken randomly on the flow plane (billet side plane) of the samples and averaged for each specimen. Hardness values will be reported using the following notation: 150 HV_{300}, where the first number is the microhardness, HV indicates the Vickers test, and the subscript indicates the load in grams used. For this study, the Vickers microhardness provides a way of evaluating not just the hardness, but the retention of amorphous character, particle-to-particle bond strength and shear band interactions.

3.5.2. Tension/Compression Testing

Mechanical testing is essential for determining the particle-to-particle bond strength and mechanical properties of the consolidated samples. Tension and compression testing was performed on electrodischarge machined (EDM) samples with an MTS testing machine at a strain rate of 10^{-4} s^{-1} at room temperature. Tension samples had gage sections of 1.5 mm × 3 mm × 8 mm. The compression samples were 6 mm long and 3 mm dia. or 2 mm x 2mm x 4mm.

CHAPTER IV

EXPERIMENTAL RESULTS

4.1 Amorphous Alloy Selection and Characterization

4.1.1. Determination of the Supercooled Liquid Region

To consolidate the amorphous powder effectively, it is necessary to find the temperature region in which it will behave viscously. This undercooled liquid region of stability ($\Delta T = T_x - T_g$) was determined for each amorphous alloy by DSC of the starting powder at a rate of 40K/min over a temperature range of 100°C to 600°C. The 40K/min heating rate was selected based on the fact that it more accurately represents the heating rate of the powder containing billet when heated in the ECAE tooling and extruded. Figure 4.1 shows the plots for both Vitreloy 106a powders and the ARLloy #1. From these plots, the T_g and T_x values are obtained, and are given in Table 4.1.

For the case of the ARLloy #1, the glass transition temperature is not clear from the DSC plot, so data was extracted from DTA results obtained at a heating rate of 10K/min by Ames Laboratories. These results showed the undercooled liquid temperature range (~ 48°C) is independent of heating rate, so 48 degrees were subtracted from the T_x value to approximate the T_g. Both batches of Vitreloy 106a have the same composition, with the only difference being the oxygen content (1280 ppmw vs. 760 ppmw). It seems that a decrease in oxygen corresponds to a wider ΔT region. Also, the ΔT region for the ARLloy #1 is the same as the batch 2 powder, but the T_g and T_x temperatures are much higher corresponding to the higher melting temperature of Hf (2207 - 2247 °C) as compared to Zr (1852°C).

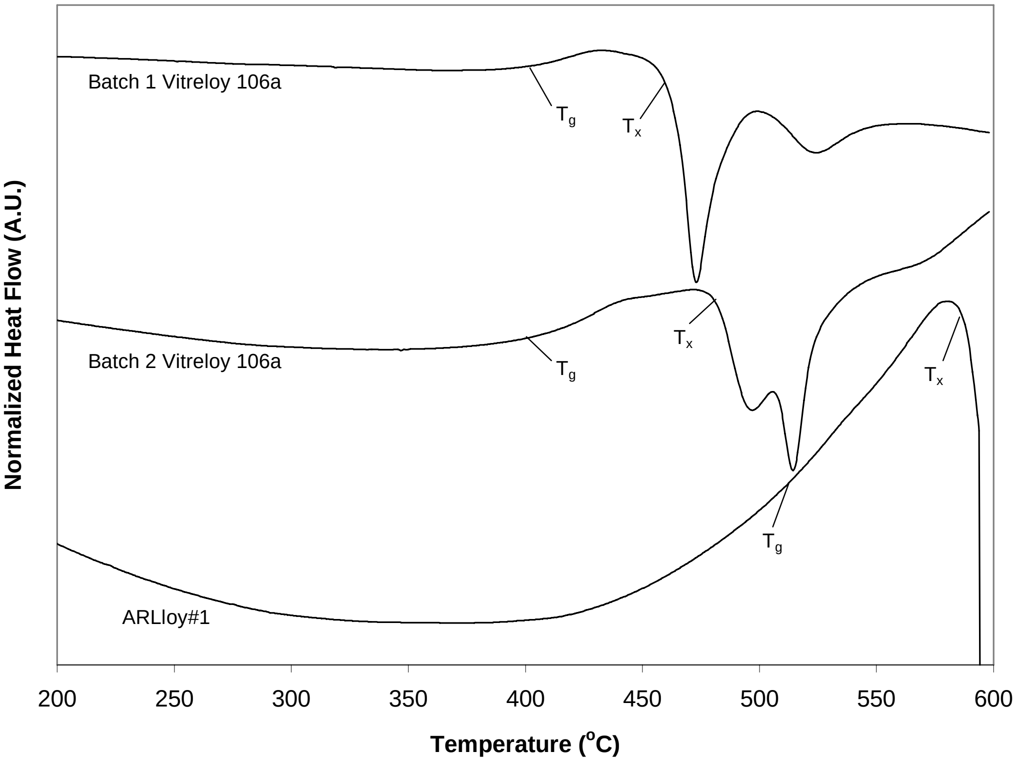

Figure 4.1 DSC traces (at 40K/min) of two runs of HPGA atomized Vitreloy 106a powder (Batch 1 with 1280 ppm O_2 and Batch 2 with 760 ppm O_2), and one run of HPGA atomized ARLloy #1 powder. These DSC traces are used to determine the T_g and T_x values (i.e. the supercooled liquid region each amorphous alloy.

Table 4.1 Undercooled liquid region for Zr- and Hf- based amorphous alloys

Amorphous Alloy	T_g (°C)	T_x (°C)	ΔT
Vitreloy 106a Batch 1	400	460	60
Vitreloy 106a Batch 2	400	480	80
ARLloy #1	520	580	60

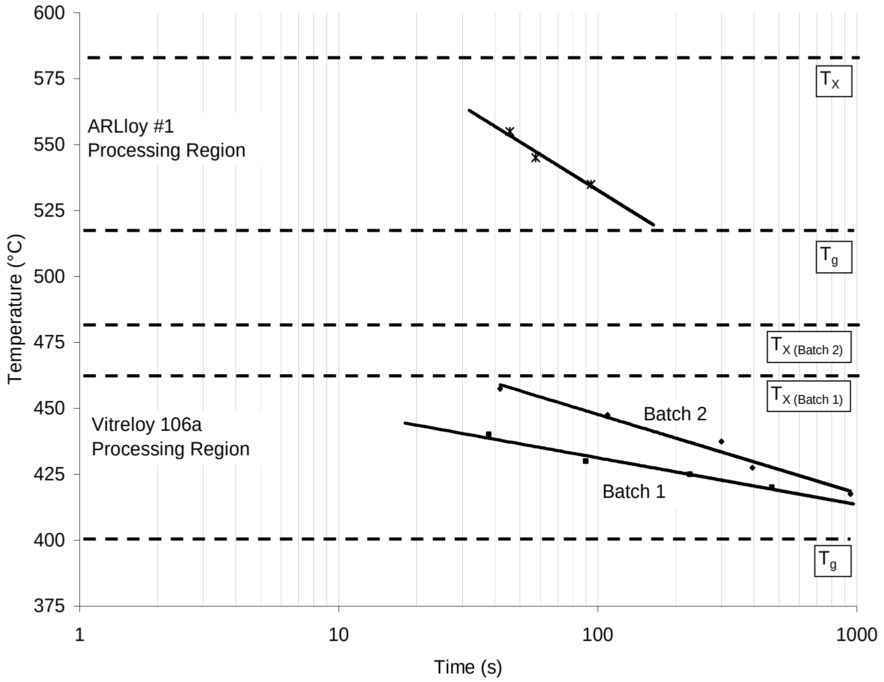

Figure 4.2 Schematic figure showing the time temperature transformation (TTT) boundary beyond which crystallization will occur. Boundaries were determined using a conservative estimate of a 40K/min heating rate.

4.1.2 Time-Temperature-Transformation Behavior

In the undercooled liquid region, the amorphous powder may partially or completely devitrify after a certain amount of time at temperatures at and above T_g, so it was necessary to obtain this time-temperature-tranformation (TTT) data for each alloy to determine how much time would be available to consolidate the powders. The TTT boundary was obtained by heating the powder sample to a temperature within the ΔT range (20K/min and 40K/min) and holding at that temperature and recording at which time the exothermic reaction begins (start of devitrification). These data points are plotted on a temperature vs. Log time plot to obtain the TTT boundaries (Figure 4.2).

Only the values obtained with the 40K/min heating rate were used as they tend to provide a more conservative estimate of the TTT boundary.

4.1.3 Thermomechanical Processing Conditions

As mentioned in the Materials and Methods chapter, much work and many iterations were put into the design and optimization of extrusion conditions and experiments. The most significant was the determination of the ΔT region and the TTT boundary to determine the particular time and temperature available for a particular alloy or composite. Tables 4.2 and 4.3 give the thermomechanical processing conditions used. The extrusions presented were all performed with the batch 2 (low oxygen) Vitreloy 106a. The summary and rationale for each set of experiments is presented here.

Table 4.2 Thermomechanical processing conditions for Vitreloy 106a (Batch 2) and composites.

Dissertation ID	Billet ID	Crystalline Content	Can Material	Can Dimensions	ECAE Route	Die Temperature (°C)	Extrusion Temperature (°C)	Punch Speed (mm/s)
Zr01	Ni026	60 vol% W[1]	Ni	19 mm x 19 mm x 89 mm	1A	410	400	0.508
Zr02	Ni022	60 vol% W[1]	Ni	19 mm x 19 mm x 89 mm	1A	430	420	0.508
Zr03	Ni010	60 vol% W[1]	Ni	19 mm x 19 mm x 89 mm	2B	410 / 420	400 / 410	0.508
Zr04	Ni012	50 vol% W[2]	Ni	19 mm x 19 mm x 89 mm	1A	420	410	0.508
Zr05	Ni013	60 vol% W[2]	Ni	19 mm x 19 mm x 89 mm	2C	410 / 420	400 / 410	0.508
Zr06	Ni020	70 vol% W[2]	Ni	19 mm x 19 mm x 89 mm	2B	410 / 420	400 / 410	0.508
Zr07	Ni 3	60 vol% W[2]	Ni	19 mm x 19 mm x 175 mm	1A	410	400	0.508
Zr08	Ni024	---	Ni	19 mm x 19 mm x 89 mm	1A	410	400	0.508
Zr09	Ni023	---	Ni	19 mm x 19 mm x 89 mm	1A	430	420	0.508
Zr10	Ni029	---	Ni	19 mm x 19 mm x 89 mm	2B	410 / 420	400 / 410	0.508
Zr11	Ni071	---	Ni	102 mm x 25 mm dia.	1A	420	410	0.127
Zr12	Ni074	60 vol% W[3]	Ni	102 mm x 25 mm dia.	1A	420	410	0.127
Zr13	VitCuNi 3	60 vol% Cu	Ni	102 mm x 25 mm dia.	1A	420	415	0.127
Zr14	VitCuNi 3	60 vol% Ni	Ni	102 mm x 25 mm dia.	1A	420	415	0.127

[1] ARL supplied W Powder
[2] ARL supplied Ni-coated W Powder
[3] Alldyne W Powder

Zr01-Zr03 were the first attempts to make composites with the Batch 2 Vitreloy powders (Table 4.2). Previous experience with the Batch 1 powder and monolithic amorphous alloy consolidation had narrowed the temperature range to between 400°C-430°C without major devitrification with a punch speed of 0.508 mm/s. Zr04-Zr07 were attempts to vary both the volume fraction of crystalline phase (50%-70%) and to see the effect of multiple extrusions. Also, the Ni-coated W powder was used in these cases to circumvent bonding problems associated with the initial bare powder. The concept of multiple extrusions was added due to the additional time provided by the Batch 2 powders as compared to the Batch 1 at a particular extrusion temperature. Zr07 was a long billet used to obtain compression and tensile samples. Zr08-Zr10 were the first attempts at consolidating monolithic Batch 2 Vitreloy powders without any crystalline phase. Extrusion temperatures varied from 400°C-420°C, a multipass extrusion was used (Zr10 – route 2B). Significant focus will be given to samples Zr11-Zr14 which incorporated new clean, unagglomerated W powder (Alldyne) as well as Cu and Ni crystalline powders and optimized conditions as determined from the previous extrusions. The four extrusions were performed in round cross-section tooling and at a slower punch speed (0.127 mm/s).

The ARLloy #1 experimentation was not as extensive as that done with the Vitreloy 106a (Table 4.3). This is partly the case because of the much shorter times available for extrusions and the higher processing temperatures. All the ARLloy#1 and composite extrusions were done in round cross-section tooling. Hf01-Hf02 were the first attempts at consolidation and were fast extrusions (1.27 mm/s). These were done to determine the effects of using Cu or Ni cans. For Hf03-Hf05, the tooling temperatures were modified to allow for slower extrusions. Hf06 was the first attempt at producing a composite with the Alldyne W powder. Using the knowledge gained from these few experiments, Hf07-Hf10 were done and were extensively characterized.

Table 4.3 Thermomechanical processing conditions for ARLloy #1 and composites.

Dissertation ID	Billet ID	Crystalline Content	Can Material	Can Dimensions	ECAE Route	Die Temperature (°C)	Extrusion Temperature (°C)	Punch Speed (mm/s)
Hf01	NiCan	---	Ni	102 mm x 25 mm dia.	1A	520	510	1.27
Hf02	CuCan	---	Cu	102 mm x 25 mm dia.	1A	530	510	1.27
Hf03	Ni3	---	Ni	102 mm x 25 mm dia.	1A	510	500	0.635
Hf04	CuMnl	---	Monel + Cu	102 mm x 25 mm dia.	1A	535	520	0.635
Hf05	Ni5 (075)	---	Ni	102 mm x 25 mm dia.	1A	515	510	0.635
Hf06 (stuck!)	Ni8 (078)	60 vol% W[1]	Ni	102 mm x 25 mm dia.	1A	475	415	unknown
Hf07	Ni6 (076)	---	Ni	102 mm x 25 mm dia.	1A	530	510	0.635
Hf08	Ni7 (077)	60 vol% W[1]	Ni	102 mm x 25 mm dia.	1A	530	510	0.635
Hf09	HfCuNi4	60 vol% Cu	Ni	102 mm x 25 mm dia.	1A	530	522	0.635
Hf10	HfCuNi4	60 vol% Ni	Ni	102 mm x 25 mm dia.	1A	530	522	0.635

[1] Alldyne W powder

4.1.4 Thermal Tracking of the Extrusion Process

As previously mentioned, thermocouples were placed at the top and bottom of each billet and in selected areas of the tooling to monitor the temperature during extrusion. A method was developed to use this capability to thermally track the temperature of the billet along with the tooling during extrusions. An example of how this was done is shown in plots of the tool and billet temperatures during the extrusion process for samples Cu058 and Zr09(Ni023) in Figure 4.3. Cu058 is a Cu billet containing Vitreloy 106a Batch 1 (high oxygen) powder extruded by route 1A at 6mm/s in a 420°C tool.

From the plot for Zr09(Ni023), it is apparent that the billet top and bottom are within about 5°C during extrusion. The punch speed for Cu058 is 12 times faster than that for Zr09(Ni023). This causes a much larger rise in temperature (see both billet bottom temperatures in Figure 4.3) during extrusion for Cu058 (~25°C), even though the can material has a lower flow stress.

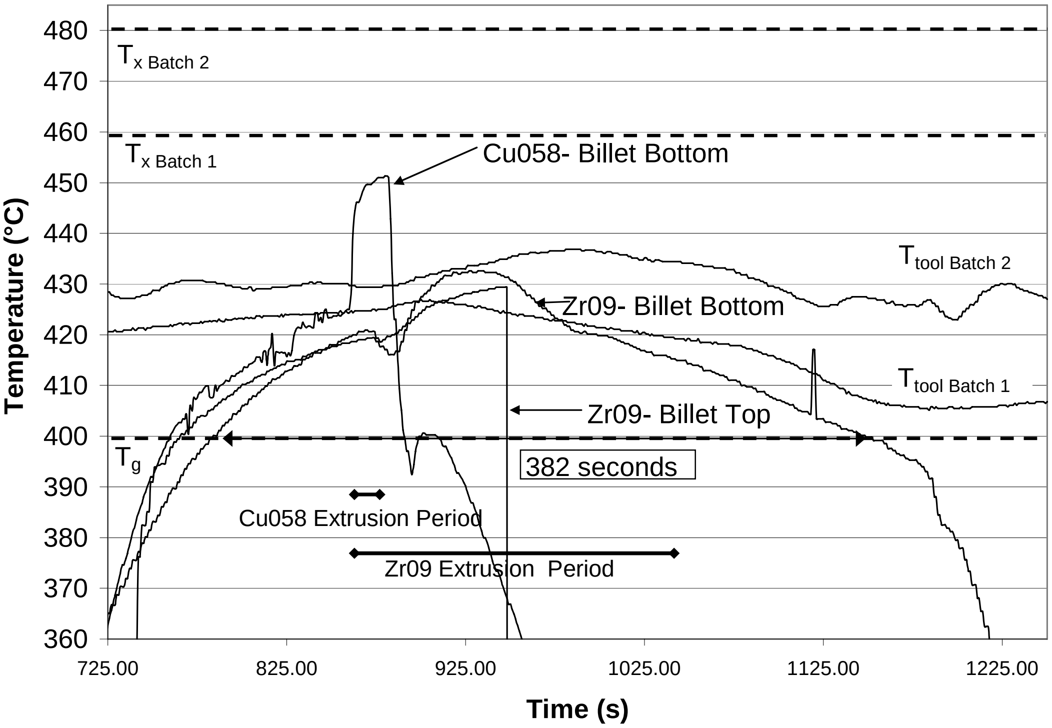

Figure 4.3 Temperature versus time for billets Cu058 and Zr09 showing the sample time above T_g and the adiabatic rise in temperature due to the material passing through the shear zone. Both billets were extruded with the die at 430°C and with a punch speed of 6 mm/s and 0.5 mm/s for Cu058 and Zr09, respectively. Note that the horizontal axis is only a time scale and not an indicator of the amount of time into the processing.

The times at and above T_g, from the plot of temperature versus time during extrusion, are used to construct thermal histories of the extrusions that can be overlaid on the TTT diagram as shown in Figure 4.4. The plotted results indicate that processing of these billets was done without crossing the TTT boundary. Notice that billet Cu058 came very close to the boundary due to the sharp temperature rise associated with the heat of deformation. Since the thermocouples in billet Zr10(Ni029) did not survive the second extrusion, the hypothetical dashed line on Figure 4.4, for this route 2B extrusion, is constructed assuming that the billet experienced the same time at temperature as the first extrusion pass. Therefore, the total time at temperature for the two extrusion case is nearly double the time measured for one extrusion pass.

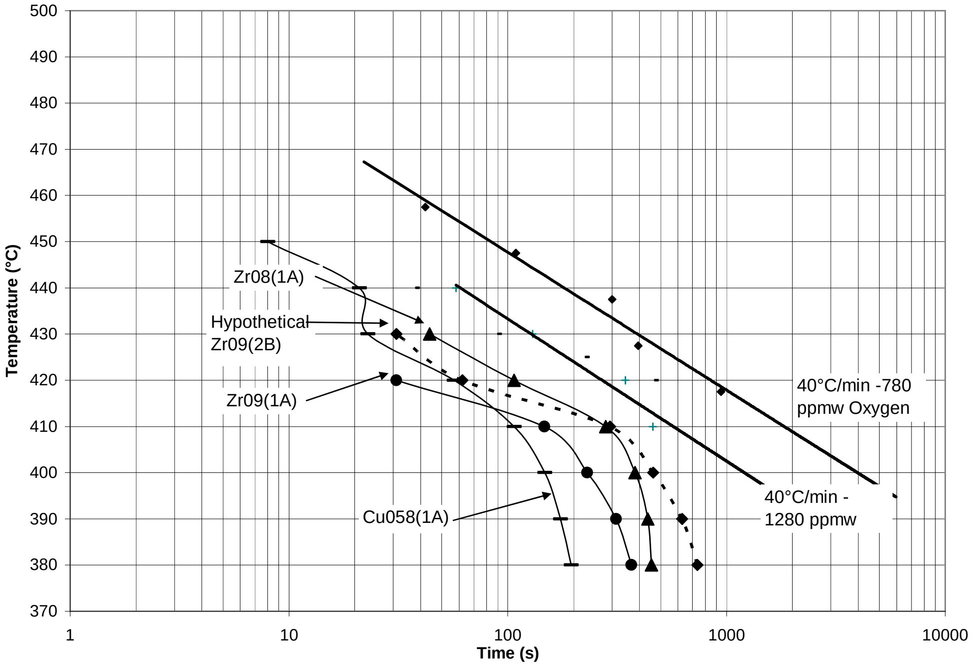

Figure 4.4 Time-temperature transformation showing the crystallization boundary for Batches 1 and 2 powders, and the thermal histories of some of the ECAE extruded billets. The dashed line shows the predicted behavior for the route 2B pass of billet Zr10.

4.2 **Effects of Processing Variables on Consolidate Properties**

4.2.1 Results for Billets Zr01 – Zr03

Figures 4.5 to 4.7 show the microstructures for billets Zr01 to Zr03. In all cases it can be observed that there is little bonding occurring between the Vitreloy 106a matrix and the W particles. Even after two extrusions, there are voids and significant W particle pull-out from the amorphous matrix. Recall that the W powder used for this these extrusions was uncoated W supplied by the Army Research Laboratory. Close examination of the surface of these W particles shows that there is a layer of scale, possible an oxide coating (Figure 4.8). This scale is clearly detrimental to adequate bonding, and therefore the use of this W powder was discontinued for further extrusions.

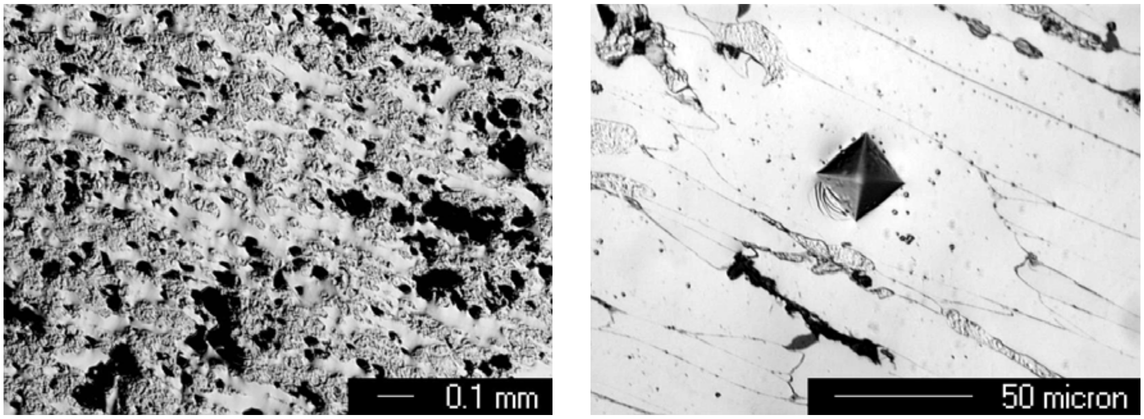

(a) (b)

Figure 4.5 Light micrographs of ECAE consolidated composite material from billet Zr01 containing Vitreloy 106a and 60 vol% W. Consolidated at 410°C, by route 1A with a punch speed of 0.508 mm/s in a Ni can. (a) W particle pullouts that occurred during mechanical polishing. (b) Microhardness indentation (500g, 15 s) showing shear band generation from the edge of the indent.

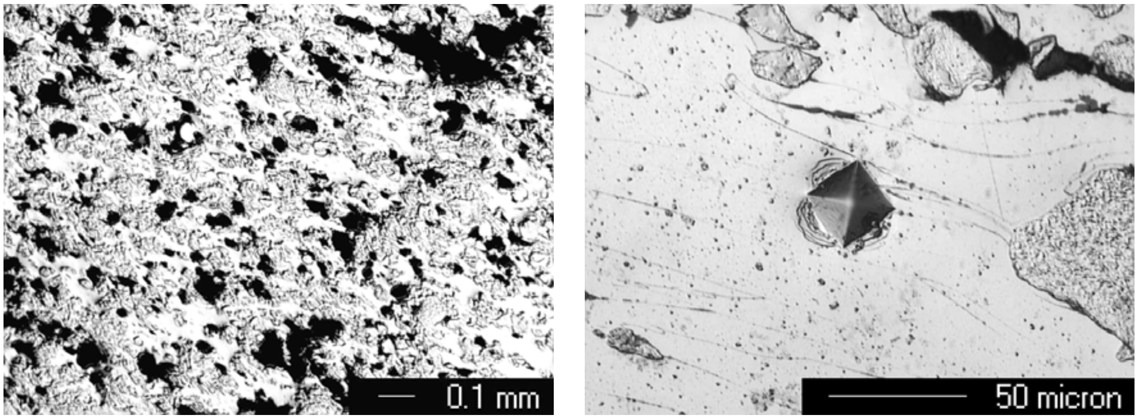

(a) (b)

Figure 4.6 Light micrographs of ECAE consolidated composite material from billet Zr02 containing Vitreloy 106a and 60 vol% W. Consolidated at 430°C, by route 1A with a punch speed of 0.508 mm/s in a Ni can. (a) W particle pullouts that occurred during mechanical polishing. (b) Microhardness indentation (500g, 15 s) showing shear band generation from the edge of the indent.

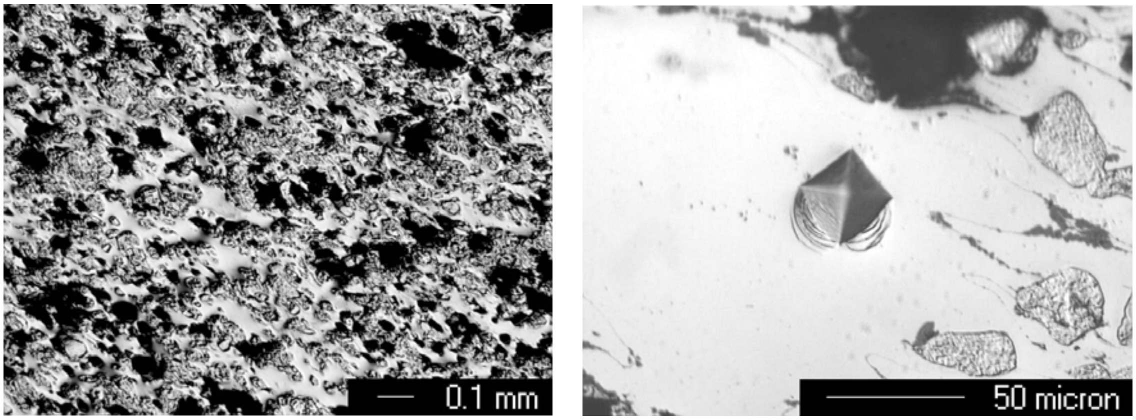

(a) (b)

Figure 4.7 Light micrographs of ECAE consolidated composite material from billet Zr03 containing Vitreloy 106a and 60 vol% W. Consolidated at 410°C for the first pass, and 420°C for the second pass by route 2B with a punch speed of 0.508 mm/s in a Ni can. (a) W particle pullouts that occurred during mechanical polishing. (b) Microhardness indentation (500g, 15 s) showing shear band generation from the edge of the indent.

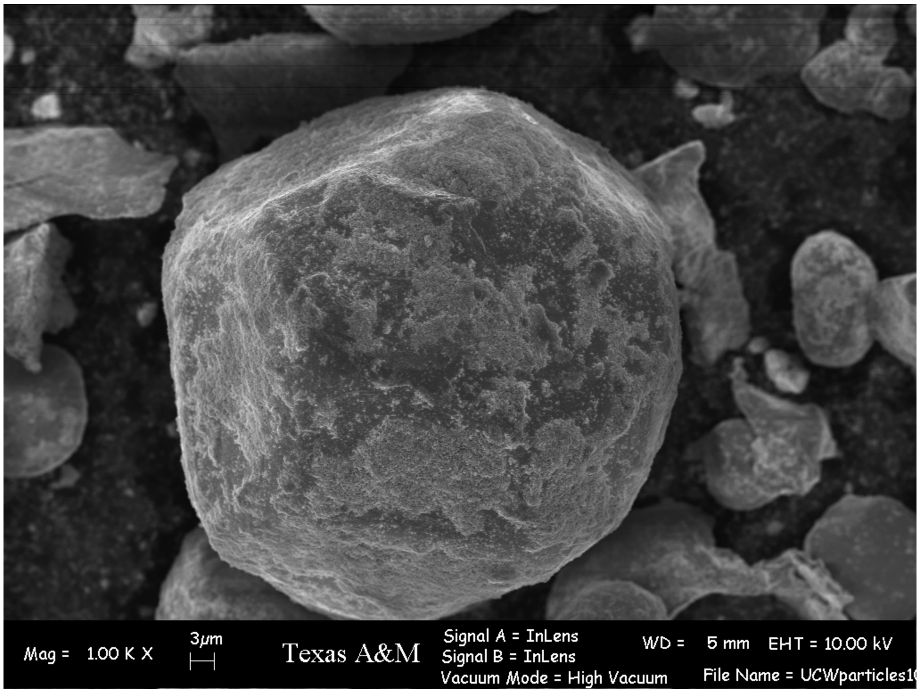

Figure 4.8 SEM image showing the scale/impurity coating visible on the outside surfaces of the ARL supplied W powder.

Examination of the thermal traces for Zr01 and Zr03 in Figure 4.9 show that the TTT boundary was not crossed. This is a good indicator that large scale devitrification should not have occured during the extrusions. This premise is verified by the shear bands apparent around the microhardness indentations seen in Figures 4.5.b – 4.7.b. Crystallinity and devitrification in amorphous alloy are generally accompanied by brittle behavior, which results in no shear bands (i.e. deformation by dislocation generation), but rather cracking from the corners of the indentation [ref]. Even further evidence of no crystallinity is seen in the DSC traces of the consolidated powders (Figure 4.10). Partial devitrification tends to shift the glass transition temperature to a lower value, and full devitrification is accompanied by a complete disappearance of the exothermic peak. Figure 4.10 shows that T_g has not shifted, and the smaller exothermic peaks are not a result of devitrification, but of the large volume of W powder present in the consolidate.

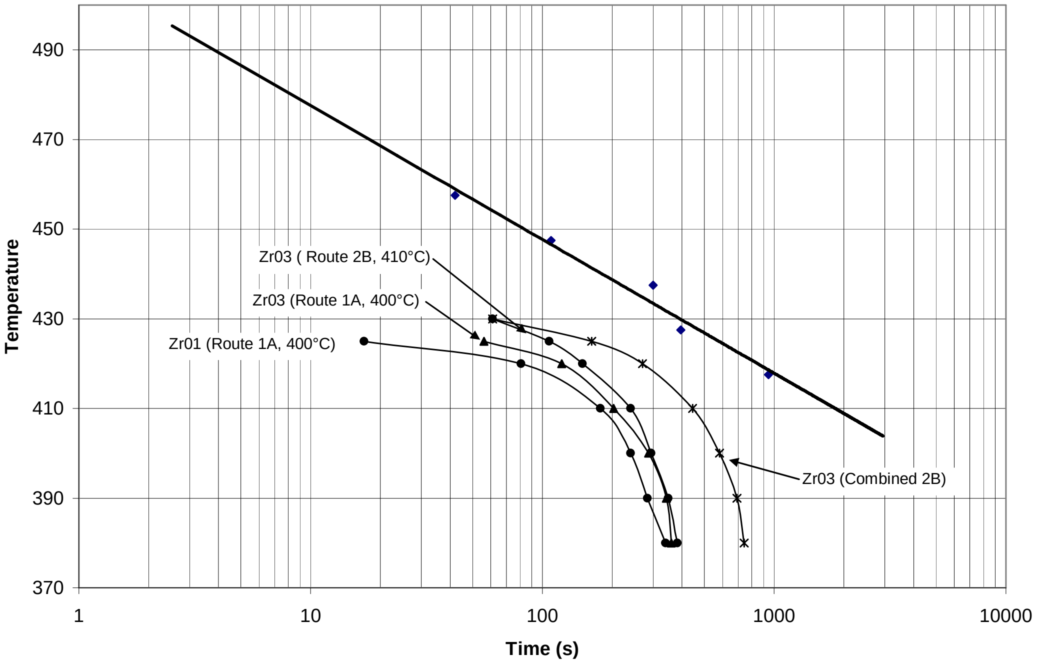

Figure 4.9 Thermal histories of billets Zr01 – Zr03. Note that even after two extrusion that the billets have not been exposed to temperatures for times that would cause significant crystallization.

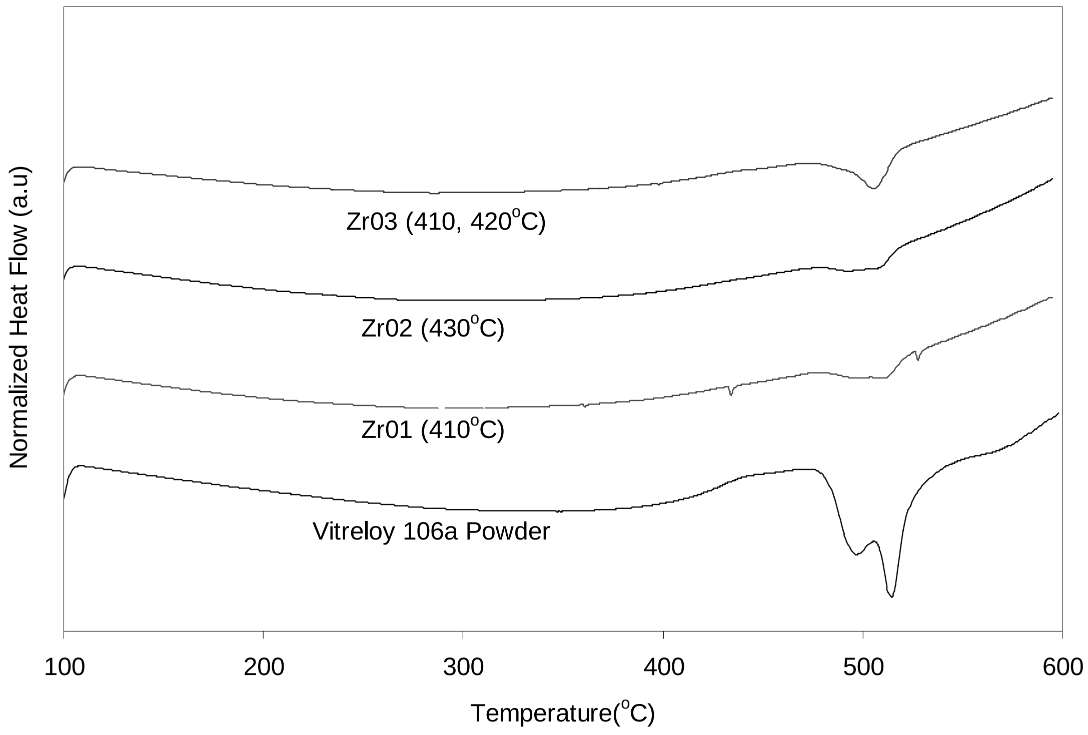

Figure 4.10 DSC traces performed at 40K/min on the starting batch 2 Vitreloy 106a powder and consolidated composite material from billets Zr01-Zr03. The show little, if any shift in the T_g and T_x of the consolidates as compared to the starting powder.

4.2.2 Results for Billets Zr04 – Zr07

The next set of experiments involved the use of Ni-coated W powder for better bonding and consolidation in the extrudates. These experiments used Ni-coated W powders instead of the scale coated powder previously used. Figure 4.11 shows the starting blended powder used for these extrusions. Figures 4.12 to 4.14 show the optical micrographs of the consolidated microstructures for billets Zr04 to Zr06. Post consolidation, there appears to be much better infiltration of the crystalline W phase into the Vitreloy 106a amorphous metal matrix. The dark spots seen in the micrographs are not residual porosity, but rather are believed to be voids left by W agglomerates that were pulled out during mechanical polishing of the microscopy samples. Even with this being the case, the flow plane microstructures appear far better than those obtained from the uncoated W particles.

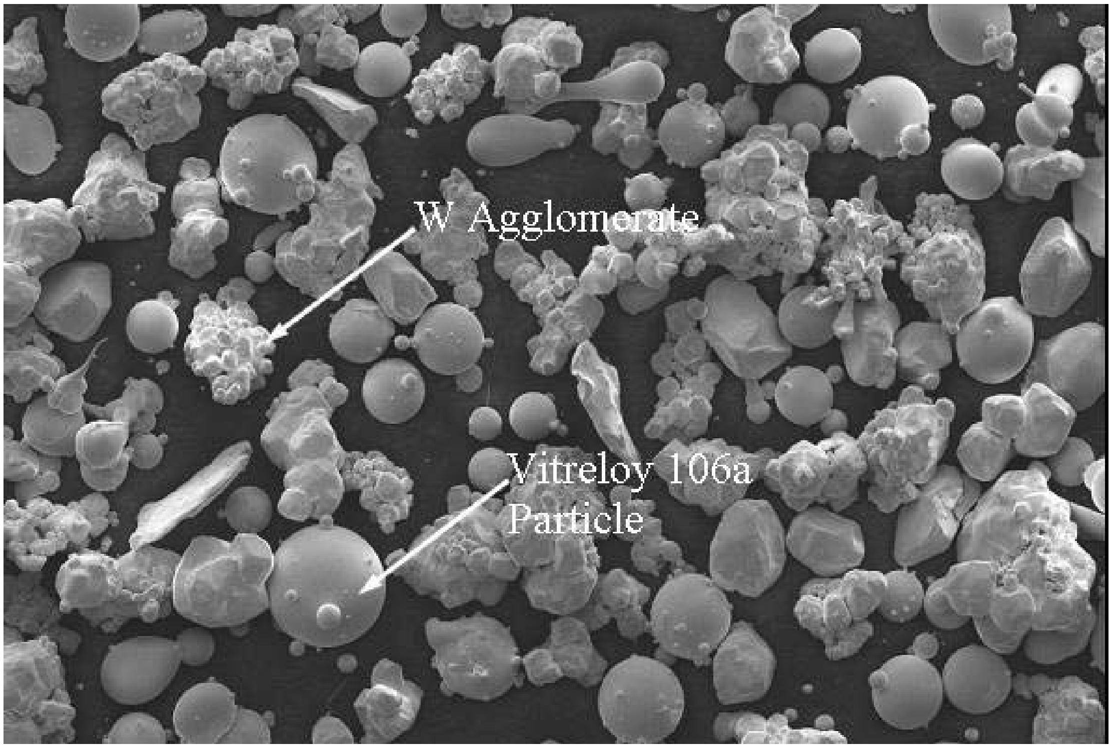

Figure 4.11 SEM image of blended Vitreloy 106a and Ni-coated W powders. The spherical Vitreloy 106a powder ranges between 38μm - 150μm in diameter. The W agglomerates have a size range of 38μm - 53μm.

The microhardness indentations were examined with optical microscopy for shear banding and particle-to-particle bond strength (Figures 4.12.b to 4.14.b). In all three cases, shear bands are seen in the Vitreloy 106a matrix giving evidence of retention of ductility and amorphous character in the amorphous metal phase. Indentations were made along Vitreloy 106a / W boundaries, but no interfacial cracking is seen, indicating significant bonding has occurred between the amorphous metal matrix and crystalline powder phase.

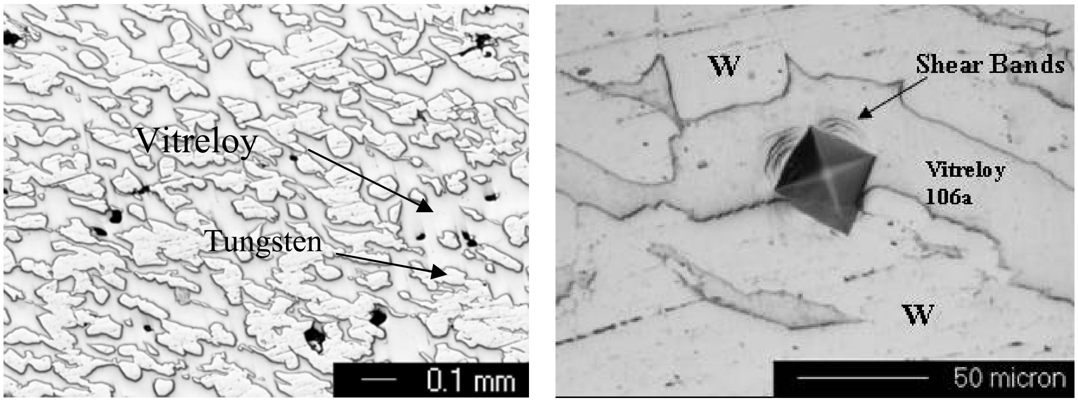

(a) (b)

Figure 4.12 Light micrographs of ECAE consolidated composite material from billet Zr04 containing Vitreloy 106a and 50 vol% Ni-coated W. Consolidated at 420°C, by route 1A with a punch speed of 0.508 mm/s in a Ni can. (a) The Vitreloy appears to have infiltrated the W fairly well and there are few W particle pull-outs (b) Microhardness indentation (500g, 15 s) showing shear band generation from the edge of the indent.

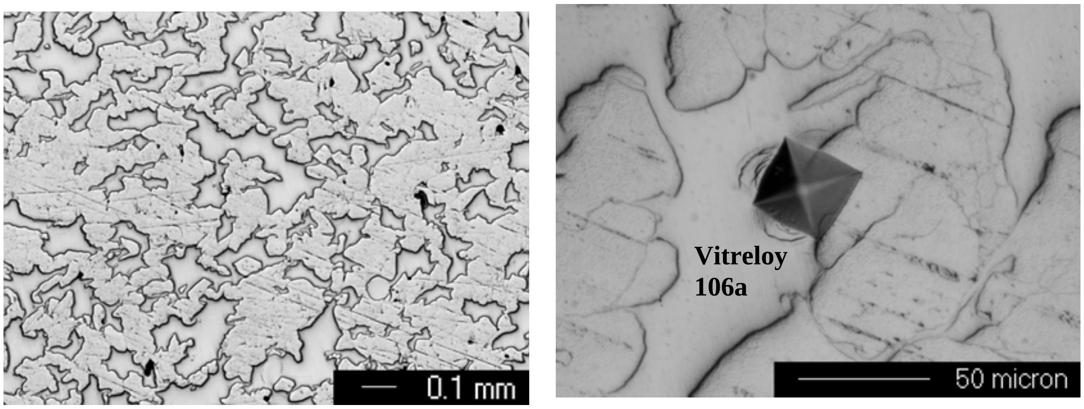

(a) (b)

Figure 4.13 Light micrographs of ECAE consolidated composite material from billet Zr05 containing Vitreloy 106a and 60 vol% Ni-coated W. Consolidated at 410°C during the first by and 420°C during the second pass by route 2C with a punch speed of 0.508 mm/s in a Ni can. (a) The Vitreloy appears to have infiltrated the W fairly well and no W particle pull-outs (b) Microhardness indentation (500g, 15 s) showing shear band generation from the edge of the indent.

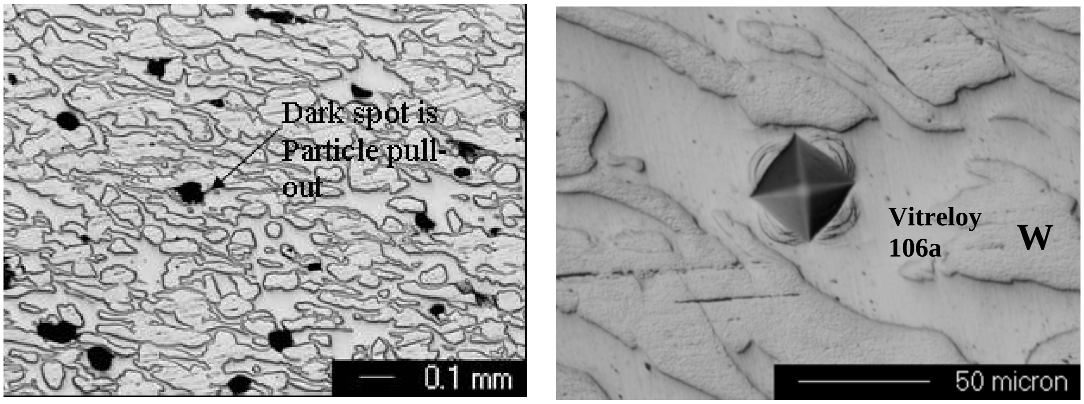

(a) (b)

Figure 4.14 Light micrographs of ECAE consolidated composite material from billet Zr06 containing Vitreloy 106a and 70 vol% Ni-coated W. Consolidated at 410°C during the first by and 420°C during the second pass by route 2C with a punch speed of 0.508 mm/s in a Ni can. (a) The Vitreloy appears to have infiltrated the W fairly well and some W particle pull-out is present (b) Microhardness indentation (500g, 15 s) showing shear band generation from the edge of the indent.

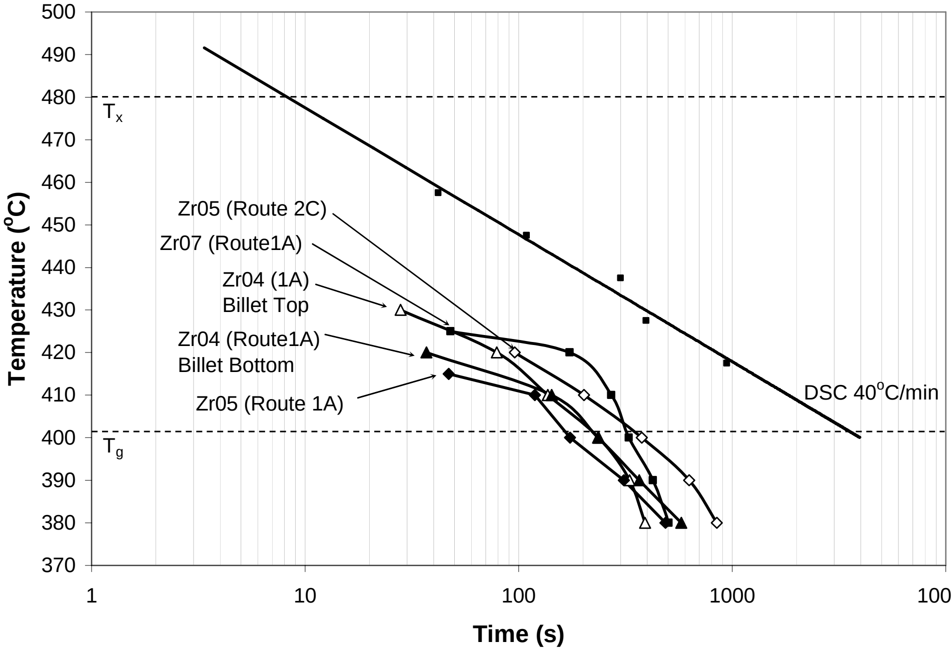

Figure 4.15 Thermal histories of billets Zr04, Zr05 and Zr07. Note that even after two extrusion that the billets have not been exposed to temperatures for times that would cause significant crystallization.

Thermal tracking of billets Zr04, Zr05 and Zr07 (to billet will be addressed shortly) show similar behavior to that seen in Figure 4.9. The extrusions are performed at the same punch speed (0.508 mm/s) so this is not unexpected. In the case of billet Zr04, the thermocouples on the bottom and top of the billet survived the extrusion. Observe that the top of the billet is exposed to higher temperatures for longer times, due to adiabatic heat generated by the billet during extrusion and the longer time in the die (i.e. the bottom is exposed to circulating air at the exit of the tool channel while the top is still extruding). Billet Zr05 shows exposure to higher temperatures during the second extrusion, which was likely caused by the greater heat generation of the fully dense material passing through the shear zone. During the first extrusion, the powder was consolidated at the shear zone which liberated less heat of deformation. Unsurprisingly, billet Zr07 is exposed to temperatures above T_g for a longer time than the other billets because of the additional billet length. It is likely that little, in any devitrification has occurred as the thermal traces are far from the TTT boundary.

Property measurements were made on samples Zr04-Zr07 included both Vickers microhardness and mechanical testing. Vickers microhardness testing was done on the amorphous Vitreloy 106a phase of the consolidate to determine if hardening occurs during extrusion. The microhardness values obtained, along with monolithic consolidated V106a (Cu058) are given in Table 4.4. Mechanical testing in both tension and compression was performed on some of the composite consolidates for comparison with monolithic amorphous alloy (Figure 4.16). These are also compared with billet Cu058. The samples tested in tension failed within the linear elastic region at low loads and after very little deformation. The samples tested in compression showed much higher stresses at failure. Comparison of the amorphous composite with the monolithic amorphous alloy shows similar compressive strengths (1540 MPa and 1640 MPa, respectively) and percent elongations (1.9% and 2.3%, respectively), but there is a difference in the Young's modulus (206 GPa and 80 GPa, respectively).

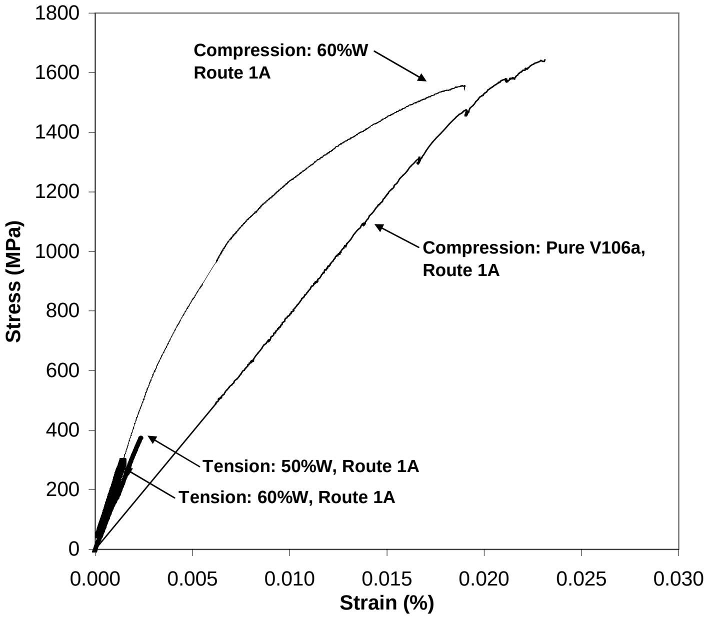

Figure 4.16 Stress-strain curves in compression and tension for Vitreloy 106a + W particulate composites.

Table 4.4 Summary of mechanical properties and microhardness for pure Vitreloy 106a and ECAE consolidated Vitreloy 106a + particulate W composites.

Billet ID	Vol.% W	ECAE Route	Loading	E (GPa)	UTS (MPa)	%EL (%)	HV_{500}	HV (GPa)
058 (V106a)	0	1A	Comp.	80	1640	2.3	469±17	4.60±0.17
Zr04	50	1A	Tension	159	---	---	489±20	4.80±0.20
Zr05	60	2C	---	---	---	---	492±25	4.83±0.25
Zr06	70	2B	---	---	---	---	513±36	5.03±0.35
Zr07	60	1A	Tension	205	---	--	---	---
Zr07	60	1A	Comp.	206	1540	1.9	---	---

4.2.3 Results for Billets Zr08 – Zr10

The purpose of this set of experiments was to examine and compare the level of consolidation, thermal stability, microhardness and processability for Vit106a with two different levels of oxygen contamination. The results of extrusions (Billets Cu052 and Cu058) from previous experiments which used the high oxygen powder are used for comparison. Figure 4.17 shows flow plane (workpiece side plane) optical micrographs of billets Cu058 and Zr09. Particles in each case are severely deformed and very little porosity is visible indicating substantial viscous flow during ECAE. A higher particle aspect ratio and sharper triple junctions for billet Zr09 point to a better consolidated powder point to a better consolidation environment for these cases. It is assumed that the larger flow stress of the Ni cans provided a higher hydrostatic pressure during consolidation. It is also clear from Figure 4.17 that uniform particle deformation occurs over large regions.

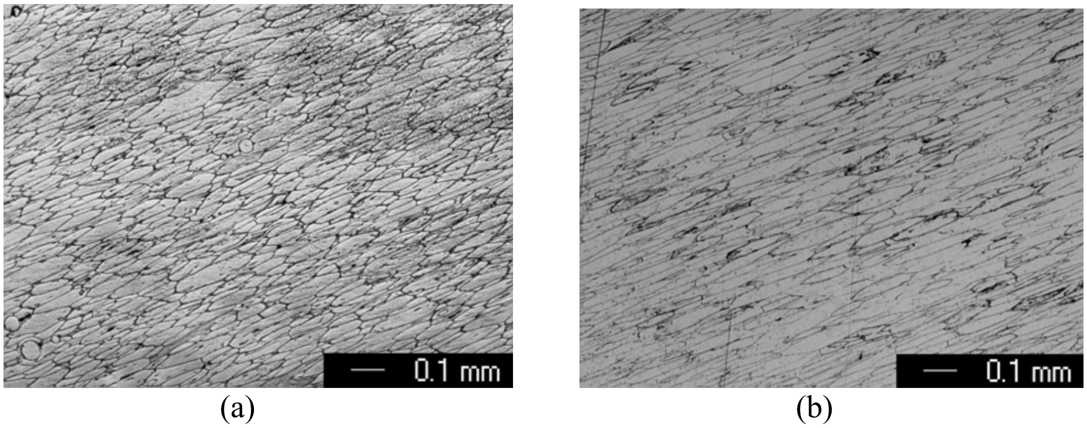

(a) (b)

Figure 4.17 Light micrographs of flow plane microstructures of (a) billet Cu058 and (b) billet Zr09 after one extrusion pass. The extrusion direction is left to right.

The absence of both large scale shear localization and non-uniform particle deformation give evidence that the ECAE process results in homogeneous deformation.

Representative microhardness indentations, shown in Figure 4.18 for billets Cu052 and Zr10 (route 2B), demonstrate the retention of amorphous character by the presence of shear banding around the indentations. As previously mentioned, significant devitrification would have resulted in a more pronounced brittle behavior and cracks propagating from the diamond indentation corners. Further verification of good particle bonding can be seen on the samples by observing that the prior particle boundaries do not separate in the vicinity of the indent.

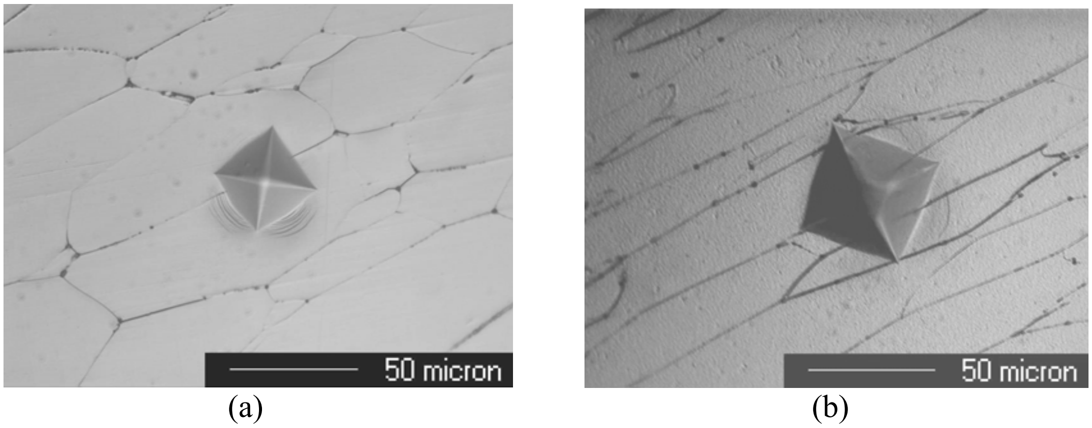

(a) (b)

Figure 4.18 Light micrographs of Vickers microhardness indentations on (a) Cu052 and (b) Zr10-Route 2B showing shear bands indicative of amorphous character. Sample Zr10 verifies the predominant amorphous nature after two extrusions. Both samples show that the particles do not debond as a result of stresses caused by the hardness indentations.

Figure 4.19 shows the DSC analyses of the initial powder and the post-extruded Ni-can billets. It is clear that there is little difference in the T_g and the T_x of the powder and the consolidated Batch 2 material. The DSC analyses of the 1280 ppmw O_2 Batch 1 consolidates (Figure 4.19.b), on the other hand, show that the material experiences a decrease in T_x and enthalpy of crystallization when compared to the initial powder indicating that some divitrification probably occurred during processing. The thermal stability of the Batch 2 Vitreloy 106a powder is evidenced by the fact that the DSC traces are the same, regardless of the extrusion processing temperature.

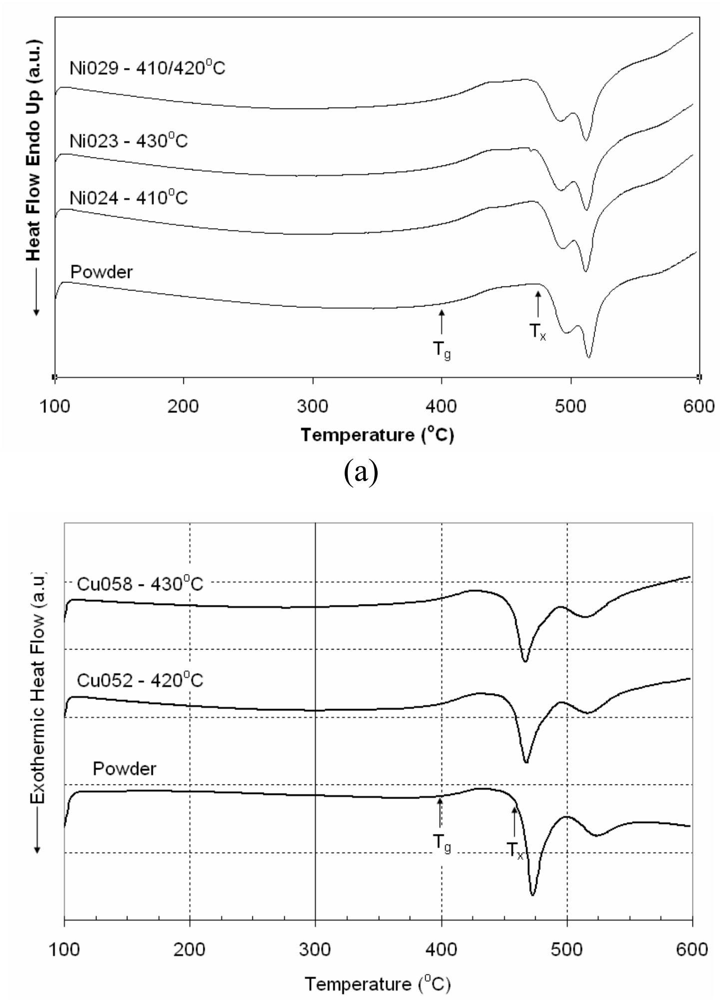

(a)

(b)

Figure 4.19 DSC scans of (a) Batch 2 consolidates and (b) Batch 1 consolidates. Batch 1 consolidates show a modest decrease in both T_x and enthalpy of crystallization as compared to the initial powder. Batch 2 shows similar curves regardless of processing temperature indicating that the lower oxygen content increases thermal stability.

While good particle bonding, retention of amorphous character and full density are demonstrated by the Batch 2 consolidate, inter-particle cracks are sometimes observed along the particle flow direction (Figure 4.20). It was suspected that these cracks arise after the material passes through the shear zone and are caused by one or both of the following issues. Notice that in Figure 4.20.a that the cracks seem to propagate from the corners at the ends of the samples. It is possible that these sharp corners serve as stress concentrations and that the cracks initiate and propagate from those regions. Another possible reason of the cracking could by from nonuniform stresses in the consolidated material and the can which arise during billet cooling. The next set of extrusions attempted to deal with these issues, and prevent the cracking from occurring.

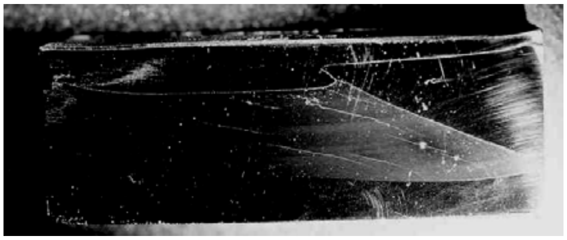

(a)

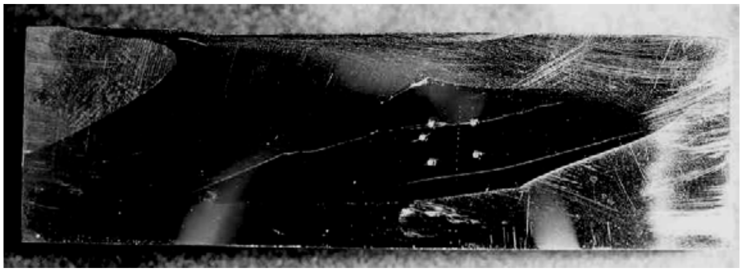

(b)

Figure 4.20 Photographs of ECAE extruded Vitreloy 106a show large scale cracks in (a) billet Zr09 and (b) billet Zr10. These cracks are probably the result of residual stresses that develop in the can material during cooling, which cause stress concentrations in the consolidated material.

4.2.4 Results for Billets Zr11 – Zr14

To alleviate the possibility of cracking due to stress concentrations from either stress concentrations in the can material during cooling or billet geometry, a new tool was designed which used round cross-section billets rather than square billets. In addition, this tooling incorporated much better thermal control than the previous square cross-section tooling. The extrusion produced by this method showed no cracking.

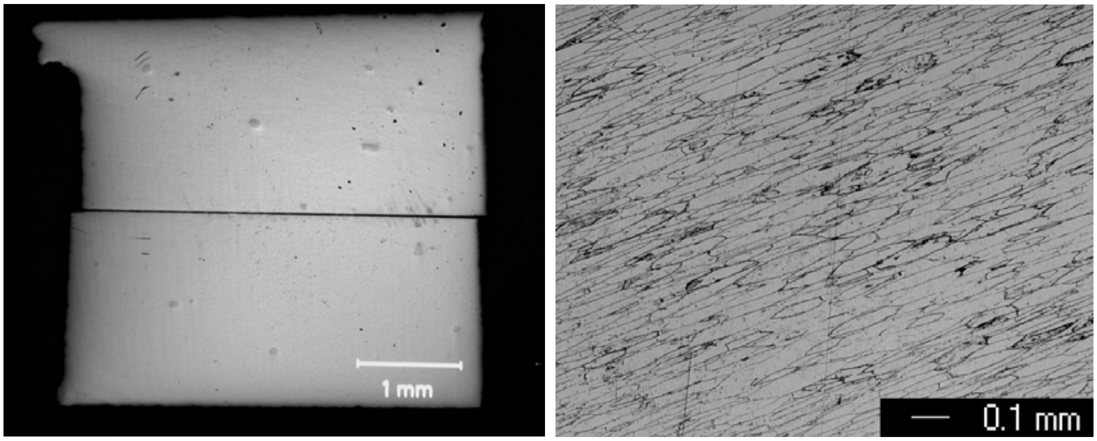

(a) (b)

Figure 4.21 Light micrographs of ECAE consolidated Vitreloy 106a from billet Zr11. Consolidated at 420°C with a punch speed of 0.127 mm/s in a Ni can. (a) The Vitreloy 106a appears to be consolidated uniformly with little porosity (b) An etched region of the billet flow plane shows good particle elongation and no voids.

Figures 4.21.a to 4.24.a show the polished surfaces of 2 mm x 2mm x 4mm samples EDM cut from the consolidated region of billets Zr11-Zr14. Figure 4.21.b to 4.24.b shows close-up regions of samples Zr11 to Zr14. Figure 4.21.a shows the consolidated material from billet Zr11. The sample surface is smooth and has only a few pores from particle pull-out. Billet Zr12 contains 60 vol% agglomerate free, clean W powder, supplied by Alldyne. It appears as if the Vitreloy has infiltrated the W fairly well with little visible porosity or particle pull-outs (Figure 4.22.b). In one region, there is a large region of consolidated Vitreloy 106a that would make the consolidation appear to be nonuniform. It is suspected that since this "band" is along the shear angle that results from a single ECAE extrusion that this region is a result of improper mixing (i.e. a layer of amorphous powder in the can that was not mixed with W) rather than an area that segregated due to nonuniform consolidation conditions.

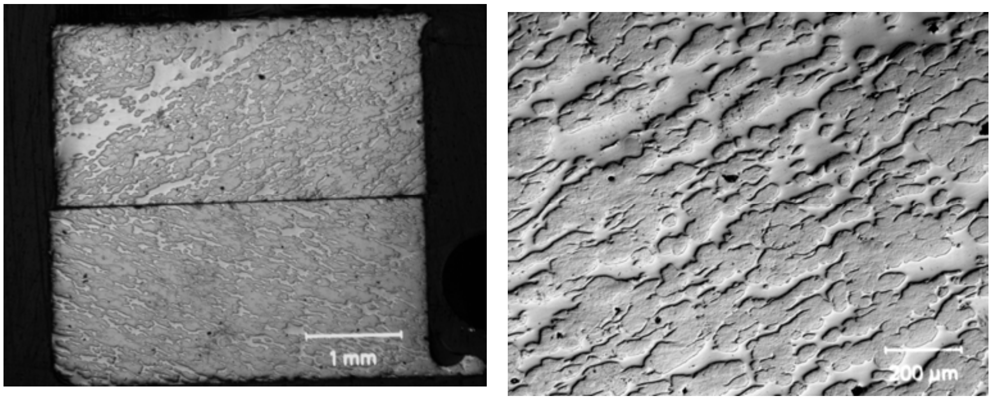

(a) (b)

Figure 4.22 Light micrographs of ECAE consolidated Vitreloy 106a + 60vol% W from billet Zr12. (a) The Vitreloy 106a appears to be have infiltrated the W well (b) A closer view of the flow plane shows no particle pullouts as was the case with the previous W composites that were consolidated.

Figs 4.23.a and 4.24.a show the consolidated composites for Vitreloy 106a and either Cu or Ni. In these cases, the high volume and low flow strength of Ni and Cu as compared to the Vitreloy 106a at the processing temperatures (410°C-430°C) cause the crystalline phase to become the matrix phase of the composite. Essentially, the crystalline phase was so ductile that it flowed around the amorphous phase during the consolidation event. In fact, there is little deformation/elongation of the amorphous metal particles in both of these cases. This is contrast to the W-composite case where the W particles did not deform and the Vitreloy became the matrix phase.

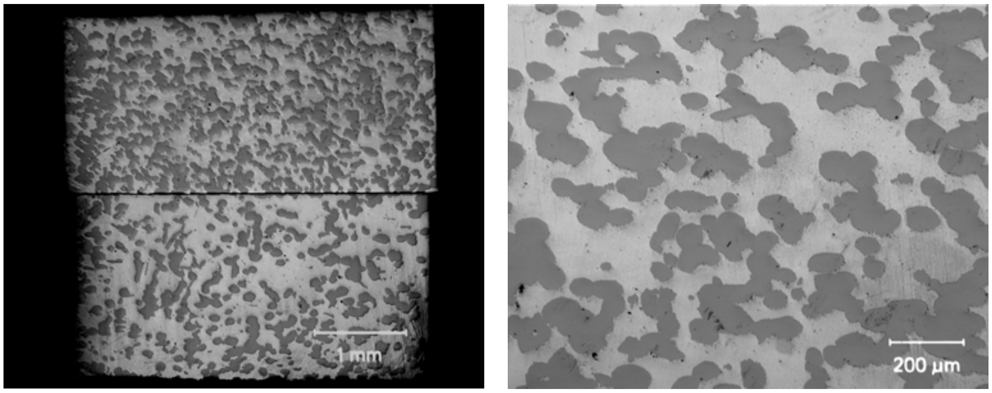

(a) (b)

Figure 4.23 Light micrographs of ECAE consolidated Vitreloy 106a + 60vol% Cu from billet Zr13. (a) Longitudinal plane showing that the Cu (the lighter color phase) comprise the matrix. (b) A closer view of the longitudinal plane good consolidation of the blended amorphous crystalline powders.

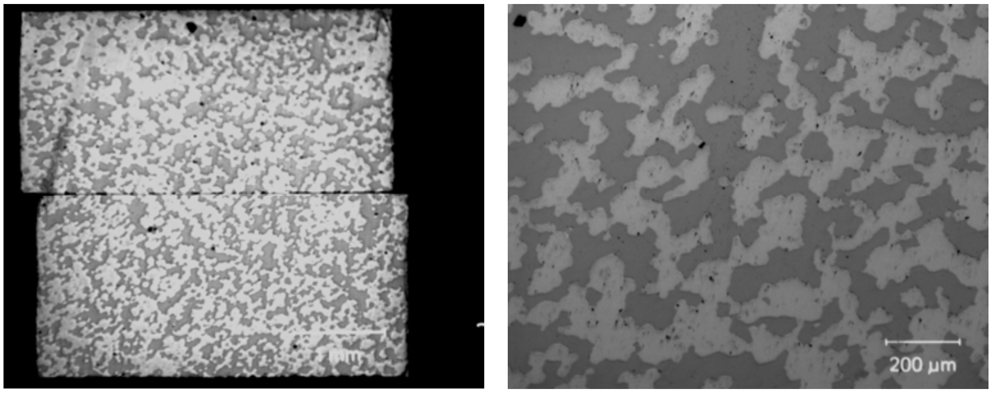

(a) (b)

Figure 4.24 Light micrographs of ECAE consolidated Vitreloy 106a + 60vol% Ni from billet Zr14. (a) Longitudinal plane showing that the Ni (the lighter color phase) comprise the matrix. (b) A closer view of the flow plane good consolidation of the blended amorphous crystalline powders, but little amorphous particle deformation from the consolidation.

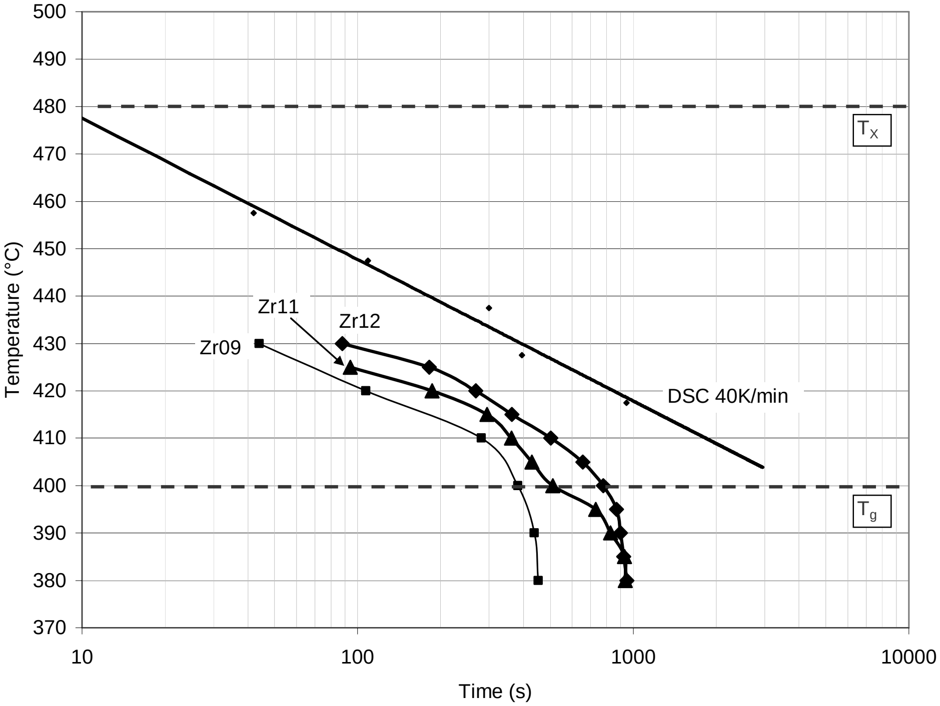

Figure 4.25 Thermal histories of billets Zr09, Zr11 and Zr12. The punch speed used for billets Zr11 (Vitreloy 106a) and Zr12 (Vitreloy 106a + 60%W) is one-fourth that used for Zr09 (Vitreloy 106a) (0.127 mm/s vs. 0.508 mm/s), yet the thermal histories remain away from the TTT boundary.

The thermal traces for billets Zr09, Zr11 and Zr12 are given in Figure 4.25. Notice that in the cases of billets Zr011 and Zr012, the lines are closer to the TTT boundary than in the previous extrusions. This is because the extrusion speed was four times slower than in the previous cases (0.127 mm/s vs. 0.508 mm/s). Even with this being the case, the traces do not cross the boundary, and therefore, the consolidates are likely still predominantly crystalline in nature.

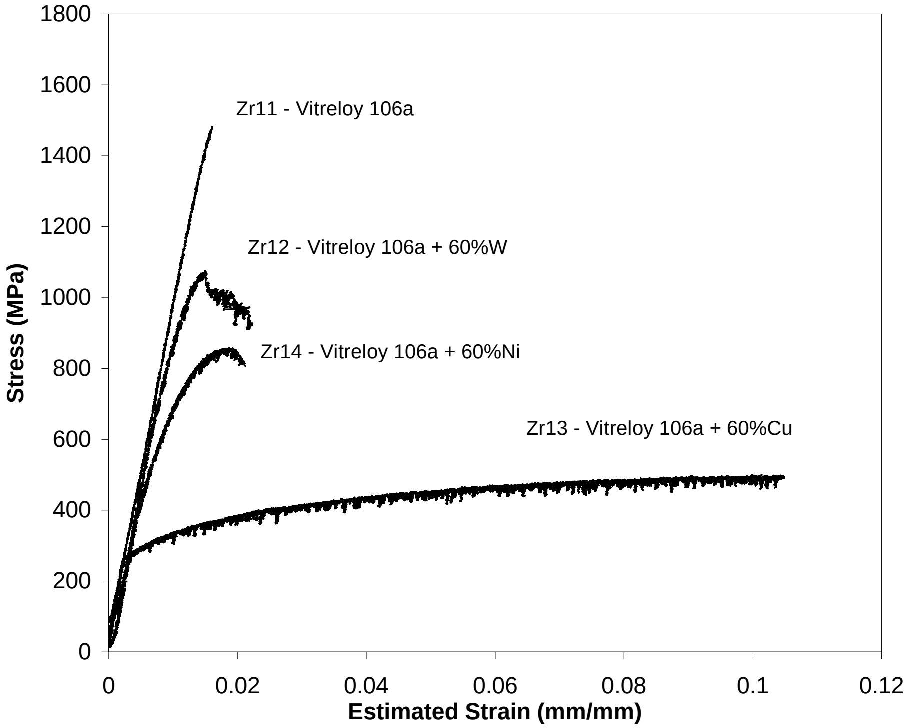

Figure 4.26 Compression stress-strain curves for ECAE consolidated Vitreloy 106a and composites containing 60 vol% W, Ni or Cu crystalline phase. The strain shown is estimated by scaling the measured results and multiplying by a factor determine from accurate measurement of the amorphous metal modulus.

Figure 4.26 shows representative stress-strain curves obtained by uniaxially compressing 2 mm x 2 mm x 4 mm samples of consolidated material from billets Zr11 to Zr14 at a rate of 10^{-4}/s. Because of the small sample size, a extensometer could not be used to measure the strain, and therefore the strain measured was higher than the actual value because of deformation in the grips during testing. But by observing that the modulus is similar for all four cases, and knowing the actual modulus of elasticity for Vitreloy 106a (from Figure 4.16: ~96 GPa), the strain values can be scaled to more accurately represent the bulk material behavior. With this correction in place the strain at failure for sample Zr11 is ~1.7%, at 1.5 MPa. The Vitreloy 106a + 60 vol% W sample does appear to have some plasticity (%EL = 2.2%), and because W is very brittle at room temperature, and the modulus is closer to that of the Vitreloy 106a matrix (~96 GPa for V106a vs. 400 GPa for W), it is likely that the deformation is taking place in the amorphous phase. Also, the strength in this composite is still fairly high (~1100 MPa), but not as high as the values obtained for Zr07 (~1540 MPa). The Ni and Cu containing consolidates are essentially particle reinforced composites. In these cases, the primary deformation occurs in the crystalline matrix (i.e. by dislocation motion), but the properties are strengthened by the inclusion of a stronger second phase (the amorphous metal). For billet Hf13, the ductility/plasticity was very high because of the highly ductile nature of Cu at room temperature in compression.

4.2.5 Results for Billets Hf01 and Hf02

Many of the ECAE processing techniques had beened refined and optimized during the work with the Vitreloy, which allowed efficient and streamlined methods to be used to characterize and consolidate the ARLloy #1 and composites. The initial experiments done were to determine the effect of using a Ni or Cu billet for consolidation (Hf01 and H02, respectively). Figure 4.27 shows flow plane images of the consolidated materials. Notice that the fast extrusion rate causes some tearing in the Cu-canned billet (Hf01) and some cracking in the Ni-canned billet (Hf02). This is likely due to the fast extrusion rate (1.27 mm/s), which being as fast as it was, was not able to keep the billet and powder from reaching temperatures and times that could cause partial devitrification(Figure 4.28). The DSC traces shown in Figure 4.29 point to the partial loss of crystallinity as well. But it was determine that it was more important to obtain samples without cracking or tearing at the risk of some crystallinity in the sample. So, in subsequent extrusions, it was decided to reduced the punch speed by half to minimize this tearing and cracking.

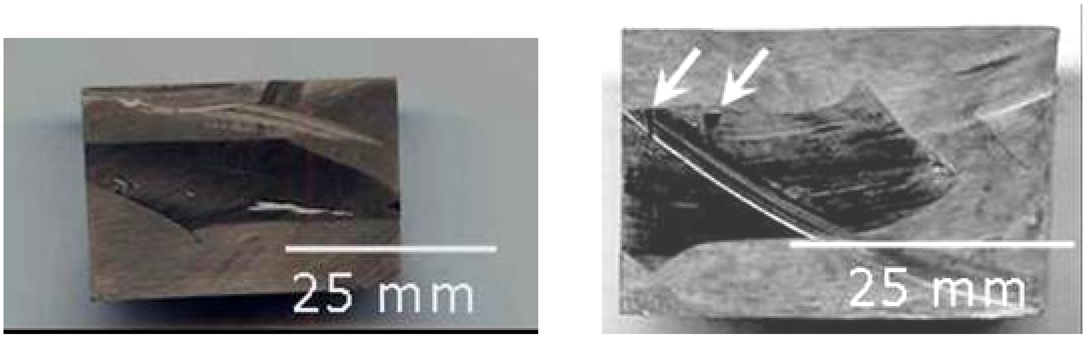

(a) (b)

Figure 4.27 Flow plan scans of billets (a) billet Hf01 – Ni can showing the cracking caused by the fast extrusion rate, and (b) billet Hf02 – Cu can with arrows pointing to tearing that was caused by the fast extrusions.

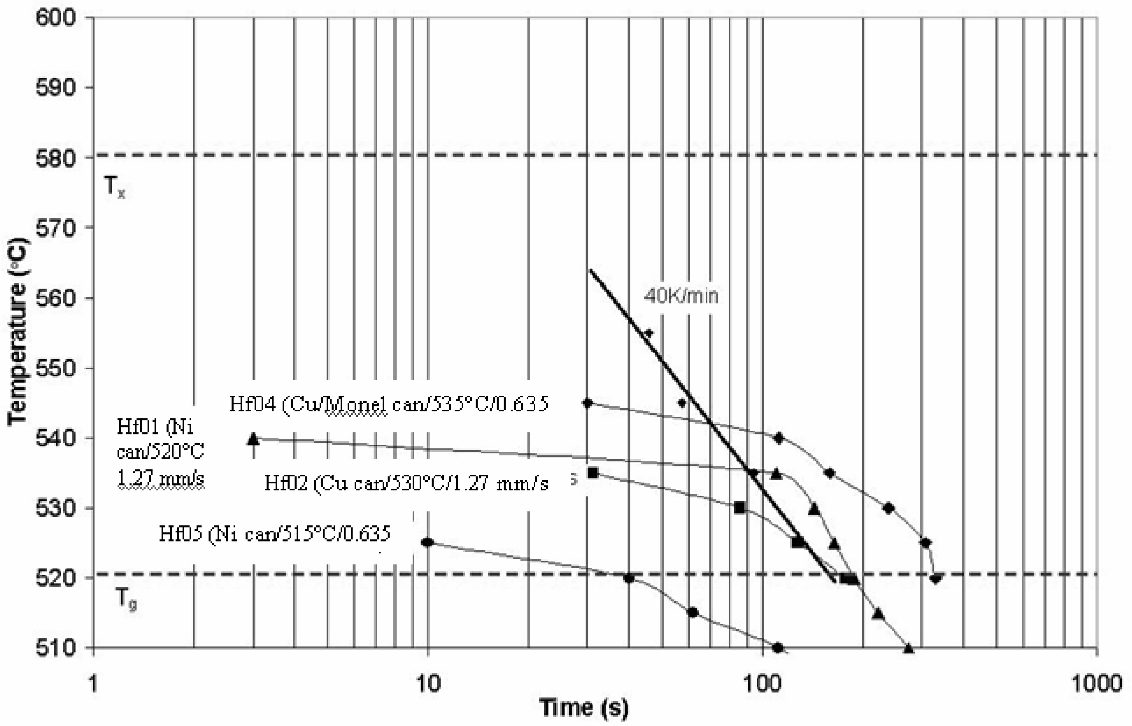

Figure 4.28 Thermal histories of billets Hf01, Hf02, Hf04 and Hf05. Because of the short time available for extrusions in the supercooled liquid region, all extrusions besides Hf05 crossed the TTT boundary at some point, which caused partial devitrification in the consolidated materials.

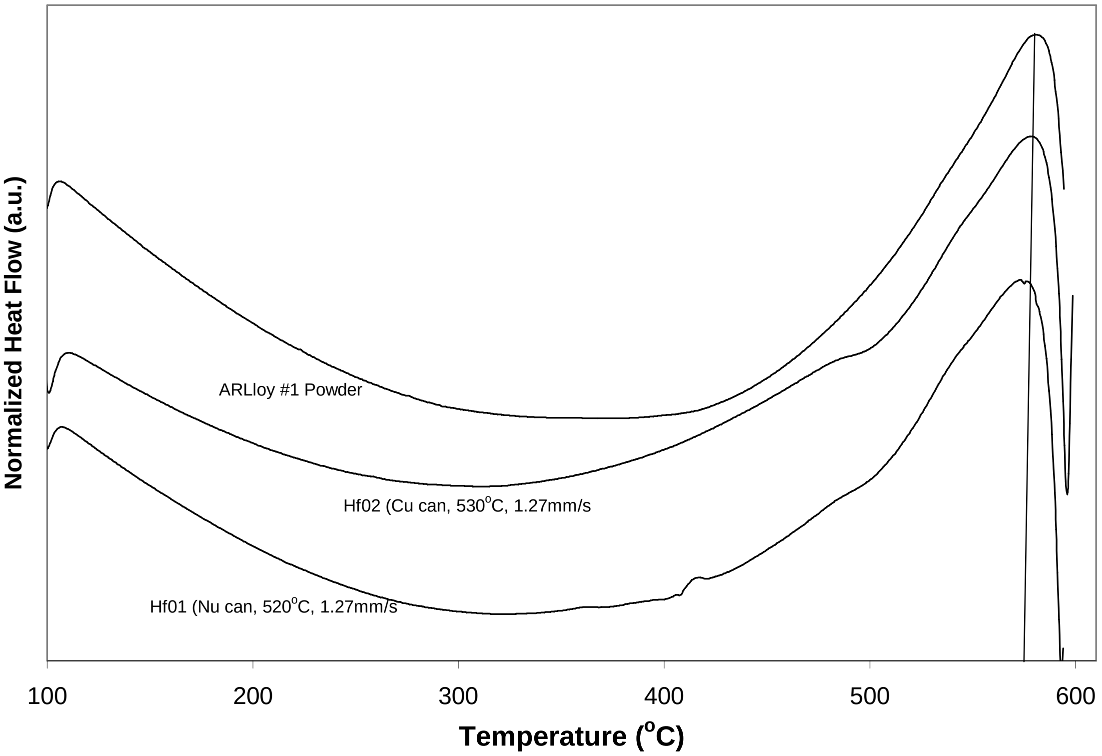

Figure 4.29 DSC traces performed at 40K/min on the starting ARLloy #1 powder and consolidated composite material from billets Hf01 and Hf02. The slight drop in the T_x value indicates that some devitrification has likely occurred.

Figure 4.30 shows the flow plane microstructures of billets Hf01 and Hf02. There is a significant amount of porosity and voids in the case of the Cu can, while in the Ni canned material, the surface is smooth and there are no apparent voids (the dark spots seen on the light micrograph are Vickers microhardness indentations done on the sample). The difference that causes the porosity can be seen in the etched microstructures for each case (Figure 4.31). The Cu can does not provide sufficient hydrostatic pressure during the extrusion event to deform the ARLlo..y #1 particles and “squeeze out” the void space in between the particles. This is true even though the die temperature of the Cu canned case is higher than for the Ni canned case (530°C vs. 520°C). Hf01 shows highly elongated particles with sharp triple points and little, if any voids. The undeformed round particles seen in the micrograph were determined through discussions with the laboratory which manufactured the powder (DOE Ames Laboratory, Ames, IA) to be an unknown impurity particle inadvertently introduced into the amorphous metal powder during the sieving/screen process.

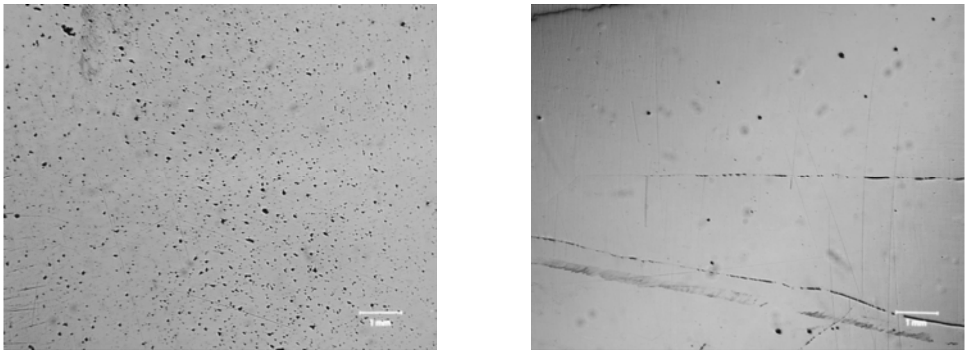

(a) (b)

Figure 4.30 Light micrographs of flow plane microstructures of ARLloy #1 powder consolidated in (a) a Cu can at 530°C: Hf02 and (b) a Ni can at 520°C: Hf 01. The extrusion direction is left to right. The black spots on consolidated material from billet Hf01 are not pores, but rather, microhardness indentations.

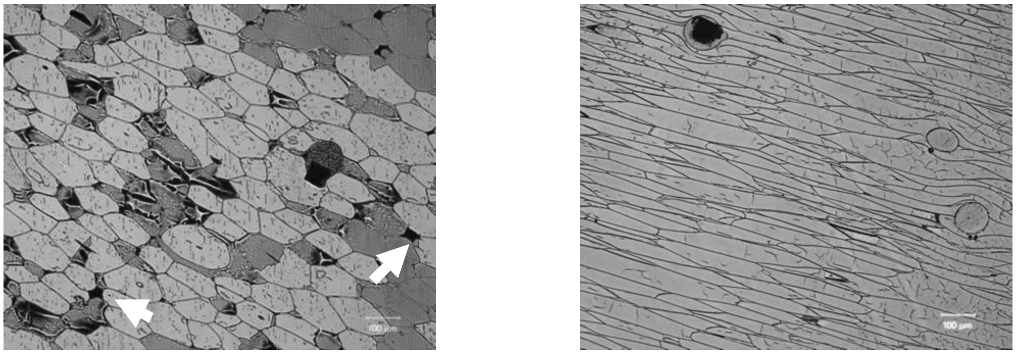

(a) (b)

Figure 4.31 Light micrographs of flow plane microstructures of ARLloy #1 powder consolidated in (a) a Cu can at 530°C (Hf02) where the particles are not elongated and the white arrow indicate voids remaining after consolidation and (b) a Ni can at 520°C (Hf 01) with no voids and highly elongated particles after consolidation. The extrusion direction is right to left.

The thermal history for these two samples has been given in Figure 4.28. Because of the short time available for extrusions both billets are exposed to temperatures that make them appear to cross the TTT boundary. DSC of the samples was done and compared to the initial powder, the curves appear similar but there is a small shift in the T_x after consolidation. As mentioned, both of these observations point to the fact that some devitrification has taken place during the consolidation event, but even so, the microhardness measurements demonstrated shear-banding around the edges of the indentation (not shown) that are typical of predominantly amorphous material and Hf01 and Hf02 had hardness values of HV_{300} = 629 ± 30 and HV_{300} = 641 ± 41 respectively. In addition, x-ray analysis of Hf01 shows similar curves before and after processing (Figure 4.32), which are indicative or retention of amorphous character as well. The reason for this effect has not yet been determined, but will be briefly discussed.

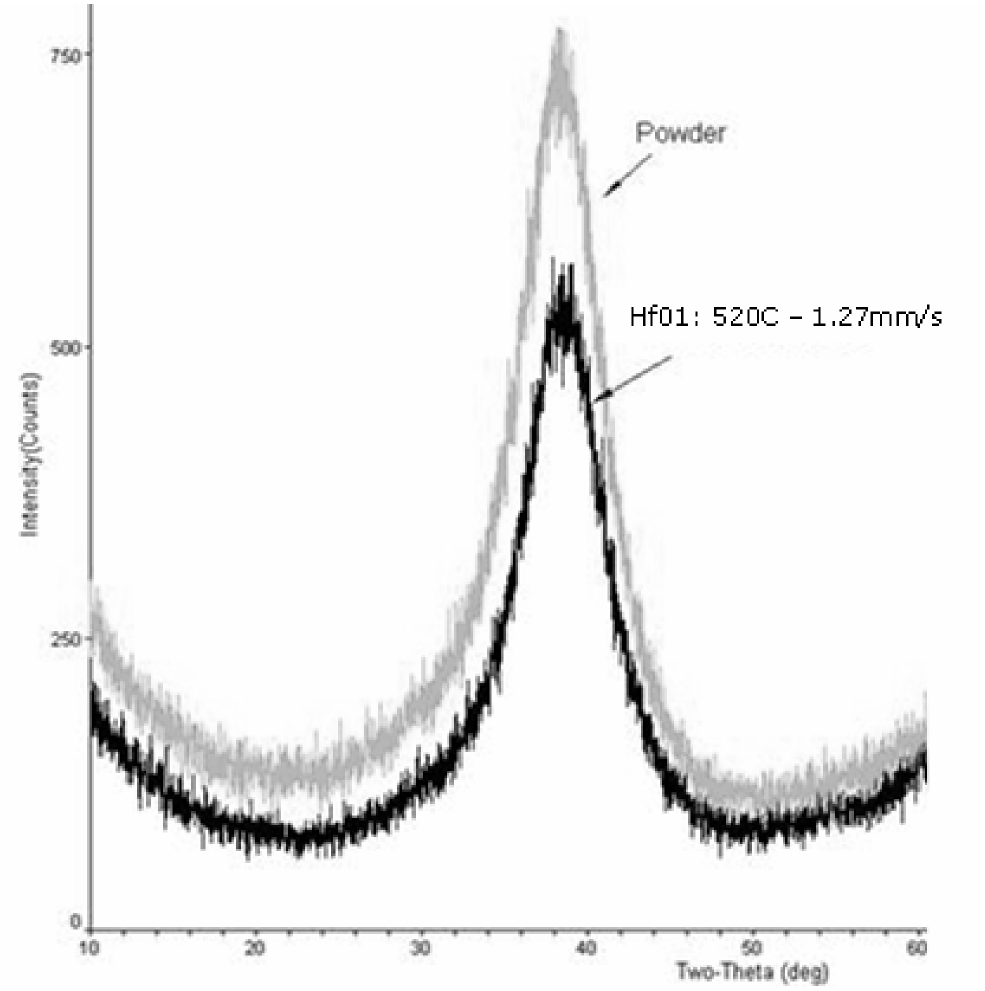

Figure 4.32 X-ray scan of the amorphous ARLloy #1 powder and the consolidated material from billet Hf01. When the scans are digitally overlayed, there is significant difference in the traces, which typically points to the retention of an amorphous structure.

4.2.6 Results for Billets Hf03 to Hf05

The initial extrusions showed that Ni provides a better consolidation environment than Cu, that ARLloy #1 is sufficiently ductile at temperature of 520°C, and that fast extrusions are detrimental to bonding in the large scale samples due to cracking and or tearing in the consolidated materials. The next two experimental sought to use lower punch speeds (0.635 mm/s) with a Ni can (Hf03) and a Monel can with a Cu liner in the hopes of Cu absorbing the residual stresses in the Monel during the billet cool down while still providing a sufficient enough pressure to deform/bond the ARLloy #1 powder. The cross-sections of these two consolidated billets are shown in Figure 4.33. While not shown here, the flow plane analysis showed that there was no cracking or tearing in either of these billets which points to the expected benefits of the slower extrusion rate. Light micrographs of the consolidated regions for samples Hf03 and Hf04 are given in Fig. 4.34. In both cases, there is little porosity seen the samples and the combination of a Monel can with a Cu liner appears to not only prevent cracking, but elongate and deform the particles nearly as well as using a Ni can alone.

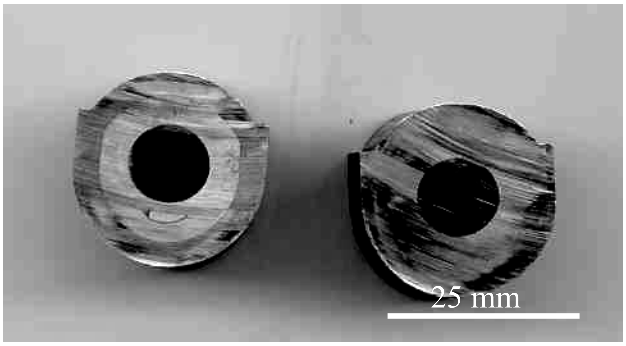

Figure 4.33 Billet cross-sections of Hf03 (Ni can) and Hf04 (Monel can with a Cu liner) showing the geometry of the cans and the internal consolidate after extrusion.

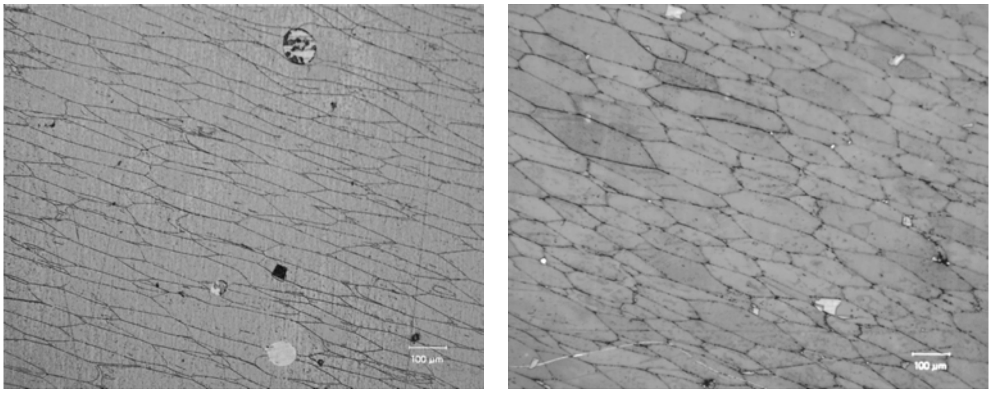

(a) (b)

Figure 4.34 Light micrographs of flow plane microstructures of ARLloy #1 powder consolidated in (a) a Ni can at 510°C and 0.635 mm/s (Hf03) where the particles sharply elongated and (b) a Monel can with a Cu liner at 535°C and 0.635 mm/s (Hf 04) with less elongated particles, but with higher aspect ratios than the Cu can alone (Hf020) and no apparent voids or porosity. The extrusion direction is right to left.

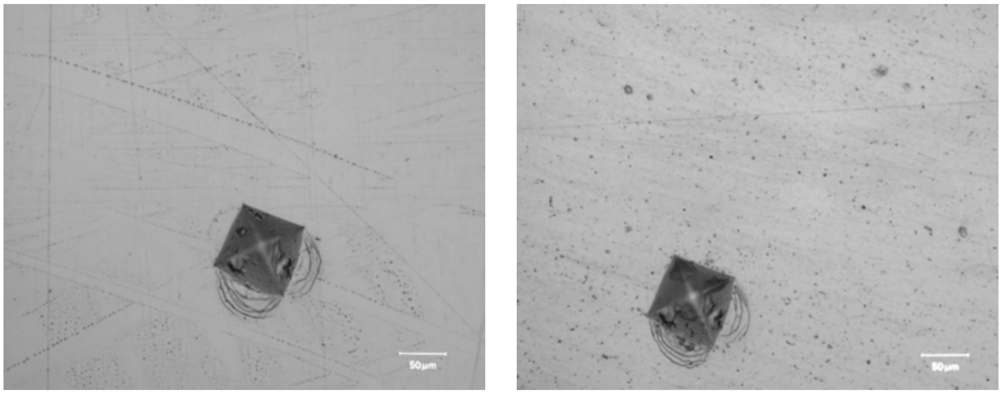

(a) (b)

Figure 4.35 Light micrographs of Vickers microhardness indentations on ARLloy #1 powder consolidated in (a) billet Hf03 (Ni can) and (b) billet Hf04 (Monel-Cu can) showing shear bands indicative of amorphous character. The punch speed in both cases was 0.635 mm/s.

As expected with the slower extrusion rate, the thermal tracking shows that the billets have been exposed to temperature and times which cross the TTT boundary (Figure 4.28). Even though shear bands were generated from microhardness indentations (Fig 4.35), it was seen that the microhardness values were much higher than for the latest two extrusions (HV_{300} = 675 ± 16 for Hf03 and HV_{300} = 700 ± 24 for Hf04 as compared to HV_{300} = 629 ± 30 and HV_{300} = 641 ± 41 for Hf01 and Hf02, respectively). The time at high temperatures likely resulted in a larger amount of devitrification of for samples Hf03 and Hf04.

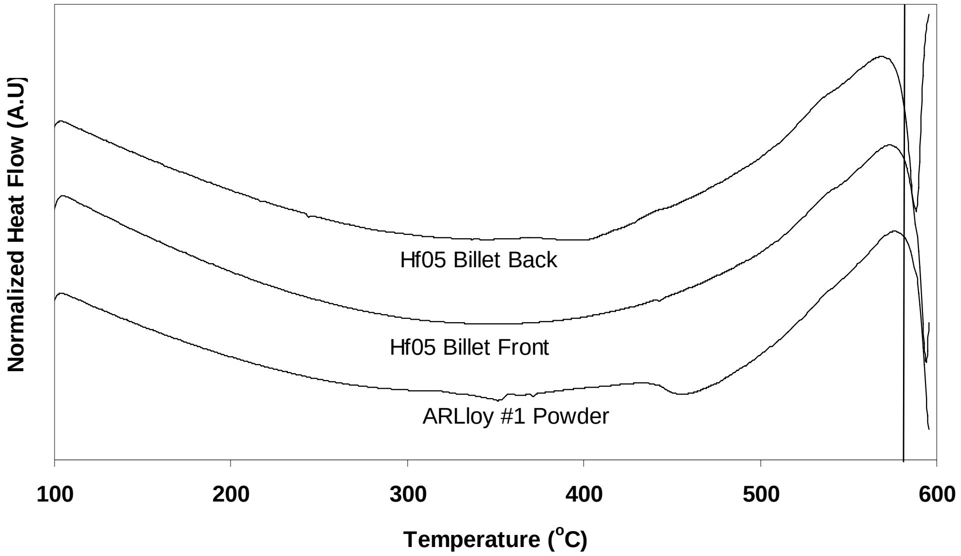

Figure 4.36 DSC traces performed at 40K/min on the starting ARLloy #1 powder consolidated in a Ni can at 515°C. The thermal history was determined from the leading edge of the billet, but the back appears to have partially devitrified as evidenced by the shift in the T_x.

To find out if the extrusion would be crystallized if extruded in a Ni can at a low temperature, billet Hf05 was extruded at 515°C (slightly higher than 510°C, and was thermally analyzed using DSC and x-ray analysis. Observe in Fig 4.28 that the thermal history of the billet is completely to the left of the TTT boundary, which would point to the material being amorphous, but this is a measurement from the leading (front) end of the billet. Analysis of the DSC traces (Figure 4.36) for regions from the front and back of billet Hf05 show that the front region has similar thermal behavior as the starting powder, which would indicate that the front region is likely amorphous. The back portion of the billet shows a decrease in the T_x, which is likely the result of some divitrification from the longer times at temperature and the higher temperatures (due to adiabatic heat generation) that the back end of the billet encounters. This is an indication of partial devitrifications. By overlaying the x-ray trace for the back of Hf05, it shows that there is no change in the structure of the material before or after consolidation (Figure 4.37). It appear as if the sensitivity of x-ray measurement is not enough to quantify the amount of devitrification in ARLloy #1 samples. Discussions were held with the Army Research Laboratory engineers who provided the sample powder, and they too have seen amorphous behavior in this particular alloy even if the was a small amount of crystallization in the sample. This slight devitrification would not prevent large scale amorphous behavior in the consolidate for this particular amorphous alloy.

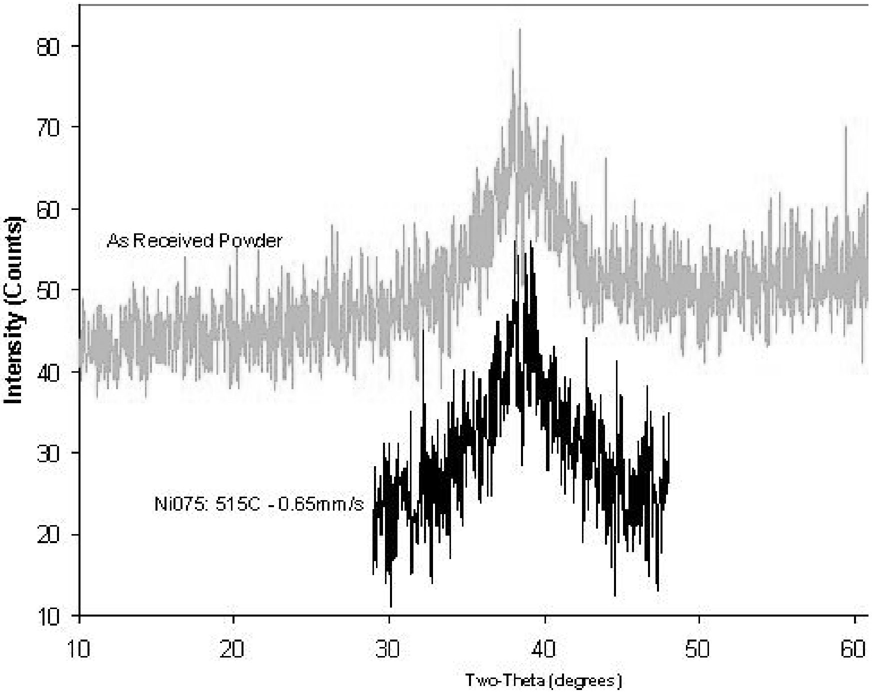

Figure 4.37 X-ray scan of the amorphous ARLloy #1 powder and the consolidated material from billet Hf05. When the scans are digitally overlayed, there is significant difference in the traces, which typically points to the retention of an amorphous structure.

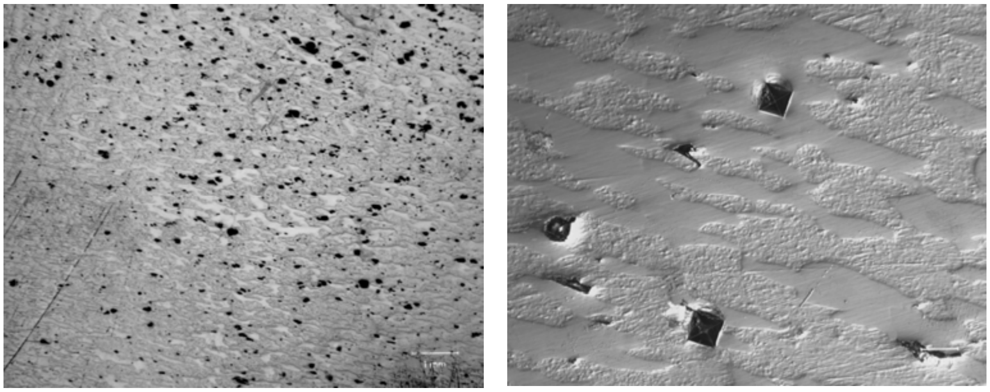

(a) (b)

Figure 4.38 Light micrographs of ECAE consolidated composite material from billet Hf05 containing ARLloy#1 and 60 vol% Alldyne W. (a) The W particles appears to have pulled out fairly easily during mechanical polishing (b) Microhardness indentation (500g, 15 s) showing shear band generation from the edge of the indent.

4.2.7 Results for Billet Hf06

With the knowledge that a small amount of crystallization would not be detrimental and that the primary objective of the sponsor (ARL) was to produce W-containing composites, it was decided that the punch rate of 0.635 mm/s would continue to be used and that Ni-cans would be used without Cu liners to provide enough hydrostatic pressure to infiltrate the amorphous ARLloy#1 with the crystalline W. Billet Hf06 was a Ni can which contained 60 vol% Alldyne W powder and 40 vol% ARLloy#1. The intention was for this billet to be extruded at 530°C with a punch speed of 0.635 mm/s, but got stuck in the tooling and was manually extruded at an unknown speed. The data from the leading end thermocouple indicated that the tooling temperature was ~475°C and the billet was at ~415°C when the extrusion was started. The highest temperature reached during the extrusions was 470°C, which is below the T_g of ~500°C. Light micrographs of this microstructure (Figure 4.38) show that while there appears to be poor infiltration of the ARLloy #1 in with the W particles, that there is also quite a bit of particle pull out at voids in the consolidate. As with the previous monolithic cases, microhardness indentations generate shear bands (Fig 4.38.b). This figure also shows that the areas that appear to be voids are primarily pull-out of W from other regions of W consolidation. It is suspected that the temperature the sample was extruded at did not allow sufficient ductility of the ARLloy#1 powder to completely infiltrate and “trap” the tungsten particles, nor was the temperature high enough to cause significant devitrification in the consolidated composite.

4.2.8 Results for Billets Hf07-Hf10

Similar to Zr11 to Zr14, 2mm x 2mm x 4mm samples were EDM cut for metallographic analysis and mechanical testing. But in this case, residual stress in the Ni can used in billet Hf07 caused the consolidated sample to be friable during the EDM cutting and therefore, pieces were EDM cut from billet Hf02 (a Cu can), so some of the results could be effected by the voids and porosity apparent in that particular sample. Figures 4.39 and the following three figures show the flow plane microstructures for Hf02, Hf08, Hf09 and Hf10. The results seen here are very similar to those given for the Vitreloy 106a and it’s composites.

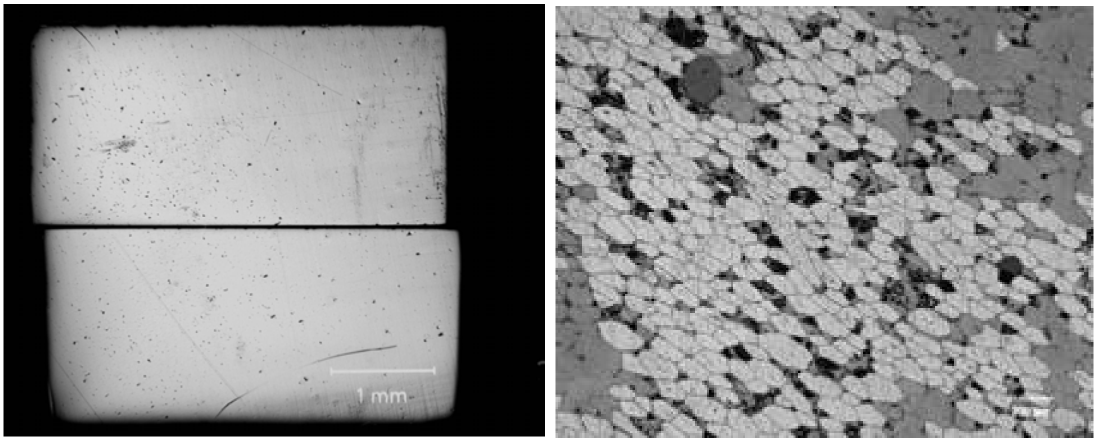

(a) (b)

Figure 4.39 Light micrographs of ECAE consolidated ARLloy #1 from billet Hf02. Consolidated at 530°C with a punch speed of 1.27 mm/s in a Cu can. (a) The ARLloy #1 appears to be consolidated uniformly, but closer observation reveals pores (b) An etched region of the billet flow plane shows minimal particle elongation and voids.

Figure 4.39.a shows the consolidated material from billet Hf02. Figure 4.28 shows that the thermal history of this billet straddled the TTT boundary, and the DSC scans (Figure 4.39) showed minimal shifts in the T_x. This combined with the fact that the sample stayed contigous during EDM cutting point to strong bonds between the particles even though there is little particle elongation and some voids in the consolidated material. Billet Hf08 contains 60 vol% W powder, supplied by Alldyne. Like in the case for Vitreloy 106a, it appears as if the ARLloy #1 has infiltrated the W fairly well with little visible porosity or particle pull-outs (Figure 4.40.b). This case show far fewer particle pullouts than occurred with billet Hf06, and indicates that the higher temperatures allowed better infiltration of the ARLloy #1 into the W.

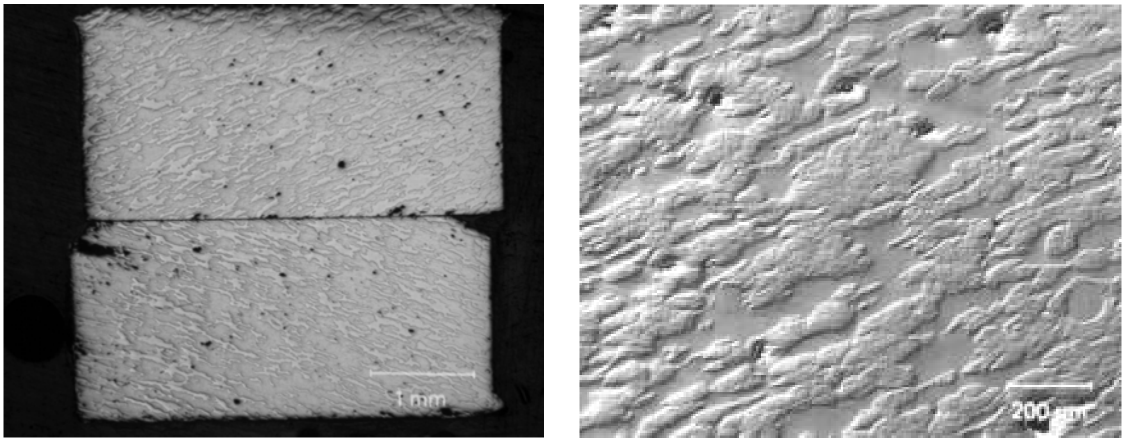

(a) (b)

Figure 4.40 Light micrographs of ECAE consolidated ARLloy #1 + 60vol% W from billet Hf08. (a) The ARLloy#1 appears to be have infiltrated the W well (b) A closer view of the flow plane shows very few particle pullouts, when compare with billet Hf06.

Figs 4.41.a and 4.42.a show the consolidated composites for ARLloy #1 and either Cu or Ni. As was the case with the Vitreloy 106a amorphous powder, the crystalline phase became the matrix phase for the composite. In Figure 4.42.b, it appears as though the Cu matrix in billet Hf09 does not apply enough force to deform the ARLloy #1 particles at the processing temperature of 530°C. But the crystalline Ni and the ARLloy #1 in billet Hf10 infiltrate well at these temperature (Figure 4.41.b)

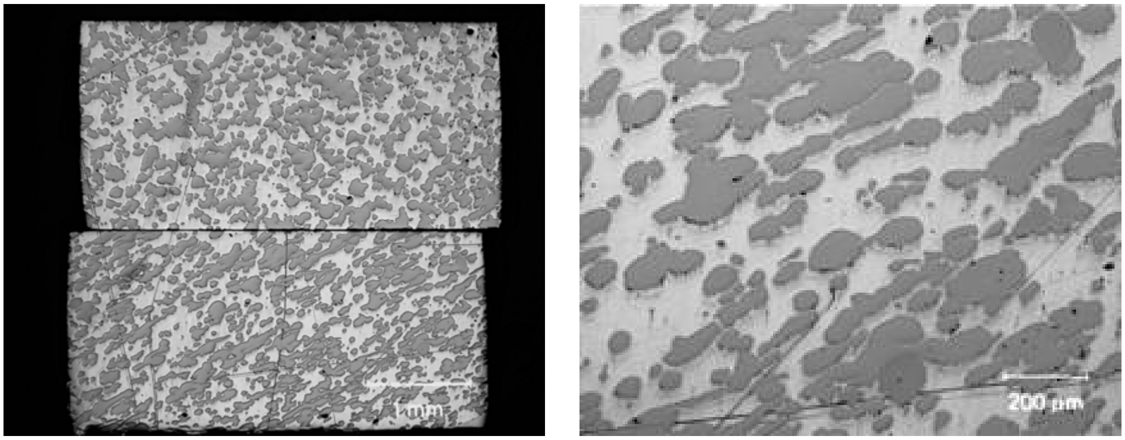

(a) (b)

Figure 4.41 Light micrographs of ECAE consolidated ARLloy #1 + 60vol% Cu from billet Hf09. (a) Flow and longitudinal planes showing that the Cu (the lighter color phase) comprise the matrix. (b) A closer view of the flow plane showing good consolidation of the blended amorphous crystalline powders, but little deformation in the amorphous phase.

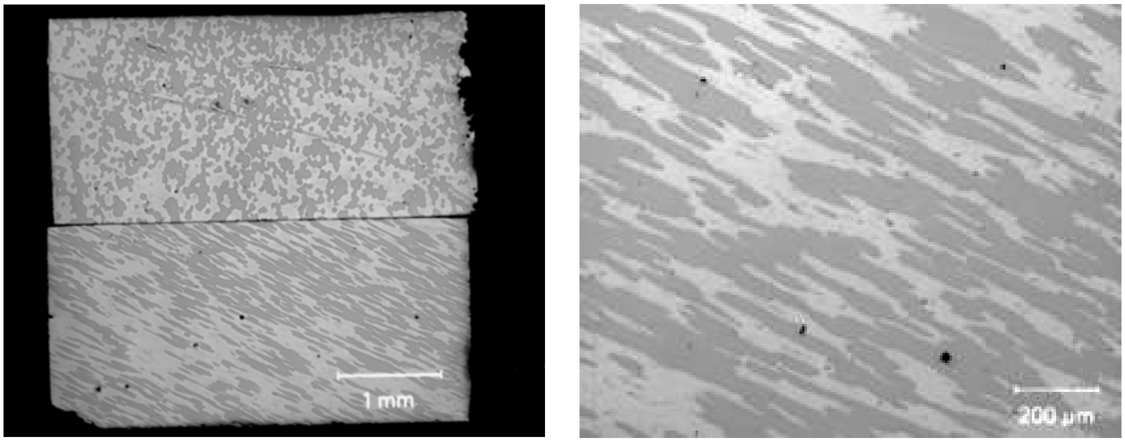

(a) (b)

Figure 4.42 Light micrographs of ECAE consolidated ARLloy #1 + 60vol% Ni from billet Hf10. (a) Flow and longitudinal planes showing that the Ni (the lighter color phase) comprise the matrix. (b) A closer view of the flow plane good consolidation of the blended amorphous crystalline powders, and signficant amorphous particle deformation from the consolidation.

Figure 4.43 shows representative stress-strain curves obtained by uniaxially compressing 2 mm x 2 mm x 4 mm samples of consolidated material from billets Hf02 and Hf08 to Hf09 at a rate of 10^{-4}/s. Again the strain was estimated by scaling the measurement with the modulus of bulk ARLloy#1 (~101 GPa). The strain at failure for bulk consolidate ARLloy#1 is ~2%, at 1.7 GPa. Like theVitreloy 106a + 60 vol% W composite, the ARLloy #1 + 60%W composite also appears to have some plasticity (%EL = 1.6%), but the strength is not very high (~700 MPa). Again, the Ni and Cu containing consolidates are essentially particle reinforced composites. Both samples this time have near unlimited the ductility/plasticity, which might indicate that a stronger bond forms between the Cu or Ni and the amorphous phase at the consolidation temperature of 530°C.

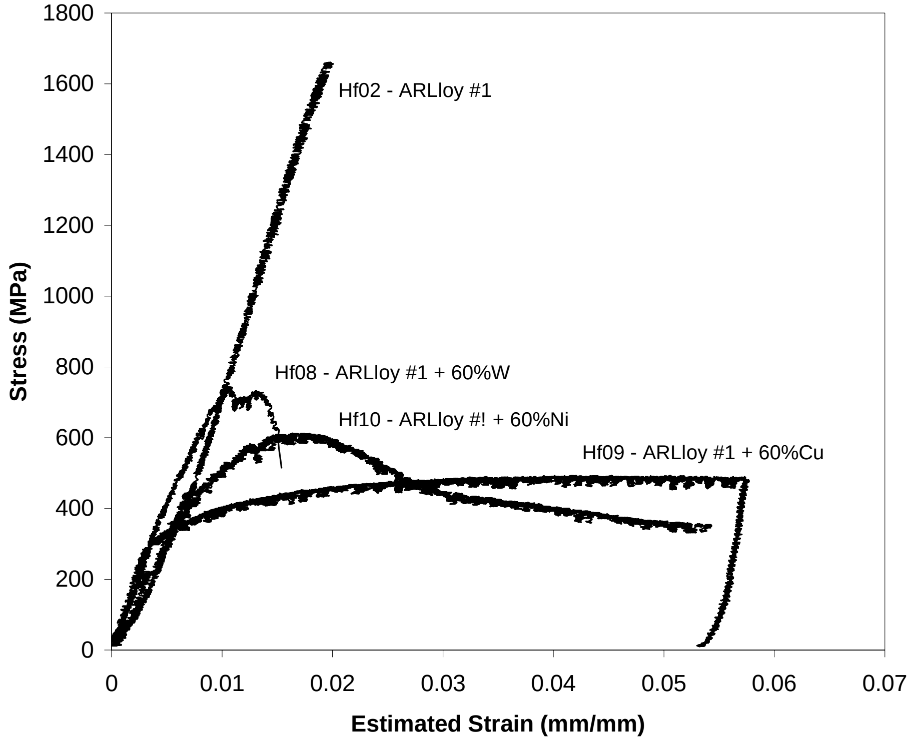

Figure 4.43 Compression stress-strain curves for ECAE consolidated ARLloy #1 and composites containing 60 vol% W, Ni or Cu crystalline phase. The strain shown is estimated by scaling the measured results and multiplying by a factor determine from accurate measurement of the amorphous metal modulus.

CHAPTER V

DISCUSSION

5.1 The Effects of Particulate Characteristics on Consolidation

5.1.1 Behavior of Amorphous Powder as a Function of Oxygen Content

Comparisons of the TTT boundaries in Figure 4.2 for the Vit106a with 780 ppmw O_2 and 1280 ppmw O_2 demonstrate the larger processing window offered by the lower oxygen content material. Differential scanning calorimetry (DSC) analysis of the powders indicates fully amorphous character with a T_g of 398°C and a T_x of 460°C ($\Delta T = 62$°C) for the Batch 1 powder and a T_g of 403°C and a T_x of 480°C ($\Delta T = 77$°C) for the Batch 2 powder (Figure 4.1). When the crystallization temperature for the Batch 1 Vitreloy 106a is compared to the values obtained for the Batch 2 Vitreloy 106a, it is apparent that the increased oxygen content present in Batch 1 material lowers the crystallization temperature. The largest benefit provided by the lower oxygen content is the added time afforded for processing between T_g and T_x. For this reason, slower extrusions could be performed (0.508 mm/s compared with 6 mm/s for the Batch 1 Vit106a). The slower extrusion rates also effectively lower the temperature rise as the billet is deformed (Figure 4.3). This adiabatic heat spike can cause the temperature of the consolidate to approach the TTT boundary and partial devitrification could occur. The larger processing window also results in the possibility of multiple extrusions to promote better particle-to-particle bonding.

The oxygen content also appears to affect the thermal stability of the consolidated powder. Figure 4.19.a shows the DSC analyses of the initial powder and the post-extruded billets containing the Batch 2 Vitreloy 106a. It is clear that there is little difference in the T_g and the T_x of the powder and the consolidated material (Figure 4.19.b). Billet Cu058, on the other hand, experiences a decrease in T_x and enthalpy of crystallization when compared to the initial powder indicating that some divitrification may have occurred during processing, indicating that a lower oxygen content can improve the thermal stability of the amorphous metal.

The concern with oxide surface layer verifies the observations of others who have seen detrimental behavior in $Zr_{65}Al_{10}Ni_{10}Cu_{15}$ powders consolidated by conventional area reduction extrusion [24,62,86]. Comparisons are made between “open” and “closed” powder metallurgy processing. “Closed” processing refers to the steps from powder atomization to consolidation by warm extrusion being done in vacuum or argon environments such that the oxygen content is less than 0.5 ppm. “Open” processing is when the powder is exposed to air from the sieving step to the precompaction of the powder into a Cu can. The results show that higher strengths and improved bonding were observed for lower extrusion ratios in the “closed” powder metallurgy processing case. The oxygen content was measured to be 0.08 and 0.11 mass.% for “closed” and “open” processing, respectively, and 0.05 mass.% for the starting powder. The differences between the values for the open and closed processing are attributed to the oxide layer thickness on the powder particles. These results agree with our observations of increased ductility and processing opportunity provided by a powder with less oxygen.

5.1.2 Consolidation as a Function of Crystalline Phase Characteristics

As previously mentioned, a number of different pure W powders were used in attempts to ECAE consolidate an AMMC. From the voids present in Figures 4.5 to 4.7, it is clear that oxide scale on the surface of the crystalline phase particles can severely hinder the ability of the particle to bond with either itself, or the amorphous phase. The hope was that by coating the W particles with Ni, this problem could be circumvented. When comparing the amount of particle pull-out in Figures 4.5 to 4.7 with Figures 4.12 to 4.13, it is evident that the Ni-coating does aid with the bonding of W to itself and the amorphous Vitreloy phase, but there is a catch. During the coating process, the fine particles of Ni-coated W tend to agglomerate (Figure 4.11), and are not completely infiltrated by the Vitreloy 106a during consolidation, and can pull out during polishing (Figures 4.12 and 4.14).

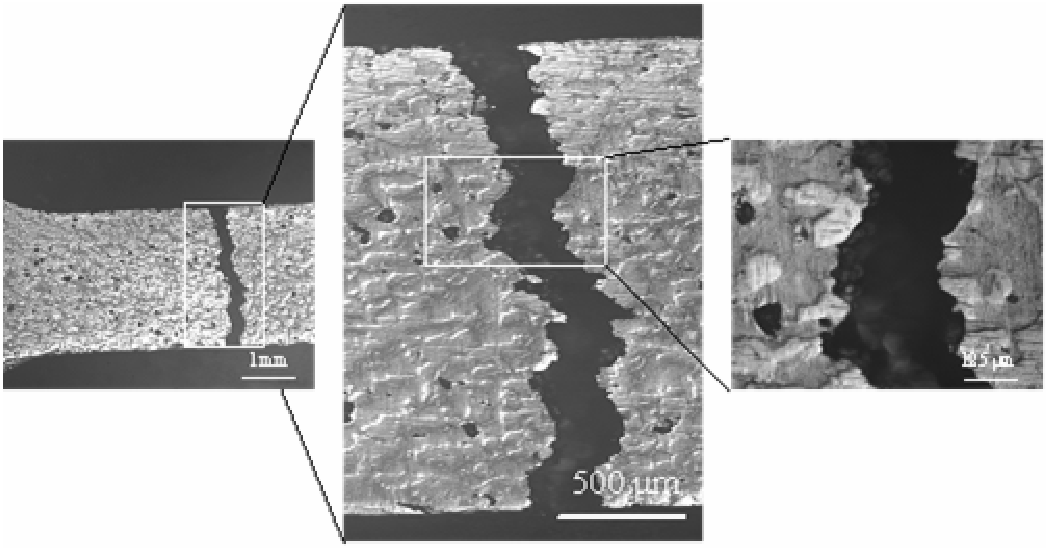

Figure 5.1 Light micrographs of the tensile test flow plane surface of billet Zr04 (50 vol% Ni-coated W) showing regions where W agglomerate pull-out has occurred. It is likely that these voids cause stress concentrations which contribute to the brittle behavior of the composites under tensile loading.

The negative effect of the particle pull-out can most readily be seen in the early failure of the tensile test samples with no plastic deformation. Figure 5.1 shows the flow plane of a polished and tested sample from billet Zr04. It is suspected that W pull-outs occur at the edge of the tensile samples, causing flaws and stress concentrations which result in premature brittle failure under tensile loading (Figure 4.16). The benefits of a clean, spherical crystalline powder, such as the Alldyne W, are seen in Figures 4.22 and 4.40 where there are few, if any, W particle pull-outs after polishing. This is also likely the case with the crystalline Ni and Cu produced by HPGA at Ames Laboratories. This powder was also reported to be clean and spherical, and as will be seen in the next section, are more likely to form a strong bond with the amorphous metal than W.

Table 5.1 Atomic radii for elements used in Vitreloy 106a, ARLloy and for W

Element	Atomic Radius (nm)	wt% in Vitreloy 106a	wt% in ARLloy #1
Zr	0.216	58.5	---
Hf	0.216	---	71.3
Nb	0.208	2.8	---
Cu	0.157	15.6	16.2
Ni	0.162	12.8	7.6
Al	0.182	10.3	2.6
Ti	0.200	---	2.2
W	0.202	---	---

5.1.3 Diffusion and Atomic Transport Issues

In Chapter II, the idea that atomic diffusion between the matrix and the reinforcement phase is necessary to chemically bond the material was presented. The reality is that this is a very complex process when amorphous metal is involved. It has been observed that there is a discontinuity in the normally linear Arrhenius diffusion plot (Diffusivity (m^2/s) vs. 1000/T (K^{-1})) which corresponds to the beginning of the supercooled liquid region, i.e. the glass transition temperature [87]. At this temperature, given sufficient time, the amorphous alloy will relax and the small atoms will break away from the amorphous matrix and diffuse. As the temperature increases, more of the smaller atoms, and some of the larger atoms become mobile. But given enough time, and high enough temperatures, localized ordering will begin to occur, resulting in detrimental crystallization.

Table 5.1 gives the atomic size for the elements used in the Vitreloy 106a, ARLloy #1, and W. Activation energy increases with increasing atomic radius because the larger atoms need more space within the lattice to diffuse. Therefore, it is theorized that the Cu and Ni present in both amorphous alloys will diffuse the fastest and easiest, and therefore, the crystalline Ni and Cu powder should bond well with the amorphous particles, and likely better than the W, which has a much larger atomic radius. X-ray analysis done on similar amorphous alloys $(Hf_xZr_{1-x})_{52.5}Cu_{17.9}Ni_{14.6}Al_{10}Ti_5$) by Gu et al. shows that the final crystallization products are $CuHf_2$ and $Al_{16}Hf_6Ni_7$ for the Hf-based alloy and $CuZr_2$ and Zr_2Ni for the Zr-based alloy [88]. This demonstrates that the smaller atoms (Cu, Ni and Al) are more mobile and are more likely to form a chemical bond with adjacent materials. The oxide coatings on Ni and Cu are also known to be thin and stable at room temperature, but fragile at higher temperatures. Warm ECAE processing will increase the surface area of the particles during deformation and fracture the oxide surface layer, thereby exposing clean, fresh surfaces for bonding.

5.1.4 Amorphous Alloy Glass Formation and Density Considerations

As mentioned previously, the selection of the Vitreloy 106a and ARLloy #1 amorphous alloys was based on their wide supercooled liquid region, and in the case of the Vitreloy 106a, the sheer amount of research done on Zr-based amorphous metals. In this section, two major differences (the supercooled liquid temperature region and the amorphous alloy density) will be discussed.

Figure 4.2 shows the TTT boundaries for both the Vitreloy 106a alloys and for ARLloy #1. From this figure, it is apparent that the processing temperature for the ARLloy #1 (520°C – 580°C) is much higher than for Vitreloy 106a (400°C – 480°C), and that the times to the TTT boundary are shorter for the ARLloy#1 (~150s at T_g) than for the Vitreloy 106a (>2000s at T_g). Hf-based amorphous metals fabricated by direct substitution of Hf for Zr in typical Zr-based amorphous metals has been researched by Gu et al. The similarity in size for Zr and Hf (0.216 nm) and chemical similarities would make it seem that the amorphous alloy would have a higher density and similar glass forming ability (GFA), but this is not the case. The researchers found that replacing the Zr with Hf reduced the GFA in every case, and that increasing the Hf content resulted in increases in both T_g and T_x, and decreases in ΔT [89]. The supercooled liquid region tends to be wider and the T_g lower for alloys which have good glass forming ability [90]. The large amount of Hf (~71 wt %) and high melting temperature of Hf (~2227°C) likely contribute to the higher T_g and T_x values, and faster times (higher temperature, and hence, enhanced diffusion) to crystallization. It is theorized that, given the mobility of Cu and Ni at high temperatures, that crystallization can occur more easily for an alloy due to the “confusion principle”, which postulates that a larger number of components improves the GFA of an amorphous alloy by hindering the mobility of atoms which migrate to form crystalline phases [91].

One of the objectives of the initial sponsor of this research (DARPA-DOD) and the supplier of the W and ARLloy #1 powders (Army Research Laboratory) was to investigate the concept of fabricating AMMC’s as a replacement material for depleted uranium (DU) for armor penetration applications. Zr-based alloys have been shown to shear localize during penetration, and addition of the W gives the AMMC the density, strength and hardness necessary for penetrator performance. But a significant deterrent to the use of Zr-based alloys is their low density (~5-7 g/cm^3), which, even when combined with W (~19 g/cm^3), produces low density composites (~11-15.5 g/cm^3). It is likely that improved KEP performance will be demonstrated by increasing the density of the amorphous matrix in such composites, hence the use of Hf-based amorphous metal.

Table 5.2 Measured and theoretical densities for ECAE consolidated Vitreloy 106a, ARLloy, and composites.

Sample ID	Vol % Cryst.	Measured density (g/cc)	Theoretical density (g/cc)	% Theoretical density (%)
Zr11	0	6.61 ± 0.08	6.70	98.7
Zr12	60% W	14.02 ± 0.16	14.20	98.7
Zr13	60% Cu	8.22 ± 0.14	8.06	>100
Zr14	60% Ni	8.00 ± 0.09	8.01	99.9
Hf02	0%	10.98*	10.90	>100
Hf08	60% W	15.79 ± 0.50	15.88	>100
Hf09	60% Cu	10.00 ± 0.08	9.74	>100
Hf10	60% Ni	9.85 ± 0.17	9.69	99.4

* Only one sample was available for measurement

Cast ARLloy#1 has shown to have a density of 10.9 g/cm^3 as compared to Vitreloy 106a, which has density of 6.7 g/cm^3. So the density improvement by using a ARLloy #1 matrix over a Vitreloy 106a matrix is calculated. The measured densities of the consolidated amorphous metals and composites are shown in Table 5.2. Nominal densities were determined on 2 mm x 2 mm x 4 mm EDM cut samples by measuring the volume with calipers and the mass on a microbalance. The rule of mixtures was used to calculate the theoretical densities with the following values: 6.7 g/cm^3 for Vitreloy 106a, 10.9 g/cm^3 for ARLloy#1, 19.2 g/cm^3 for W, 8.96 g/cm^3 for Cu and 8.88 g/cm^3 for Ni. The crystalline phase densities were found at www.matweb.com. It should be noted that the measured densities are only rough approximations due to the size of the samples and the inability to determine pore concentration, but comparisons can still be made. The density of the ARLloy#1 is ~66% higher than that of the Vitreloy 106a, but the increase in density of the ARLloy#1 + 60vol%W AMMC is only ~13% higher than that of the Vitreloy 106a + 60 vol% AMMC. While the improvement is small, it still is a step toward obtaining a higher density AMMC for penetrator applications.

5.2 The Effects of Processing Conditions on Consolidation

5.2.1 The Effect of Can Material Properties

The biggest factors involved when choosing a can for consolidating amorphous metal powders are the yield strength, the hardness, and the thermal conductivity of the can material. The properties are listed in Table 5.3. Figures 4.17, 4.31 and 4.34 show the effect of the can material yield strength on the deformed particle geometry after consolidation. Clearly, the hydrostatic environment provided by a Ni can during the consolidation event causes larger particle deformations than Cu or even Monel with a Cu liner for equivalent extrusion temperatures. To try to deform the amorphous metal powders more significantly when using a Cu can or liner, higher temperatures were used for the extrusions, e.g. Hf01 (Ni can) at 520°C, Hf02 (Cu can) at 530°C and Hf04 (Monel + Cu can) at 535°C). The effects of the extrusion temperature will be discussed in the following section.

Table 5.3 Flow Strength, microhardness and thermal properties of the ECAE can materials. All properties except the microhardness are from www.matweb.com.

Can Material	Yield Strength (MPa)	Vickers Microhardness (HV_{300}) @20°C	Thermal Conductivity (W/m-K)	Coefficient of Thermal Expansion (μm/m-°C) @ 20°C
Cu	33.3	78 ± 9	385	16.4
Ni	59	198 ± 7	60.7	13.1
Monel	170*	---	21.8	13.9

*at 425°C

Observations of the AMMCs containing W, such as Figures 4.22.b and 4.40.b show minimal deformation in the W phase, and mostly infiltration by the amorphous metal. Even with multiple extrusions (Figures 4.12 - 4.14) there is little, if any deformation in the W particles. This can be explained by knowing the yield strength of W is ~750 MPa, and the Vickers microhardness which is $HV_{300} = 313 \pm 8$. The strength/hardness of the W is so high compared to the can materials that deformation of the W, even at temperatures as high as 400°C – 530°C does not result in significant elongation of the W particles.

The thermal conductivity of the can material is important from the perspective that if it is too low, there may not be sufficient time to get the encapsulated powder to uniform temperatures for consolidation. Observe from Figure 4.3 that the Cu canned material (Cu058) heats up more quickly (~ 40°C/min) as it approaches T_g as compared to the Ni canned material (Zr09) which approaches T_g at a rate of ~ 26°C/min. This small difference can have a major effect if the amorphous alloy being consolidated which has limited time in the supercooled liquid region before crystallization. Unfortunately, there are no commonly available materials that combine a high thermal conductivity and high yield strength, and Ni provides marginal values for both at a reasonable cost.

5.2.2 The Effect of Processing Temperature and ECAE Route

While the importance of consolidating the amorphous metals and AMMCs in the supercooled liquid region has been addressed, the effects of the processing temperature within that region needs some discussion. Microstructural examination of the Vitreloy 106a matrix AMMCs containing W (Figures 4.12-4.14) shows that infiltration and consolidate morphology appear to be independent of temperature or multiple extrusions by ECAE routes 2B or 2C. The range of processing temperatures used in this case are all within the first 30°C of the supercooled liquid region (Figure 4.15), and so there is not much difference in the powder viscosity in this temperature range. Similar results are seen for consolidated bulk Vitreloy 106a. With a proper can material to apply sufficient hydrostatic pressure, significant particle deformation and full compaction is achieved after only one extrusion as can be seen in Figures 4.17.b and 4.21.b. The 10°C difference in processing temperature for these two billets (Zr09 – 430°C and Zr11 – 420°C) appears to have little or no effect on the morphology of the consolidated particles or the density of the consolidate.

Billets Hf01 and Hf02 also illustrate the idea that the hydrostatic load applied by the can is far more of a factor in particle deformation and bonding than the temperature, if the processing is being done in the supercooled liquid region (Figure 4.31). Billet Hf01 is a Ni can extruded at 520°C, and Hf02 is a Cu can extruded at 530°C. Clearly, the higher temperature does not compensate for the lower hydrostatic pressure applied by the Cu can, and voids are present in this alloy. The same principle is seen with billets Hf03 (Ni can – 510°C) and Hf04 (Monel-Cu can – 535°C) in Figure 4.34. Even with a 25°C decrease in processing temperature, the Ni-canned material shows more elongated particles and sharper triple junctions. Billet Hf06, which got stuck in the tooling and was manually extruded at a temperature below T_g, illustrates the effect of consolidation at too low a temperature. Below T_g the ARLloy #1 was not viscous enough to surround and lock in the W particles.

Even though the microstructures showed little change in morphology as a function of extrusion temperature, there is still an effect on the crystallinity as evidenced by changes in the microhardness values. Figure 5.2 plots the Vickers microhardness as a function of the die/extrusion temperature for both amorphous alloys. Observe from this plot that there is a much smaller slope associated with the Vitreloy 106a than for the ARLloy #1. Recall that the thermal histories for the Vitreloy 106a are far from the TTT boundaries, so little, if any crystallization should occur. The ARLloy #1 extrusions approached or crossed the TTT boundaries signifying that partial crystallization occurred during consolidation. The increases in microhardness with increased processing temperature can be associated with increased devitrification of the amorphous alloy. This is just another demonstration of the reduced thermal stability offered by the Hf-based ARLloy. The Vitreloy 106a, as expected, is thermally stable, and shows only minor increases in microhardness with increased processing temperature.

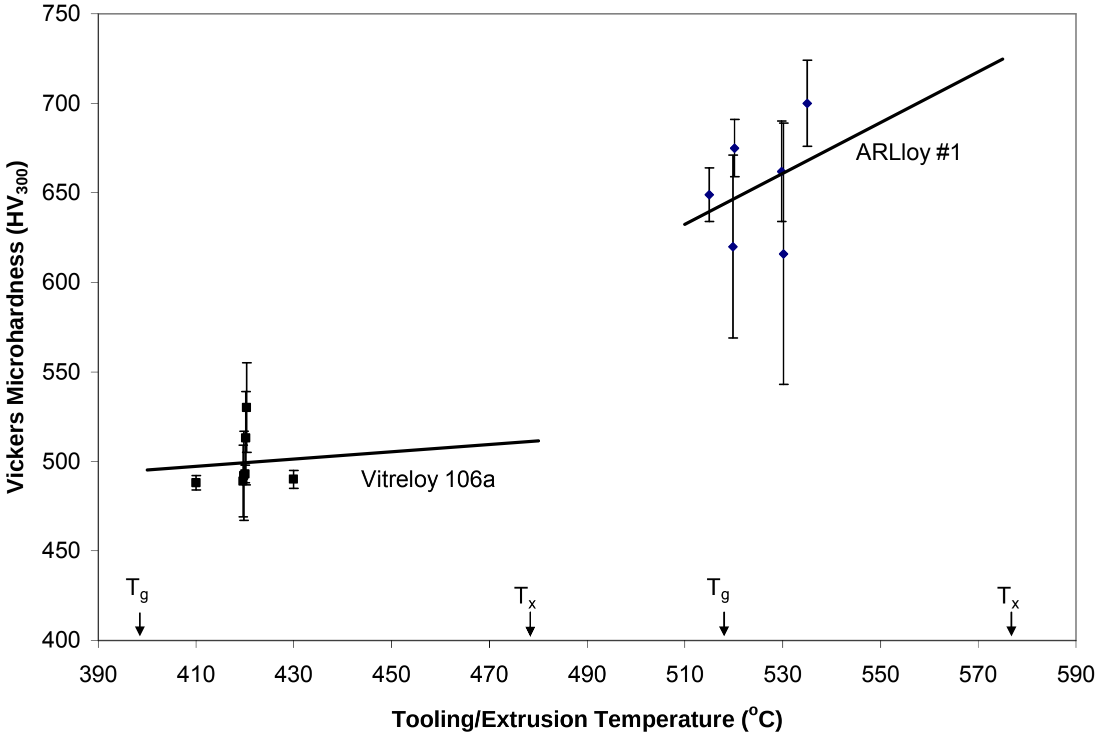

Figure 5.2 Vickers microhardness (HV_{300}) for Vitreloy 106a or ARLloy #1 as a function of processing temperature. The Vitreloy demonstrates thermal stability (i.e. little devitrification) by experiencing only minor increases in microhardness with increasing processing temperature. The ARLloy#1 has much poorer thermal stability and undergoes more substantial devitrification during processing.

5.2.3 The Effect of Extrusion Rate

The TTT boundary was used to determine the time available for extrusions at a particular temperature in the supercooled liquid region for each amorphous alloy. This boundary was used to determine at what speed the extrusions should be performed so as to not cross the TTT boundary. But other factors, such as adiabatic heating from the can deformation can play a significant role in maintaining proper temperatures. Figure 4.3 shows that there is a large spike in temperature (~25°C) for billet Cu058, which was extruded at 6 mm/s. The effect of this spike on the thermal history is seen in Figure 4.4 where there is a portion of the trace which deviates from a smooth curve at high temperatures. By reducing the punch speed to 0.508 mm/s and 0.127 mm/s, these large spikes were avoided, even though the can material (Ni) has a higher yield stress than the Cu cans that were previously used.

Kawamura et al. give an equation that predicts the rise in temperature due to adiabatic heating for conventional extrusion [62]:

$$\Delta T_e = 1.1 \times 10^4 \cdot V_e^{0.64} \cdot \frac{P_e}{\rho \cdot C_p} \qquad \text{Eq. 5.1}$$

Where V_e is the punch speed, P_e is the pressure during extrusion, ρ is the density, and C_p is the specific heat. The density for $Zr_{65}Al_{10}Ni_{10}Cu_{15}$ amorphous alloy is 6.7 g/cm^3, and C_p is estimated to be 30 J/mol-K [62]. These values are similar to Vitreloy 106a, and therefore will be used in calculations. The maximum punch load is calculated to be approximately 0.679 GPa for the 19 mm x 19 mm cross-section cans, and 0.500 GPa for the 25.5 mm dia. cross-section cans assuming a max force of 245 kN (typical force value during) during extrusions. Eq 5.1 then predicts the temperature rise for Vitreloy 106a to be 117°C for a 6 mm/s extrusion in a square can, 24°C for a 0.508 mm/s in a square can and 7°C for a 0.127 mm/s extrusion in a round can. The latter two values are very close to the actual temperature rise that is observed during extrusions, and the reason that the extrusions are begun at temperatures 10-20°C below the tooling temperature, i.e. the adiabatic temperature spike pushes the temperature of the powder in the billet to that needed for consolidation.

5.3 Discussion of Hardness and Mechanical Properties

5.3.1 Mechanical Properties of the Consolidated BMG

Table 5.4 summarizes the mechanical properties observed for the ECAE consolidated bulk amorphous metal and AMMC's (Figures 4.16, 4.23 and 4.46). Since the mechanical response of the composites which contain the crystalline Cu or Ni are probably dominated by deformation in the crystalline phase, the mechanical properties of these composites will not be addressed.

Table 5.4 Summary of mechanical properties and microhardness for consolidated Vitreloy 106a, ARLloy #1 and W-reinforced AMMC's. The microhardness values are for the amorphous phase only.

Billet ID	Vol.% W	ECAE Route	Loading	E (GPa)	UTS (MPa)	%EL (%)	HV_{300}	HV (GPa)
058 (V106a)	0	1A	Comp.	80	1640	2.3	469±17	4.60±0.17
Zr04	50	1A	Tension	159	---	---	489±20	4.80±0.20
Zr07	60	1A	Tension	205	---	---	---	---
Zr07	60	1A	Comp.	206	1540	1.9	---	---
Zr11	0	1A	Comp.	91*	1480	1.6*	530±25	5.20±0.25
Zr12	60	1A	Comp.	94*	1065	2.2*	---	---
Hf02	0	1A	Comp.	97*	1660	2.0*	620±51	6.10±0.50
Hf08	60	1A	Comp.	71*	740	1.5*	---	---

* Recall that the strain value was corrected by scaling the measured strain by a proportionality constant.

For most polycrystalline metals, the yield strength correlates well with the microhardness using the Tabor relationship:

$$\sigma_f = 1/3*HV \qquad \text{Eq. 5.2}$$

where σ_f is the stress at failure and HV is in GPa units. This theoretical equation has recently been used to correlate the strength of monolithic amorphous metal alloys with microhardness as well. Predictions using this equation are given in Figure 5.3 for Vicker microhardness loads from 50 to 1000g. It appears as though the Tabor rule overpredicts the fractures strength of the amorphous alloy in both cases. This may be an indicator of non-ideal bonding conditions in the consolidated material.

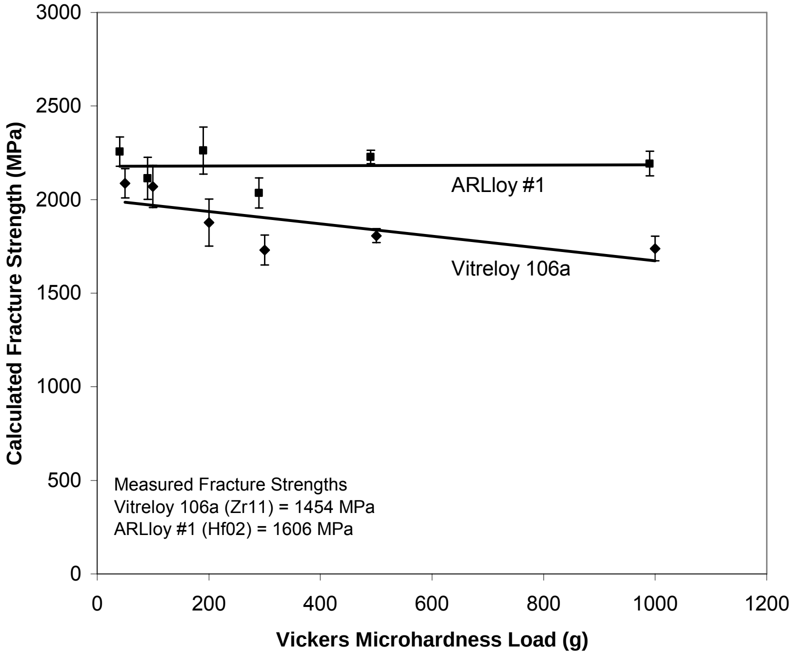

Figure 5.3 Fracture strength calculated from Vickers microhardness measurements (50 – 1000g) with the Tabor relationship. The predicted values are higher than those measured for the ECAE consolidated Vitreloy 106a and ARLloy #1.

The properties obtained in other consolidated or cast alloys similar to Vitreloy 106a and ARLloy #1 are presented in Table 5.5. The fracture strength of the ECAE consolidated samples are observed to be slightly less than those of the cast alloys, and the fracture strains are near the same as for cast alloys. The moduli are also seen to be similar. Therefore, the assumption that bond strength is not high from the predictions of the Tabor equation may not be completely valid.

Table 5.5 Summary of mechanical properties for consolidated Vitreloy 106a, ARLloy #1 and comparable cast alloys tested in compression.

Name	Composition (wt%)	E (GPa)	σ_f (MPa)	%EL (%)
Vitreloy 106a (Cu058)	$Zr_{58.5}Nb_{2.8}Cu_{15.6}Ni_{12.8}Al_{10}$	80	1640	2.3
Vitreloy 106a (Zr11)	$Zr_{58.5}Nb_{2.8}Cu_{15.6}Ni_{12.8}Al_{10}$	91*	1480	1.6*
Cast Vitreloy 106 [9]	$Zr_{57}Nb_{5}Cu_{15.4}Ni_{12.6}Al_{10}$	85	1800	2.5
ARLloy #1 (Hf02)	$Hf_{71.3}Cu_{16.2}Ni_{7.6}Ti_{2.2}Al_{2.6}$	97*	1660	2.0*
Cast [6]	$Hf_{52}Cu_{17.9}Ni_{14.6}Ti_{5}Al_{10}$	102.4	2150	<2.5

* Recall that the strain value was corrected by scaling the measured strain by a proportionality constant.

Empirical correlations have been made by Wang [92] between the mechanical properties, such as the modulus, Vickers microhardness and fracture strengths using data from a large variety of amorphous metal alloys. The data used to make correlations between the modulus and the Vickers microhardness and the modulus and the fracture strength are given in Figure 5.4 and 5.5.

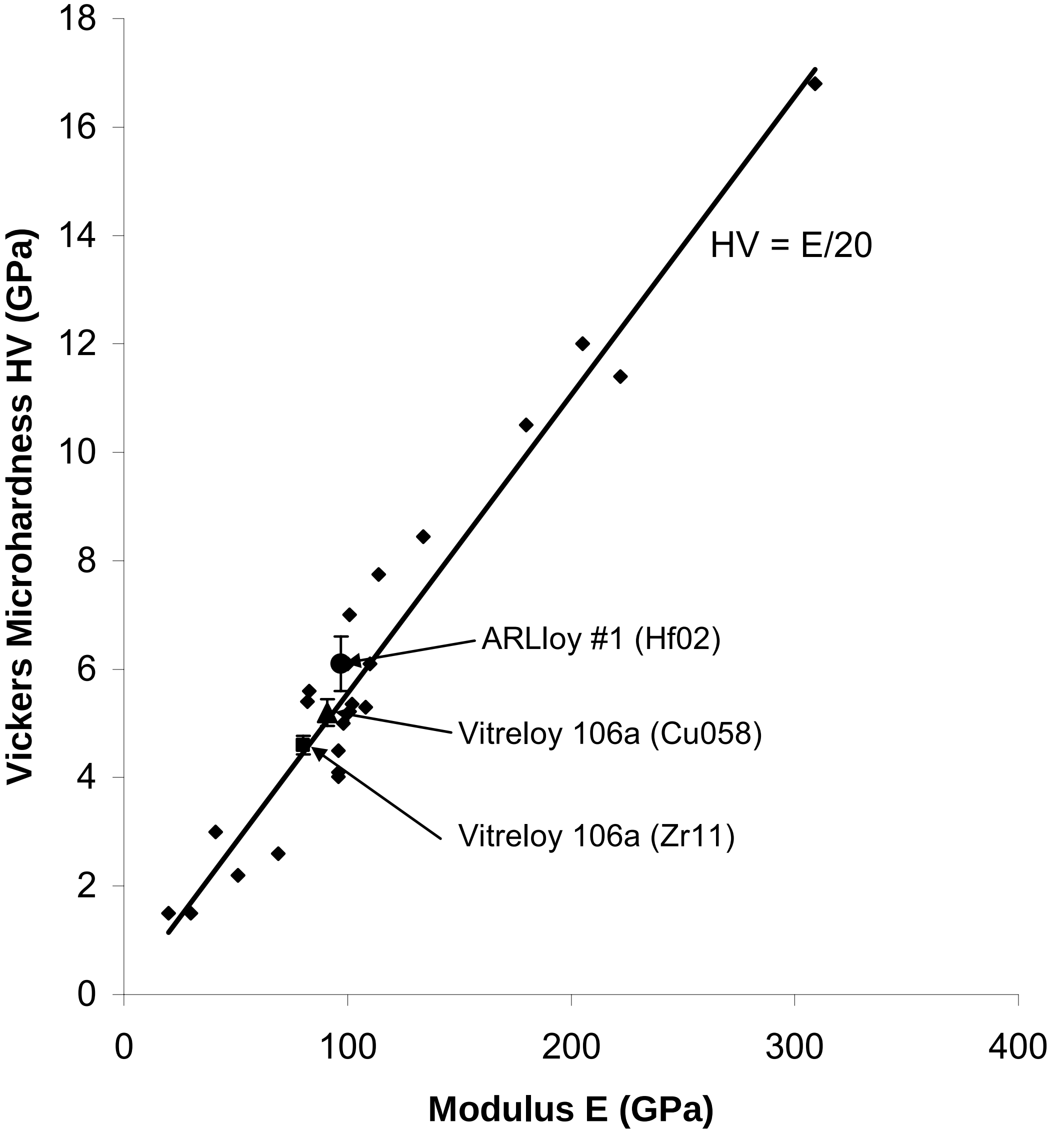

Figure 5.4 Correlation of the Vickers microhardness with the elastic modulus constructed with data from a variety of metallic glasses [92]. The three ECAE consolidated materials fit the data well.

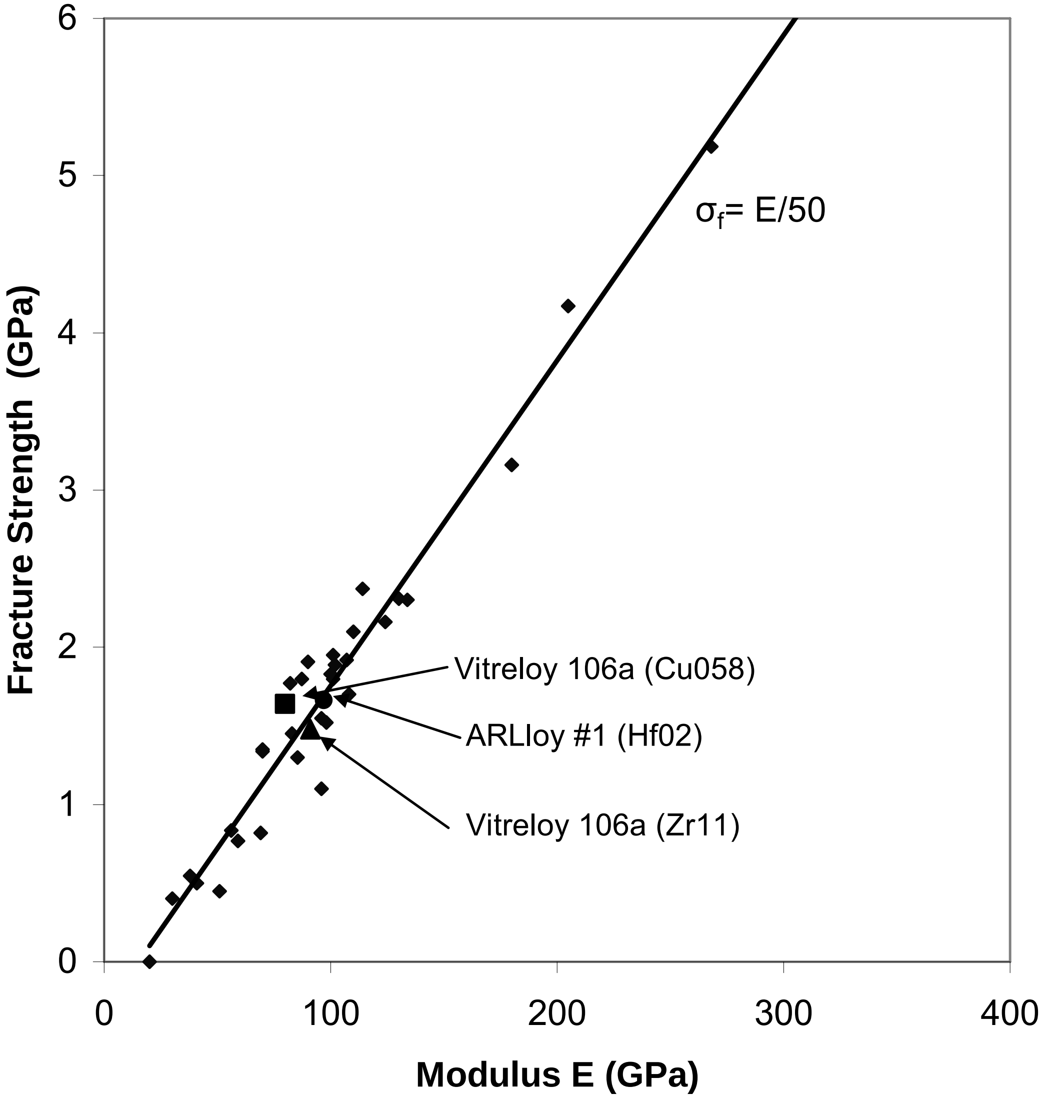

Figure 5.5 Correlation of the fracture strength with the elastic modulus constructed with data from a variety of metallic glasses [92]. The three ECAE consolidated materials fit the data well.

The good fit of the data from the ECAE consolidated BAMs with the empirical data obtained from other alloy systems points to fact that the properties are similar to cast materials and that HV = E/50 and σ_f = E/20 (with E in GPa) provide a reasonable correlations that can be used to predict mechanical properties in bulk metallic glasses.

5.3.2 Mechanical Properties of the Consolidated AMMCs

Two theoretical equations were given in Chapter II to predict the elastic moduli for composite materials. The rule of mixtures:

$$E_C = \sum \left(f_i E_i \right) = f_1 E_1 + f_2 E_2 + \cdots + f_n E_n \qquad (2.1)$$

where E is the elastic modulus of each component in the system, and another equation that determines the modulus of the composite using the constituent properties by Mital et al. [66]:

$$E_{pc} = \frac{V_f^{0.67} E_b}{1 - V_f^{0.33} \left(1 - \frac{E_b}{E_p} \right)} + (1 - V_f^{0.67}) E_b \qquad (2.2)$$

where V_f is the volume fraction particles, and E_{pc}, E_b and E_p are the normal moduli of the particulate composite, binder (matrix) and particles, respectively. Table 5.6 presents the measured elastic moduli for the AMMCs fabricated by ECAE and compares them to the theoretical values predicted by Equations 2.1 and 2.2. Curiously, the moduli of the samples tested in tension (recall that these failed prematurely (Figure 4.16)) show a much better correlation with the predicted values than those in compression, and the fit seems better for the equations developed by Mital et al. The moduli of the samples from billet Zr12 and Hf08 tested in compression are very similar to those of the amorphous matrix phase. This issue will be revisited in the next section which will deal with bonding and plasticity issues.

Table 5.6 Elastic modulus values obtained for Vitreloy 106a and ARLloy #1 AMMCs and predicted values using Equations 2.1 and 2.2.

Sample	Loading	Vol % W	Measured E (GPa)	RoM E (GPa)	Mital E (GPa)
Vitreloy 106a (Zr11)	---	---	91*	---	---
Vitreloy 106a (Zr04)	Tension	50%	159	245	182
Vitreloy 106a (Zr07)	Tension	60%	205	276	212
Vitreloy 106a (Zr07)	Compression	60%	206	276	212
Vitreloy 106a (Zr12)	Compression	60%	94*	276	212
ARLloy #1 (Hf02)	---	---	97*	---	---
ARLloy #1 (Hf08)	Compression	60%	71*	279	219

* Recall that the strain value was corrected by scaling the measured strain by a proportionality constant.

Table 5.7 Summary of mechanical properties for consolidated Vitreloy 106a, matrix AMMCs and comparable alloys tested in compression.

Name/Sample	Composition (wt%)	Vol %W	E (GPa)	σ_f (MPa)	%EL (%
Vitreloy 106a (Zr07)	$Zr_{58.5}Nb_{2.8}Cu_{15.6}Ni_{12.8}Al_{10}$	60	206	1540	1.9
Vitreloy 106a (Zr12)	$Zr_{58.5}Nb_{2.8}Cu_{15.6}Ni_{12.8}Al_{10}$	60	94*	1065	2.2*
Vitreloy 106 [9]	$Zr_{57}Nb_{5}Cu_{15.4}Ni_{12.6}Al_{10}$	80% wires	320	2150	16.2
Vitreloy 106 [9]	$Zr_{57}Nb_{5}Cu_{15.4}Ni_{12.6}Al_{10}$	15%	---	1960	7.0
ARLloy #1 (Hf08)	$Hf_{71.3}Cu_{16.2}Ni_{7.6}Ti_{2.2}Al_{2.6}$	60	71*	740	1.5*

* Recall that the strain value was corrected by scaling the measured strain by a proportionality constant.

Table 5.7 compares the properties of the Vitreloy 106a matrix composites fabricated by ECAE consolidation to similar AMMCs fabricated by other methods. There is no data published at this point which reports the properties of Hf-amorphous alloy matrix composites. When comparing the values of the AMMCs given in Table 5.6 to the properties of those presented in Table 5.4, it is observed that the cast Vitreloy 106 matrix AMMC's have a significantly higher ductility than the monolithic counterparts with the addition of a crystalline phase (16.2% with 80%W, 7.0% with 15%W and 2.5% without any reinforcement). This increased ductility is not seen in the ECAE consolidated materials, which, in case of the ARLloy#1 matrix, fail at a lower strain with the addition of the crystalline W, than without. While this is disappointing, it should be noted that the primary objective was not to increase the ductility, but to lend some plasticity to the composite with the addition of the crystalline phase. Figures 4.26 and 4.43 show that even though the material fails at a low strain, there is plastic deformation occurring during the compression loading. The next section will investigate the reasons for some of the peculiar stress-strain responses in the BAM and AMMCs, strength and nature of the bonds between the amorphous metal and crystalline phase, and the mechanisms of the enhanced plasticity observed in the W composites will be elucidated.

5.4 Mechanisms of Deformation, Bond Strength and Plasticity Issues in the Consolidates

5.4.1 Fracture and Deformed Surface Investigations

Examination of the fracture surfaces using light microscopy and SEM provides insight into the deformation behavior observed in the ECAE consolidated BAM and AMMCs, and the strength of the bond between the adjacent amorphous metal particles and of amorphous metal powers with the crystalline particulate reinforcement. The first issue that will be addressed is the early failure of consolidated Vitreloy 106a + 60vol% W tested in compression (Zr04 and Zr07) as seen if Figure 4.16. It was seen in Figure 5.1 that the agglomerated W pulls out of the matrix and causes stress concentrations that initiate the premature failure. But investigation of the flow plane fracture surface of the tensile test samples reveal that there is some substantial bonding occuring between the Vitreloy and W phase. Figure 5.6 shows that cracking does not occur along prior particle boundaries, but rather propagates through both Vitreloy 106a and W particles.

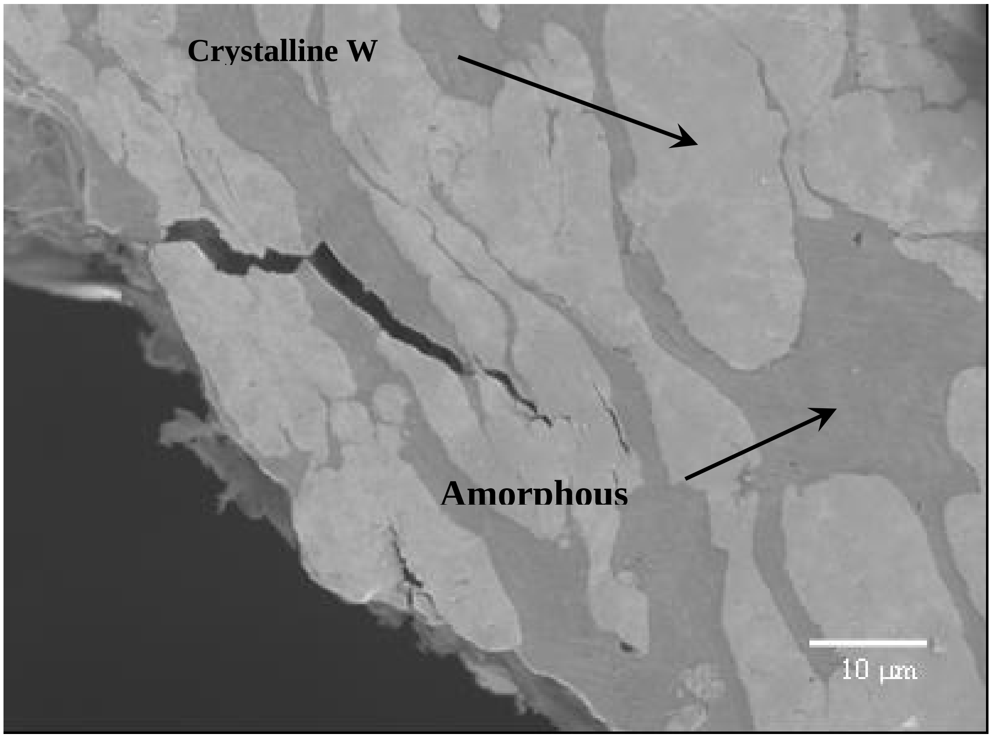

Figure 5.6 SEM image of a tensile test flow plane surface for Zr04 (50 vol.%W) after premature failure. The image shows regions where a crack has propagated through both the amorphous and crystalline phase, and not along particle boundaries, indicating that significant particle-to-particle bond strength has occurred in some regions of the AMMC.

The material loaded in compression (billet Zr07) does not suffer from the same susceptibility to void and stress concentrations. Overall, it appears that the majority of the failure occurs along prior particle boundaries (Figure 5.7) as evidenced by clear surface fracture patterns that match closely with the prior particle boundary morphology. Even so, some evidence of viscous flow in the amorphous phase and some good bonding between the amorphous and crystalline phases is observed in the 60%W compression test sample. Fracture through the amorphous phase is seen to be melt-like in nature (likely along a shear band) and flows around the W particles (Figure 5.8).

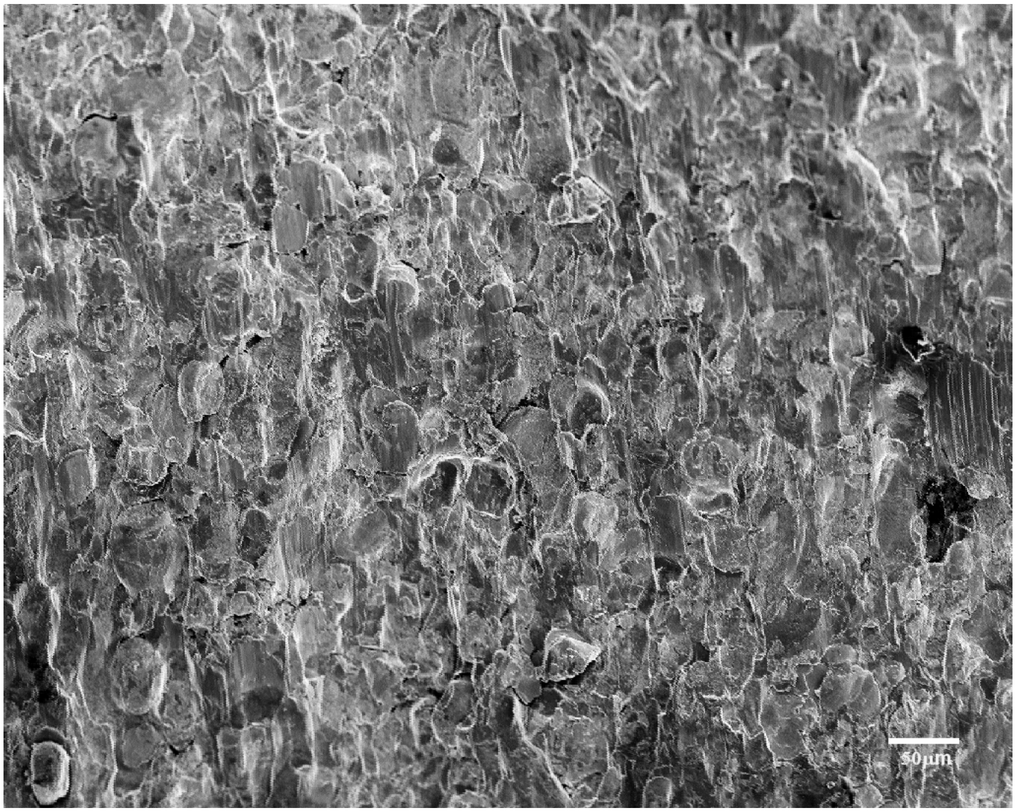

Figure 5.7 SEM image of a compression test fracture surface for billet Zr07 (60 vol.%W) showing that the majority of failures appear to occur along prior particle boundaries.

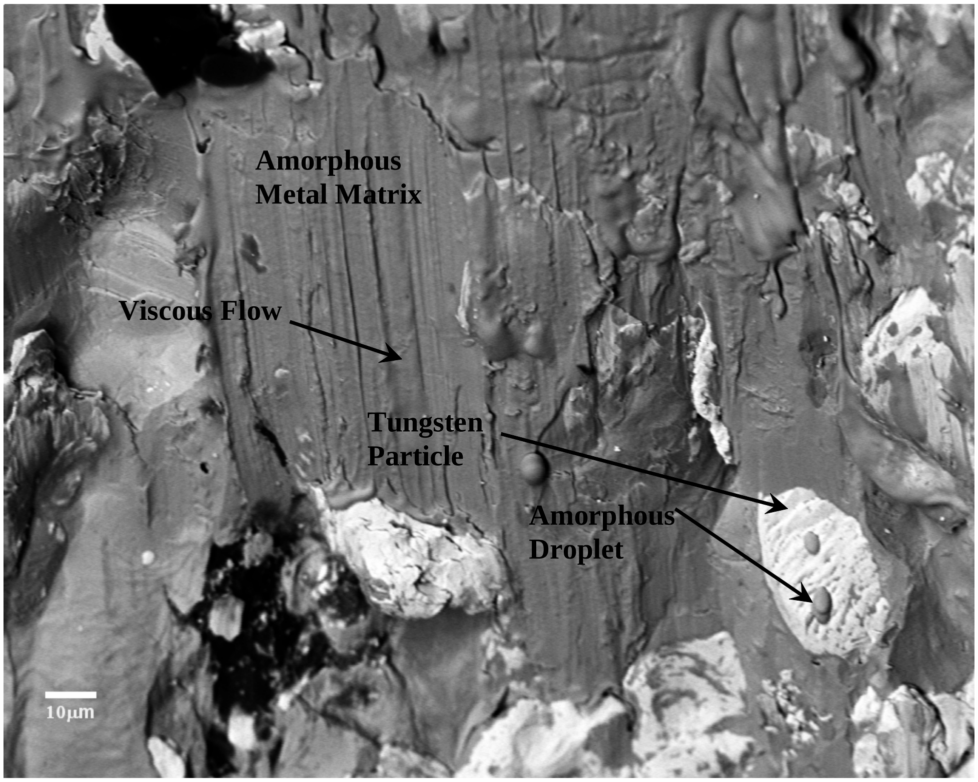

Figure 5.8 SEM image of a compression test fracture surface for billet 3 (60 vol.%W) showing localized melting and flow of the amorphous metal matrix.

Later extrusions used round tooling with better temperature control, clean and unagglomerated W powder, and slower extrusion rates. This improved consolidation environment results in few particle pull-outs and strong bonding between amorphous particles. Figures 5.9 and 5.10 show the fracture surfaces of consolidated Vitreloy 106a from billet Zr11. There are two regions of interest on this fracture surface: where the sample exhibits vein-like structures along a main shear band and localized shear bands parallel to the fracture plane (Figure 5.9) in the middle of the fracture surface, and along the front and back edge of the fracture surface where it appears that particles have separated (Figure 5.10).

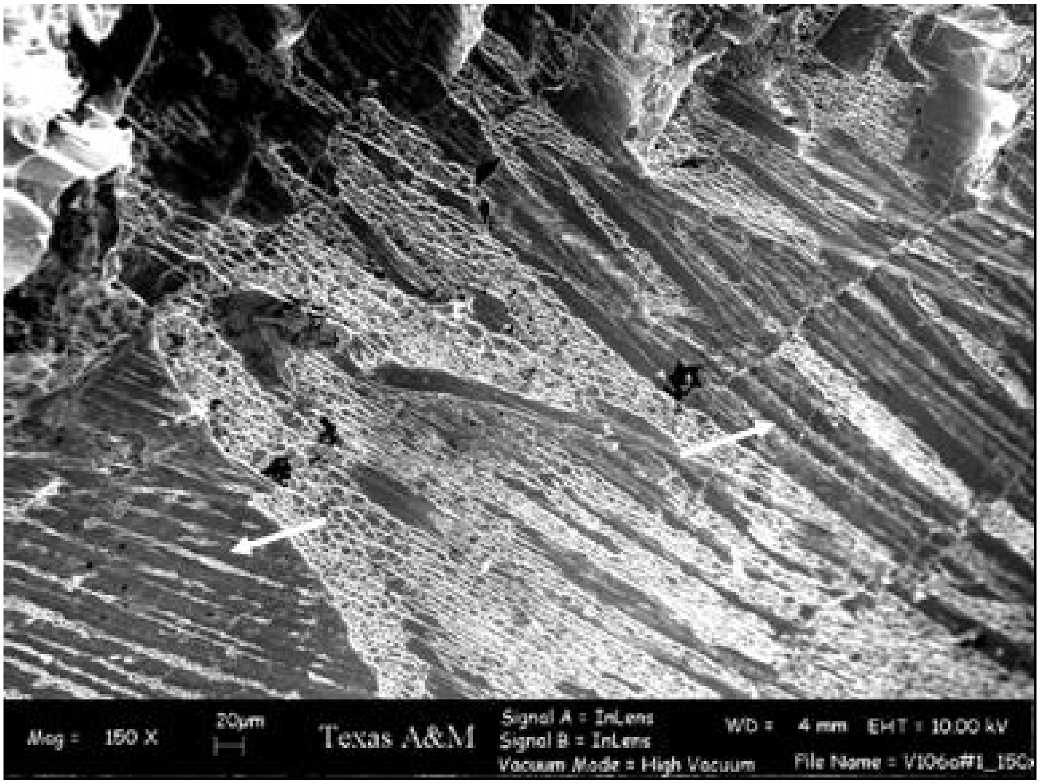

Figure 5.9 SEM image of a compression test fracture surface for Vitreloy 106a from billet Zr11. The surface is composed of vein structures along the direction of shear and shear bands parallel to the fracture plane (indicated by arrows).

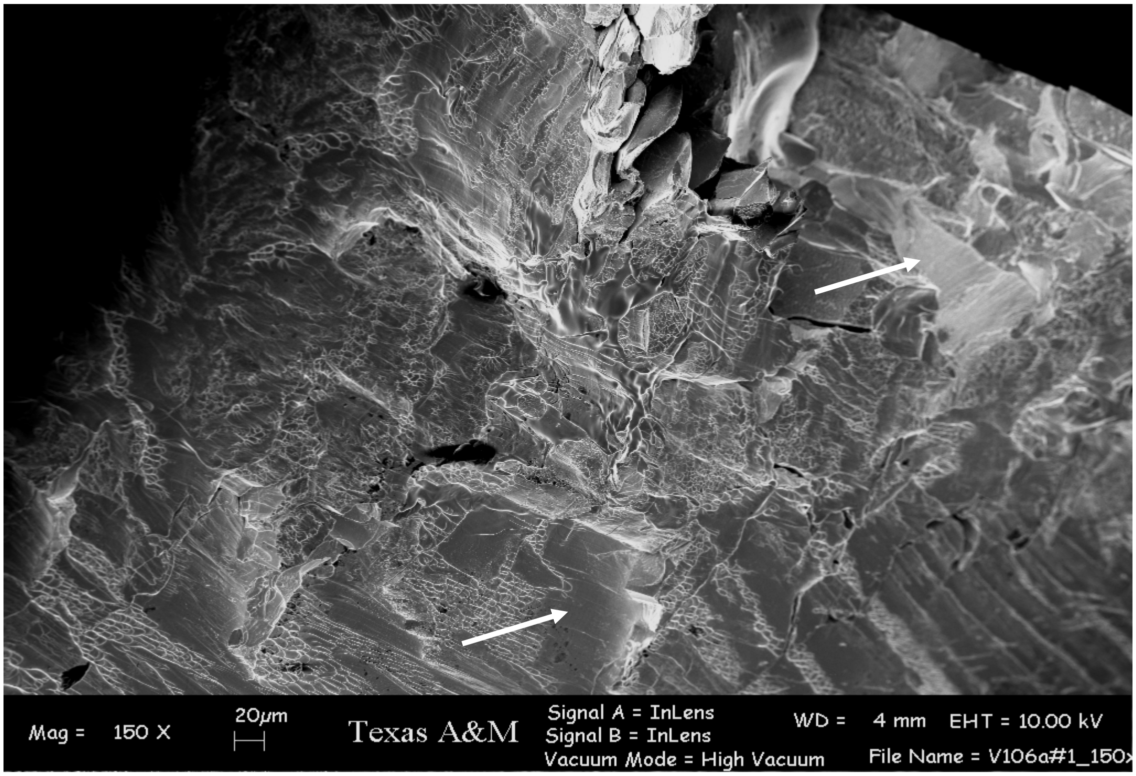

Figure 5.10 SEM image of a compression test fracture surface for Vitreloy 106a from billet Zr11. This region shows both vein-like patterns and smooth surfaces that appear to be unbonded regions (indicated by arrows).

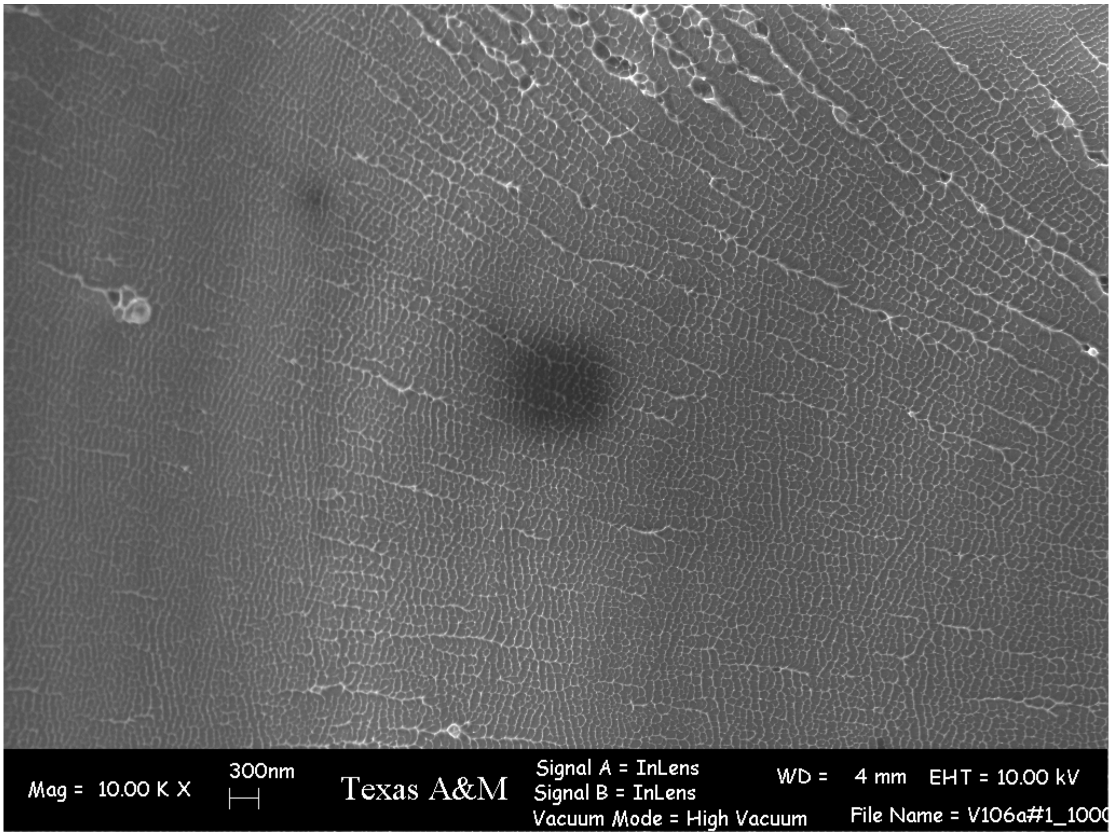

Figure 5.11 High resolution SEM image of the smooth fracture surface indicated by the white arrows in Figure 5.10. This appears to have the same vein-like patterns that are observed when the large scale sample fails along a catastrophic shear band.

High resolution SEM inspection of the smooth regions seen in Figure 5.10 are presented in Figure 5.11. The patterns seen on the surface have not been reported by other researchers for powder consolidated materials. The particle surfaces show a flow pattern very similar to the vein patterns that occur on shear bands due to localized melting and shear in one direction. It is theorized that these nanoscale vein patterns are the result of localized melting of the particle/particle bond during deformation. Figure 5.12 shows melt-like droplets that point to the fact that localized melting is occurring on the particle surface due to the high elastic energy of the fracture. The strength level achieved for this consolidated material (1480 MPa) and the similarity of the modulus to cast alloy (~91 MPa) would not be possible if there were not significant bonding of the particles.

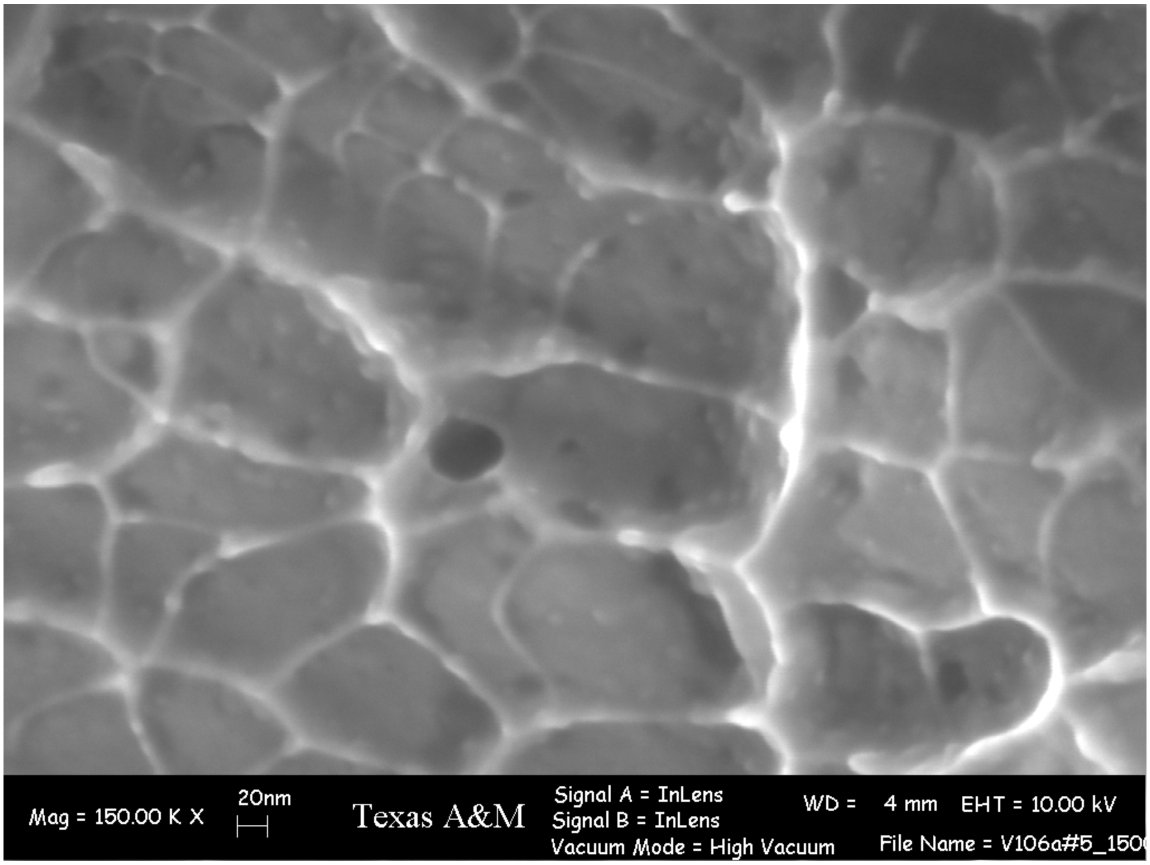

Figure 5.12 High resolution SEM image of the vein-like pattern seen in Figure 5.11. The molten drops on the surface ridges and the directional nature of the liquid point to localized melting on the surface during fracture and deformation.

It is hypothesized that there are essentially two mechanisms for deformation when the consolidated amorphous metal is loaded in compression. The first is the separation of amorphous metal particles along the edge of the sample, which is sometimes followed by the catastrophic failure along the major shear band. This failure is illustrated in Figure 5.13. As the compressive load is applied to the sample, the shear stress (τ_θ^c) dominates the fracture process and causes the particles at the edge to rapidly slide against each other (hence the localized melt patterns along the particle surface) and debond. This reduces the surface area that the compressive load is being applied on, which causes the catastrophic failure along a dominant shear band. During the whole process, the normal stresses (σ_θ^c) always apply a compressive stress to the fracture plane and therefore there are no tensile loads.

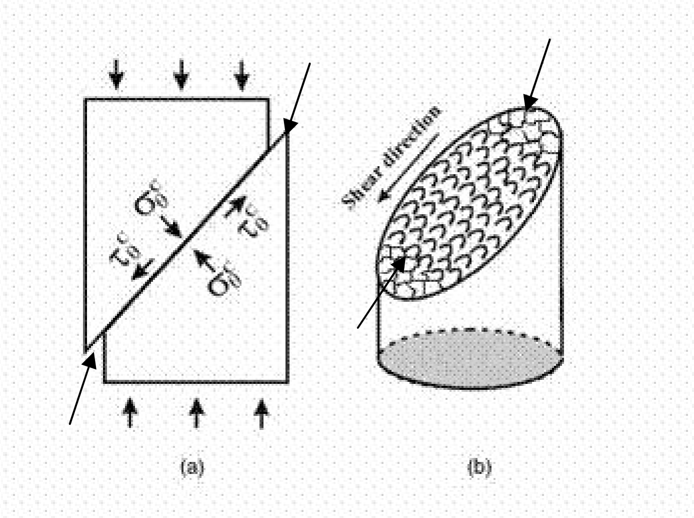

Figure 5.13 Illustration of the fracture process of a consolidated metallic glass under a compressive load. (a) is the shear fracture process and (b) is the general structure that forms. This image is a modified figure from [93]. Long black arrows indicate the initial failure region where the amorphous particles debond.

A similar effect takes place for the monolithic ARLloy #1 consolidated by ECAE (billet Hf02), except that failure never occurs along a catastrophic shear band, but rather

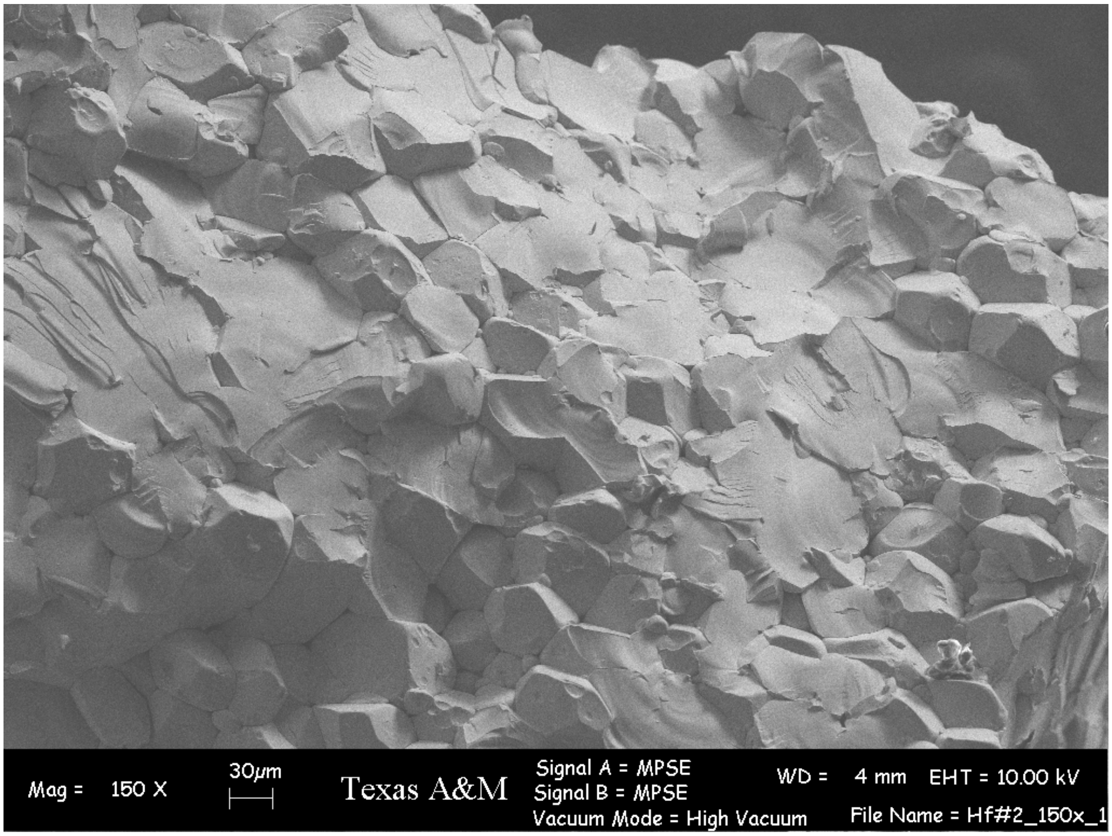

Figure 5.14 SEM image of a compression test fracture surface for ARLloy #1 from billet Hf02. The surface is composed smooth surfaces along prior particle boundaries and fairly unelongated/deformed particles.

by shearing/separation of the prior particle boundaries. Recall that for this particular sample, there was limited particle deformation during consolidation due to the Cu can being used, and there was a large amount of voids and porosity present. These factors likely limited the strength of the consolidated alloy by decreasing the bonded surface area on the fracture plane of the sample. Also, remember the TTT boundary was crossed, and that partial devitrification could cause some of the bonding problems from the amorphous alloy crystallizing into stable crystalline intermetallic phases on the surface. Figure 5.14 shows the fracture surface for ARLloy #1 from billet Hf02. The fracture surface consists of undeformed particles that appear to not have bonded with the opposite surface. But this is not the case. High resolution SEM inspection of the smooth particle surfaces shows nanoscale melting and periodic shear banding associated with good bonding (Figures 5.15). In this case, the shear stress does not reach a level that causes rapid failure on one shear band as was the case with the Vitreloy 106a, but be

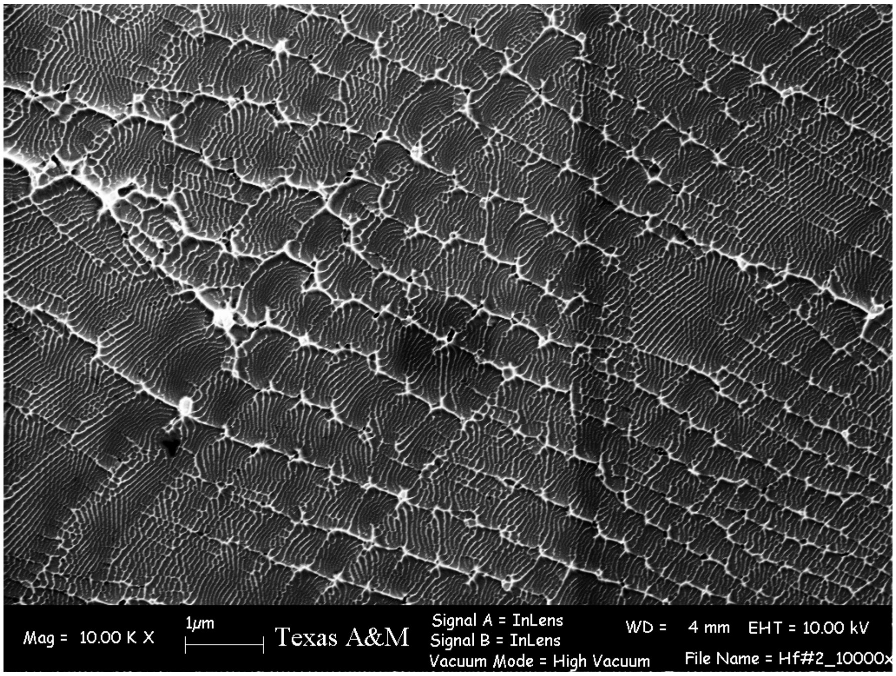

Figure 5.15 High resolution SEM image of the smooth particle surface on ARLloy #1 (Hf02) indicative of localized melting of the particle to particle bond.

reminded that the Cu can offered minimal bonding surface area to the particles and large void fractions. Even with this being the case, is noted that strengths of 1660 MPa and moduli comparable to the cast alloy (~97GPa) would not be achieved without significant bond strength between the amorphous particles.

It has now been established that the Vitreloy 106a and ARLloy #1 can form significant bond strengths with each other, and that deformation and fracture can occur in multiple modes. With this in mind we will move on to the AMMCs fabricated with these amorphous alloys as the matrix material. The fracture surface for a Vitreloy 106a + 60vol% W (billet Zr12) composite is shown in Figure 5.16. A number of important observations can be made from this image. First, notice that the W separates easily from the Vitreloy 106a matrix. In fact, it is possible that there was little bond strength between the Vitreloy 106a and W particles, but rather the W particles were "trapped" by the contiguously bonded amorphous matrix. The high strength value (~1065 MPa) observed during the compression test is likely due to a mechanical bond as a result of mechanical interlocking. This effect is similar to that reported in Chapter II for W wires in an aluminum matrix.

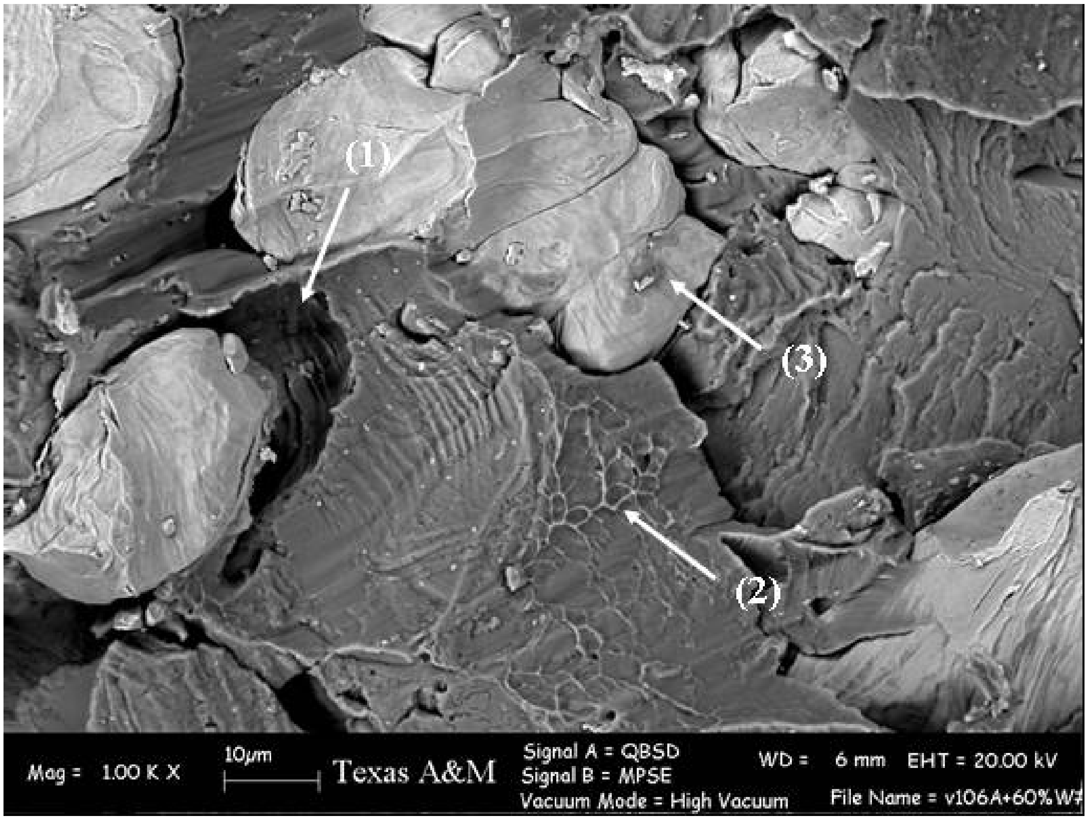

Figure 5.16 BSE SEM image of the fracture surface of ECAE consolidated Vitreloy 106a + 60 vol.%W (billet Zr12). A number of features are noted on the surface: (1) W particles easily separate from the matrix. (2) Localized melting occurs during fracture, which verifies the amorphous matrix bond strength. (3) There is little change in the morphology of the W particle after extrusion or compression testing.

Another observation is that localized melting occurs on the fracture surface of the Vitreloy 106a amorphous matrix. This is evidence that bonding occurs in the matrix which is not quite contiguous because of the low volume fraction of AMMC. Also, there is little change in the shape of the W particles, which means that the majority of the plastic deformation is taking place in the amorphous matrix by shear band generation and interactions.

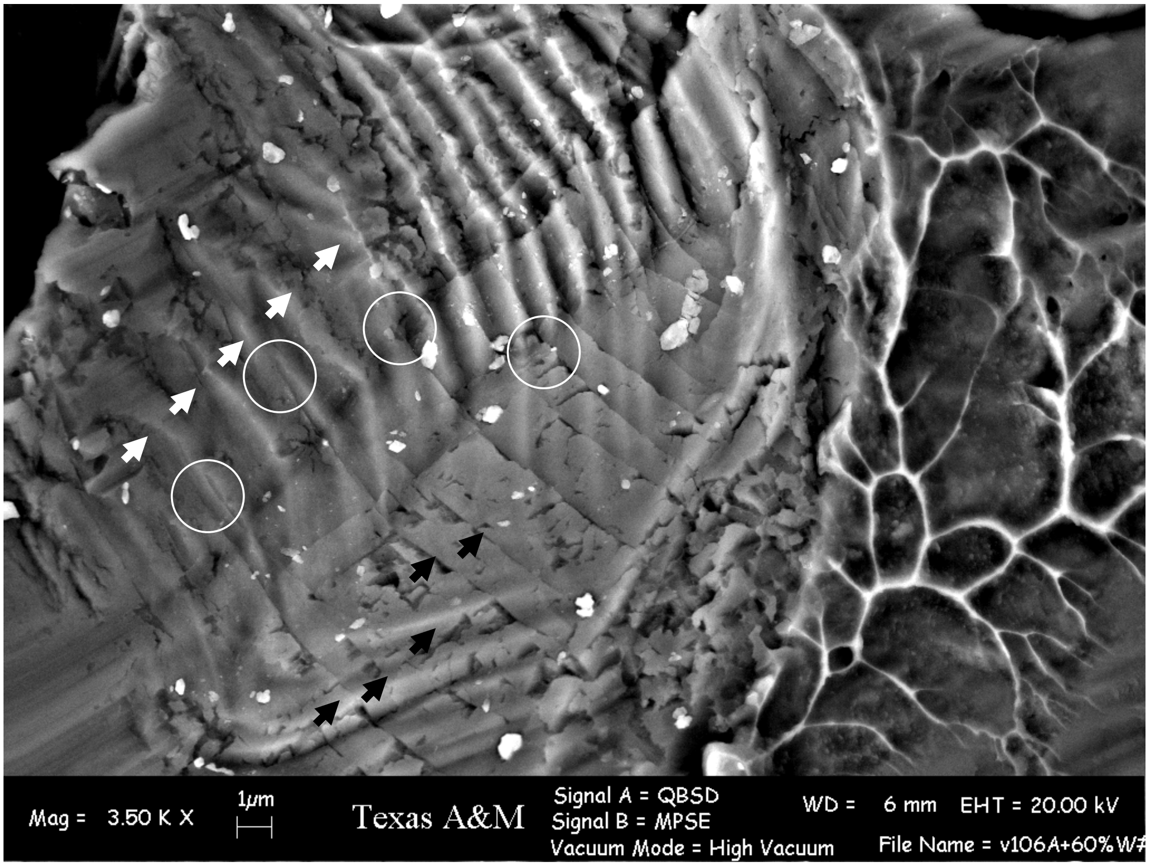

Figure 5.17 BSE SEM image of the shear band interactions on the fracture surface of ECAE consolidated Vitreloy 106a + 60 vol.%W (billet Zr12). One set of shear bands is indicated by white arrows, and the other by black arrows. Notice that the propagation of one set of shear bands ceases at an intersection with the first (shown with circles).

This can be clearly seen in Figure 5.17. Notice the shear bands on the surface where a particle has separated from the matrix. These are very similar to the shear bands that are generated from the edge of microhardness indentation in an amorphous alloy. The periodic nature of these shear bands reflects the many load drops and oscillations in the stress-strain curve as the sample is plastically deformed and shear banding occurs in the amorphous matrix [38]. A closer investigation of this region shows a set of secondary shear bands that have been generated during the deformation. These shear band intersect with the ridged shear bands and cease propagation. This phenomenon is theorized to be the predominant mechanism by which plasticity is enhanced in AMMCs.

BSE SEM images of the fracture surface for the ARLloy #1 + 60% W AMMC (billet Hf08) are shown in Figure 5.18. This material exhibited low strength (~740 MPa) and a low modulus (~71 MPa). Recall that this material was extruded slowly, and the TTT boundary was crossed, so partial devitrification likely occurred and thereby prevented effective bonding of the particles. Evidence for this behavior is seen in Figure 5.18. Like in the case of the Vitreloy 106a AMMC, there is separation between the matrix phase and the W. There also appears to be break-up and fragmentation of the W particles that likely occurs during the compression testing. These factors, along with the brittleness that comes with the partial devitrification, caused this sample to fail in a brittle manner with less plasticity than was seen for the Vitreloy matrix AMMC.

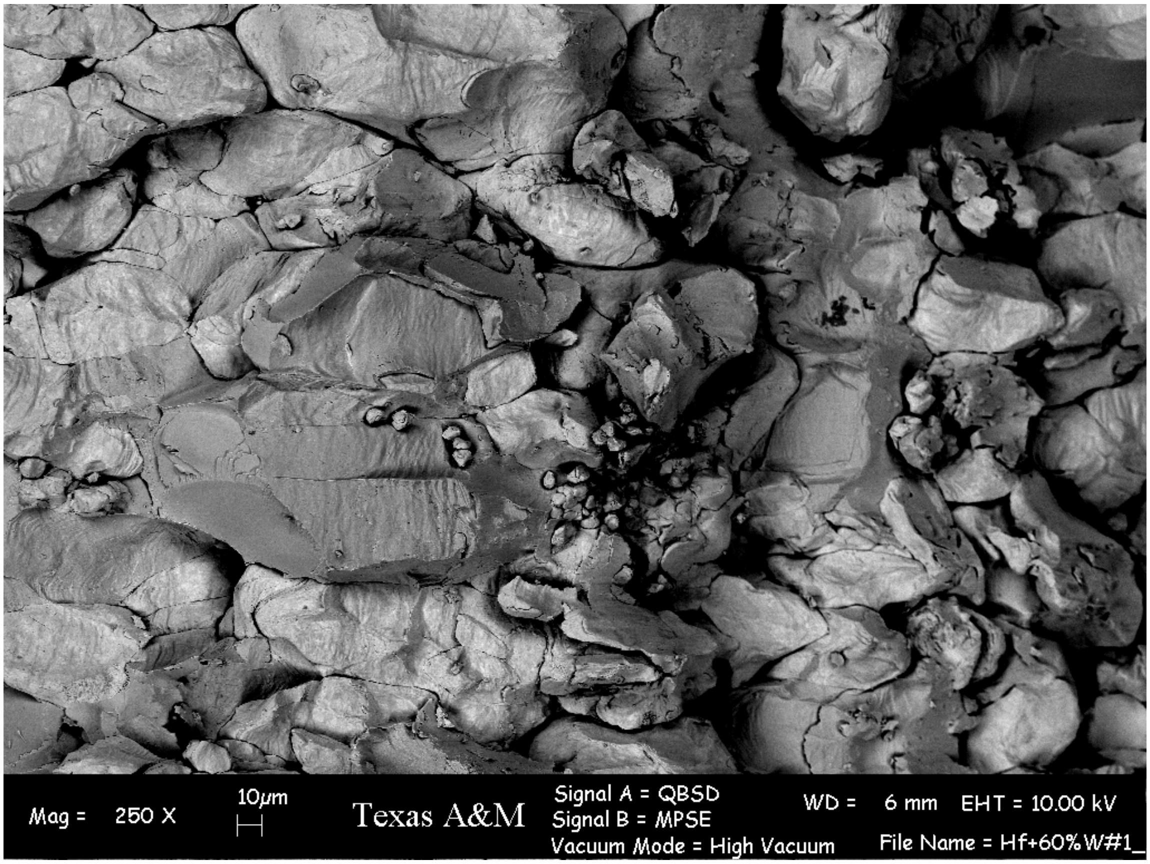

Figure 5.18 BSE SEM image of the fracture surface of ECAE consolidated ARLloy #1 + 60 vol.%W (billet Hf08). The W particles appear to have separated from the ARLloy #1 matrix and fragemented during the compression testing.

Recall that samples from billet Zr12 and Hf08, when exposed to a compression load, had a modulus of elasticity very close to that of the amorphous metal matrix. This contradicted the results seen in the tension and compression test for the AMMC from billets Zr04 and Zr07, whose values are in agreement with those given by the predictive equations (Table 5.5). But observe that in both Figures 5.16 and 5.18, that the W has clearly separated from the amorphous metal matrix, and does not appear to bond well with itself either. The predictive equations assume an ideal bond between the matrix and dispersed phase, which is clearly not the case for this sample, and therefore the modulus reflects the deformation behavior of the only phase that is deforming: the amorphous metal matrix. The fact that the moduli from tension and compression tests done on Zr04 and Zr07 show values close to those predicted is likely because the Ni-coating on the unagglomerated W particles did promote a stronger bond between not just the W particles, but the W particles and the Vitreloy 106a. As was discussed in section 5.1.3, the fact that Ni is a small atom, and has comparatively low activation energy for diffusion allows it to diffuse and bond well with itself and other atoms. The fact that metals such as Ni and Cu diffuse more readily and promote better bonding are reasonable assumptions why the Cu and Ni crystalline phase AMMC composites did not fail catastrophically in compression. Figures 5.19 to 5.22 give the polished flow plane microstructures for the Cu- and Ni- containing composites.

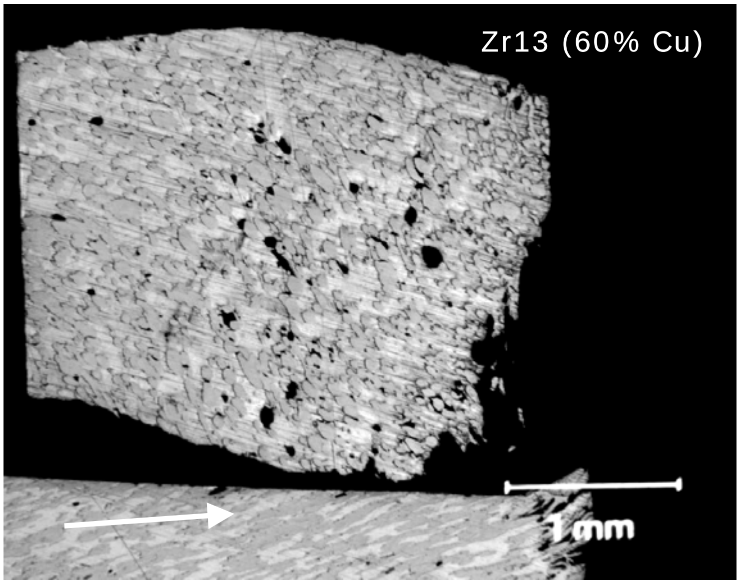

Figure 5.19 Light microscopy image of the flow plane surface of a deformed ECAE consolidated Vitreloy 106a + 60 vol.%Cu (billet Zr13) test. There is no deformation in the amorphous metal phase during the compression.

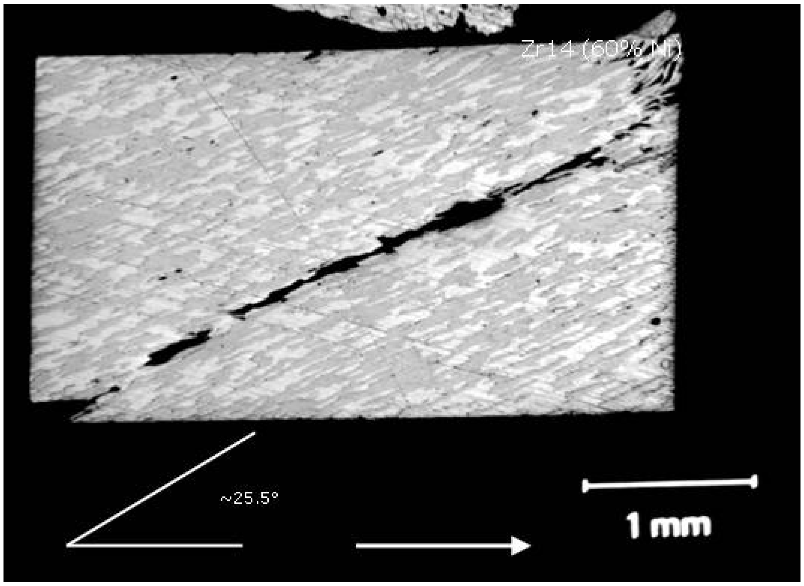

Figure 5.20 Light microscopy image of the flow plane surface of a deformed ECAE consolidated Vitreloy 106a + 60 vol.%Ni (billet Zr14) test sample. Deformation occurs on the ECAE shear plane at ~26°. Amorphous particles do not deform during compression.

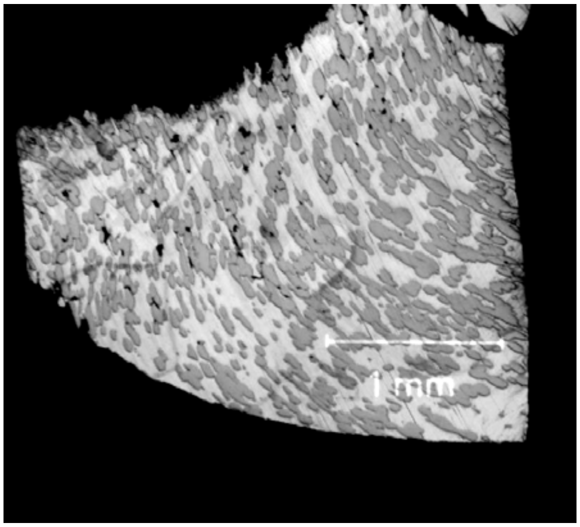

Figure 5.21 Light microscopy image of a near flow plane surface of a deformed ECAE consolidated ARLloy #1 + 60 vol.%Cu test. There is no deformation in the amorphous metal phase during the compression. Apparent amorphous particle deformation is due to out-of-plane bending of the sample followed by polishing.

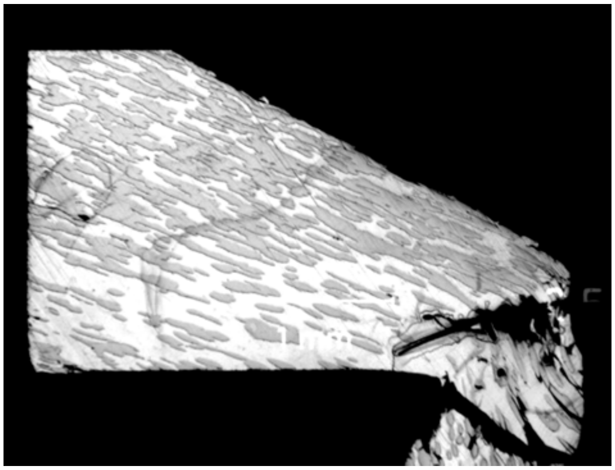

Figure 5.22 Light microscopy image of the flow plane surface of a deformed ECAE consolidated ARLloy #1 + 60 vol.%Ni test sample. Deformation occurs on the ECAE shear plane at ~26°. Amorphous particles do not deform during compression.

Figures 5.19-5.22 show that deformation takes place primarily in the crystalline phase during deformation and no shear bands or shear localizations were seen in the amorphous particles. The Ni-containing materials both failed on the ECAE shear plane by due to the Ni matrix debonding from itself. It is possible that by using multiple ECAE routes where an originally equiaxed element is returned to its initial equiaxed state that there would be additional mechanical interlocking that would prevent such failures from occurring.

A significant observation from these figures is that there was no indication of debonding between the amorphous metal phase and the crystalline Ni or Cu. The fact that Cu and Ni bond easily with the amorphous metal explain in part why other researchers have been successful in consolidating amorphous powders and crystalline particulate into AMMCs: the amorphous metal is based on Ni-[28,29] , Cu-[94-96], Mg-[97,98], Al- [99,100] or some other atom with an atomic radius favorable for migration and the crystalline phase is composed of either small ceramic reinforcements in low volume fractions, or metals or alloys that also can easily migrate to form a bond. The issues involved in consolidating W with amorphous metals with large component atoms (such as Zr and Hf) have been presented, and presented many challenges, but for the most part, these hurdles were overcome, and some level of success was achieved. It is hoped that the work presented here will provide a better understanding of issues involved with ECAE powder consolidation and specifically, give a better understanding of the processing/property/microstructure relationships in BAM and AMMCs produced by severe plastic deformation.

CHAPTER VI

SUMMARY AND CONCLUSIONS

Bulk amorphous metal (BAM) and amorphous metal matrix composites (AMMCs) were produced via ECAE consolidation of Vitreloy 106a ($Zr_{58.5}Nb_{2.8}Cu_{15.6}Ni_{12.8}Al_{10.3}$ -wt%), ARLloy #1 ($Hf_{71.3}Cu_{16.2}Ni_{7.6}Ti_{2.2}Al_{2.6}$ -wt%), and both of these amorphous alloys blended with crystalline phases of W, Cu and Ni. The results give a better understanding of the processing/property/microstructure relationships in BAM and AMMCs. Through instrumented extrusions and post-processing material characterization, an understanding of the role of ECAE processing parameters and powder characteristics on the consolidation performance and particularly interparticle bonding effectiveness has been developed. ECAE extrusion at temperatures within the supercooled liquid region gives near fully dense (>99%) mm-scale BAM and AMMCs. The properties of these consolidates are comparable to cast, melt-infiltrated, or conventionally consolidated materials. The ECAE processing is shown to promote strong bonds between amorphous particles due to the combined action of compaction and shearing. The addition of a crystalline phase is shown to increase the plasticity of the amorphous phase by serving as locations for generation and/or retardation of adiabatic shear bands. The major conclusions are summarized as follows:

1. Full consolidation of amorphous metal powder and amorphous metal composites can be accomplished with one ECAE extrusion pass at temperatures in the supercooled liquid region. Significant precursor particle deformation and strength are seen in the consolidated monolithic amorphous metal as a result of the combined compaction and shear associated with ECAE.

2. Thermal analysis by DSC shows the detrimental nature of oxygen to thermal processing of the amorphous phase at temperatures above T_g. Decreased oxygen contamination gives the benefits of a larger processing window, and a greater supercooled liquid region (ΔT). The added time and processing temperature range from the lower oxygen content aids in consolidation by allowing slower extrusions, which in turn causes less deformation related temperature rise during extrusion. More time for deformation processing also enables homogeneous material flow during consolidation, better bonding and allows the possibility of carrying out multiple extrusions if necessary.
3. Crystalline phase characteristics are critical to the bonding and desired properties in AMMCs. The particulates selected should be clean and unagglomerated. Crystalline particulate with small atomic radii (such as Cu, Ni, Mg, Al or Ti) and fragile, porous or unstable oxide (or hydrogen in some cases) layers will bond better with the amorphous metal matrix due to high mobility of such atoms in the glass transition region. Crystalline materials with larger atomic radii and/or stable dense oxide layers are more difficult to bond to an amorphous phase. The benefit of a surface coating (such as Ni with a thin oxide layer) improves the opportunities for bonding of such materials to not only each other, but the amorphous matrix.
4. Ideally, the amorphous metal used for the matrix phase in AMMCs should have not just a large supercooled liquid region, but needs to be thermally stable for a significant amount of time for slow extrusions. In addition, materials based on pure metals with large atomic sizes (e.g. the Zr- and Hf- based amorphous alloys investigated here) are more difficult to bond to than Cu-, Ni-, Al- or Mg- based

alloys because of the better characteristics with which small “mobile” atoms can diffuse and bond with adjacent crystalline or amorphous phases.

5. The selection of the proper encapsulation material influences the consolidation environment by the level of hydrostatic pressure that is induced, and the thermal conductivity during powder heat-up to the supercooled liquid temperature region. Selection of a material with a flow/yield stress which is higher than that of the amorphous alloy consolidates the powder to near full density after one extrusion. A lower flow/yield stress results in less particle deformation (i.e. less surface area of bonding) and voids in the consolidate. Selection of a can material with good thermal conductivity allows a more rapid heat up of the encapsulated powder to temperatures necessary for extrusion, and rapid cool down after consolidation, thereby decreasing the fime for devitrification.
6. Consolidation at temperatures low in the supercooled liquid temperature region, compared to processing at higher temperatures within the T_g-T_x region, only minimally influences particle deformation and infiltration around second phase particles. Higher temperatures can result in partial or full devitrification, especially if the amorphous alloy is not thermally stable, i.e. there is little time to the TTT boundary or the ΔT range is small. Therefore, processing should be done as low in the supercooled liquid region as possible to allow the largest time for consolidation.
7. The mechanical properties of monolithic amorphous metal and AMMCs consolidated by ECAE are measured to be slightly less than those obtained by casting and infiltration methods, and are also less than those predicted by empirical and theoretical models and equations. The difference in properties is due to non-

ideal (yet still fairly strong) bonding of the amorphous powders to themselves and little or no bonding with the uncoated crystalline particles. Improved properties from better particle-to-particle bonding are expected for amorphous metals and crystalline particulates with minimal surface oxide layers, and amorphous metals with large time-temperature processing regions.

8. Fracture surfaces of the monolithic consolidated amorphous metals demonstrate two failure mechanisms: debonding at the particle-to-particle boundary and fracture through particles. Both cases show evidence of localized melting and shear banding during fracture. The bond strength of the amorphous particle-to-particle bond shows high strength as evidenced by high fracture strengths of the consolidate.
9. Plasticity is enhanced in AMMCs by the addition of a dispersed crystalline phase. The enhanced plasticity is a result of shear bands and shear localization of the amorphous metal during deformation. These shear bands are started and/or stopped at the interface between the amorphous and crystalline phase. The ductility of the consolidate is also improved by a higher number of networked shear bands which is analogous to dislocation density giving a higher strength in crystalline metals. Therefore a smaller dispersion of the crystalline phase in a contiguous amorphous matrix would result in plasticity and higher ductility in the consolidate by the generation of a larger number of shear bands.

CHAPTER VII

SUGGESTIONS FOR FUTURE WORK

1. The effectiveness of using an amorphous powder with minimal oxide or surface coating has been demonstrated. These powders are notoriously difficult to manufacture, and require “closed” processing as in the work done by Inoue et al. Obtaining such powder for future experiments would undoubtedly provide better bonding and properties in the consolidated materials.

2. The initial motivation, to use a large volume fraction of crystalline phase, was driven by density issues related to kinetic energy penetrator applications, and the limited amount of amorphous powder fabricated. Since that time, our focus shifted away from density, and more to the realm of enhanced plasticity. As such, further experimentation should be done with a lower volume fraction of crystalline phase so as to ensure that the amorphous metal is contiguous.

3. The use of W as the crystalline phase was a result of a high density objective. Clearly other crystalline materials (in lower volume fractions) should bond better with the amorphous matrix and will likely have the same effects of shear band initiation and hindering. It is suggested that future work continue the idea of using Cu, Ni or even small ceramic particles as the reinforcement phase.

4. The flow stress of the can material was shown to have a significant effect on the consolidation and porosity of the extruded material. In theory, by using a thicker can wall in a material with a lower flow stress, a higher hydrostatic load can be induced. Cu and Ni cans should be fabricated with different wall thicknesses to examine this effect.

5. The small sample sizes used in the compression tests and metallography (2 mm x 2 mm x 4 mm) limited ideal examinations and testing. For future work, larger compression and tensile samples should be fabricated and EDM cut. This will allow more realistic characterizations for structural applications.

6. The idea of extrusion route should be reinvestigated for amorphous metal matrix composites where both phases have similar properties (such as the Vitreloy/ARLloy alloys + Ni). These samples failed along the ECAE shear plane. Incorporating routes such as route 2C will shift this plane away from the tension/compression shear plane, and should result in more homogenous, and likely better strength properties.

…

REFERENCES

[1] W.L. Johnson, Mat. Res. Soc. Symp. Proc., 554 (1999) 311.

[2] W.L. Johnson, JOM, 54 (2002) 40.

[3] C. A. Inoue, H.M. Kimura, K. Sasamori and T. Masumoto, Mater. Trans. JIM. 35 (1994) 85.

[4] C.C. Hays, C.P. Kim and W. L. Johnson, Phys. Rev. Lett. 84 (2000) 2901.

[5] K. Hashimoto, in: Current Topics in Amorphous Material Physics and Technology, Elsevier Science Publishers, New York, NY, (1993) 167.

[6] Bruck, H.A., Rosakis and A.J. Johnson, W.L., J. Mater. Res. 11 (1996) 503.

[7] W.L. Johnson, in: Current Opinions in Solid State and Materials Science, 1 (1996) 383.

[8] A. Inoue, Mater. Trans. JIM 36 (1995) 866.

[9] W.L. Johnson, Mater. Sci. Tech. 9 (1994) 94.

[10] A. Inoue, Acta Mat. 48 (2000) 279.

[11] R.D. Conner, R.B. Dandliker and W.L. Johnson, Acta. Mat., 46 (1998) 6089.

[12] L.Q. Xing, J. Eckert, L. Schultz, Nanost. Mater. 12 (1999) 503.

[13] H. Kato, T. Hirano, A. Matsuo, Y. Kawamura and A. Inoue, Scripta Met. 43 (2000) 503.

[14] C. Fan, R.T. Ott, and T.C. Hufnagel, Appl. Phys. Lett. 81 (2002) 6.

[15] R. Hasagawa, R.E. Hathaway and C.F. Chang, J. Appl. Phys. 57 (1985) 3566.

[16] Y. Kawamura and M. Takagi, Mater. Sci. Eng. 98 (1988) 415.

[17] S. Ishihara, W. Zhang and A. Inoue, Scripta Met. 47 (2002) 231.

[18] T. Itoi, T. Takamizawa, Y. Kawamura and A. Inoue, Scripta Met. 45 (2001) 1131.

[19] O. N. Senkov, D. B. Miracle, J. M. Scott and S. V. Senkova, J. Alloys and Compounds 365 (2004) 126.

[20] J. Robertson, J. -T. Im, I. Karaman, K. T. Hartwig and I. E. Anderson, J. Noncrys. Sol. 317 (2003) 144.

[21] I. Karaman, J. Robertson, J-T. Im, S.N. Mathaudhu, Z.P. Luo and K.T. Hartwig, Met. Mater. Trans. A. 35A (2004) 247.

[22] S.N. Mathaudhu, J.-T. Im, R.E. Barber, I.E. Anderson, I. Karaman, and K.T. Hartwig, Proceedings of the 2002 MRS Fall Meeting Symposium on Supercooled Liquids, Glass Transition, and Bulk Metallic Glasses, MRS, 754 (2003) 191.

[23] Y. Kawamura, H. Kato, and A. Inoue, Appl. Phys. Lett. 67 (1995) 2008.

[24] H. Kato, Y. Kawamura, A. Inoue and T. Masumoto, Mater. Sci. Eng A. 226-228 (1997) 458.

[25] S. Ishihara, W. Zhang and A. Inoue, Scripta Met. 47 (2002) 231.

[26] D. J. Sordelet, E. Rozhkova, M. F. Besser and M. J. Kramer, J. Noncrys. Sol. 317, 1-2 (2003) 137.

[27] T. Itoi, T. Takamizawa, Y. Kawamura and A. Inoue, Scripta Met. 45 (2001) 1131.

[28] D.H. Bae, M.H. Lee, D.H. Kim, and D.J. Sordelet, Appl. Phys. Lett. 83 (2003) 2312.

[29] M.H. Lee, D.H. Bae, W.T. Kim, D.H. Kim, E. Rozhkova, P.B. Wheelock and D.J. Sordelet, J. Noncrys. Sol. 315 (2003) 89.

[30] R.D. Conner, A.J. Rosakis, W.L. Johnson and D. Owen, Scripta Met. 37 (1997) 1373.

[31] C.J. Gilbert, R.O. Ritchie, and W.L. Johnson, Appl. Phys. Lett. 71 (1997) 476.

[32] P. Lowhaphandu and J.J. Lewandowski, Scripta Met. 38 (1998) 1811.

[33] C. Fan, C. Li, A. Inoue and V. Haas, Phys. Rev. B 61 (2000) 3761.

[34] C. Bertrand, L.Q. Qing, J.P. Dallas and M. Cornet, Mater, Sci. Eng. A. A241 (1998) 216.

[35] C. Fan and A. Inoue, Appl. Phys. Lett. 77 (2000) 46.

[36] C. A. Pampillo, J. Mater. Sci. 10 (1975) 1194.

[37] R.D. Conner, R.B. Dandliker and W.L. Johnson, Acta. Mat. 46 (1998) 6089.

[38] L.Q. Xing, J. Eckert, L. Schultz, Nanost. Mater. 12 (1999) 503.

[39] C.J. Gilbert, V. Schroeder, R.O. Ritchie, Bulk Metallic Glasses, W.L. Johnson et al. Eds., MRS Symp. Proc. 554 (1999) 343.

[40] W. M. Segal, V.I. Reznikov, A.E. Drbyshevskiy and V.L. Kopylov, Rus. Metall. Engl. Trans., 1 (1981) 115.

[41] V. M. Segal, Mat. Sci. Eng. A. A197 (1995) 157.

[42] R.Z. Valiev, R.K. Islamgaliev and I.V. Alexandrov, Prog. Mater. Sci. 45 (2000) 103.

[43] M. Furukawa, Z. Horita, M. Nemoto and T.G. Langdon, J. Mater. Sci. 36 (2001) 2835.

[44] L.R. Cornwell, K.T. Hartwig, R.E. Goforth and S.L Semiatin, Mater. Charact. 37 (1996) 295.

[45] W. Klement, R.H. Willens, P. Duwez, Nature, 187 (1960) 869.

[46] R.W. Cahn, in: Rapidly Solidified Alloys, H.H. Libermann, Ed., Marcel Dekker, New York (1993) 1.

[47] C. M. Atzmon, K.M. Unruh and W.L. Johnson, J. Appl. Phys. 58 (1985) 3865.

[48] G.J. Fan, W. Loser, S. Roth and J. Eckert, Acta Mat. 48 (2000), 3823.

[49] A. Peker and W.L. Johnson Appl. Phys. Lett. 63 (1993) 2342.

[50] S. Linderoth, N. H. Pryds, M. Ohnuma, A. S. Pedersen, M. Eldrup, N. Nishiyama and A. Inoue, Mater. Sci. Eng A. 304-306 (2001) 656.

[51] X. Wang, I. Yoshii, A. Inoue, Y.H. Kim, I.B. Kim, Mater Trans JIM 40 (1999) 1130.

[52] S. Yi, T.G. Park, D.H. Kim J. Mater. Res. 15 (2000) 2425.

[53] W. Zhang and A. Inoue, Appl. Phys. Lett. 80 (2002) 1610.

[54] T. Zhang, A Inoue and T. Masumoto, Mater. Lett. 15 (1993) 379.

[55] T. Zhang, A. Inoue, and T. Masumoto, Mater. Sci. Eng. A181/182 (1994) 1423.

[56] R.B. Dandliker, Bulk Metallic Glass Matrix Composites: Processing, Microstructure, and Application as a Kinetic Energy Penetrator, PhD Dissertation, California Institute of Technology, Pasadena, CA (1998).

[57] K. R. Cardoso, A. García Escorial, M. Lieblich and W. J. Botta F, Mater. Sci. Eng A. 315, 1-2 (2001) 89.

[58] E. Vasilyeva and V. Vystavkina, J. Magnetism and Mag. Mat. 267 (2003) 267.

[59] K. Amiya, N. Nishiyama, A. Inoue and T. Masumoto, Mater. Sci. Eng A. 179-180 (1994) 692.

[60] Y. Kawamura, H. Mano and A. Inoue, Scripta Met. 43 (2000) 1119.

[61] I. E. Anderson and R. L. Terpstra, Mater. Sci. Eng A. 326 (2002) 101.

[62] Y. Kawamura, H. Kato, A. Inoue and T. Masumoto, Int. J. Powder Metall. 33 (1997) 50.

[63] Y. Kawamura, H. Mano and A. Inoue, Scripta Met. 44 (2001) 1599.

[64] D.R. Askeland and P.P. Phule, in: The Science and Engineering of Materials, 5th ed., Thomson Publishers, Victoria, Australia (2006) 615.

[65] T.S. Srivatsan, T.S. Sudarshan and E.J. Lavernia, Prog. Mater. Sci. 39 (1995) 317.

[66] S.K. Mital, P.L.N. Murthy, and R.K. Goldberg, NASA Tech. Memo. 107279 (1996).

[67] L.J. Broutman and R.H. Krock, in: Composite Materials Vol 1: Interfaces in Metal Matrix Composites, A.G. Metcalfe Ed., Academic Press, New York (1974) 66.

[68] N. Chawla and K.K. Chawla in Metal Matrix Composites, Springer Science and Business Media, Inc., New York, (2006) 117.

[69] R.G. Hill, R.P. Nelson and C.L. Hellerich, in: Composites Work at Battelle-Northwest, Proc. of the 16th Refractory Metal Working Group Meeting, Pacific Northwest Laboratory, Seattle, WA (1969).

[70] N. Schlorke, B. Weiss, J. Eckert, L. Schultz, Nanost. Mater. 12 (1999) 127.

[71] A. Inoue, Mater. Sci. Eng. A. 304-306 (2001) 1.

[72] H. Choi-Yim, R.Busch, and W.L. Johnson, J. Appl. Phys. 83 (1998) 7993.

[73] H. Choi-Yim, R. Busch, U. Köster and W. L. Johnson, Acta Mat. 47 (1999) 2455.

[74] H. Choi-Yim, R. D. Conner, F. Szuecs and W. L. Johnson, Acta Mat. 50 (2002) 2737.

[75] H.Choi-Yim, R.D. Conner, F. Szuecs and W.L. Johnson, Scripta Met. 45 (2001) 1039.

[76] H. Choi-Yim, J. Schroers and W.L. Johnson, Appl. Phys. Lett. 80 (2002) 1906.

[77] S. Deledda, J. Eckert and L. Schultz, Scripta Met, 46 (2002) 31.

[78] R.M. German in: Powder Metallurgy of Iron and Steel, Wiley Interscience Publications, New York (1998) 29.

[79] R.Z. Valiev, A.V. Kornikov, R.R. Mulykov, Mater. Sci. Eng. A. A168 (1993) 141.

[80] V.M. Segal, Mater. Sci. Eng. A A271 (1999) 322.

[81] K.T. Hartwig, H. Zapata, A. Parasiris and S.N. Mathaudhu, in: Powder Materials: Current Research and Practices, TMS Publishing, Warrendale, PA (2001) 211.

[82] K.T. Hartwig, G. Chase and J. Belan, IEEE Trans. Appl. Supercond. 13 (2003) 3548.

[83] A. Parasiris, K. T. Hartwig and M. N. Srinivasan, Scripta Met. 42 (2000) 875.

[84] A. Parasiris and K. T. Hartwig, Int. J. Refract. and Hard Metals. 18 (2000) 23.

[85] M. Haouaoui, I. Karaman, H. J. Maier, and K.T. Hartwig, Met Trans. A. in press.

[86] Y. Kawamura, H. Kato, A. Inoue and T Masumoto, Mat. Sci. Eng. A. A219 (1996) 39.

[87] U. Geyer, A. Rehmet and S. Schneider in: Bulk Metallic Glasses, W.L. Johnson, A. Inoue and C.T. Liu, Eds., Materials Research Society, Warrendale, PA (1999) 275.

[88] X. Gu, L.Q. Xing and T.C. Hufnagel, J. Non-Crys. Solids 311 (2002) 77.

[89] X. Gu, T. Jiao, L.J. Kecskes, R.H. Woodman, C. Fan, K.T. Ramesh and T.C. Hufnagel, J. Non-Crys. Solids 317 (2003) 112.

[90] Y. Kawamura, A. Inoue and T. Masumoto, Scripta Met. 29 (1993) 25.

[91] A.L. Greer, Nature 366 (1993) 303.

[92] W.H. Wang, J. Non-Crys. Solids 351 (2005) 1481.

[93] Z.F. Zhang, J. Eckert and L. Schultz, Acta Mat. 51 (2003) 1167.

[94] S.-Y. Lee, T.S. Kim, J.K. Lee, H.J. Kim, D.H. Kim and J.C. Bae, Intermetallics 14 (2006) 1000.

[95] T.S. Kim, J.K. Lee, H.J. Kim, J.C. Bae, Mat. Sci. Eng. A. A402 (2005) 228.

[96] H.J. Kim, J.K. Lee, S.Y. Shin, H.G. Jeong, D.H. Kim and J.C. Bae, Intermetallics 12 (2005) 1109.

[97] Y.K. Xu, H. Ma, J. Xu, E. Ma, Acta Mat. 53 (2005) 1857.

[98] A. Kato, T. Suganuma, H. Horikiri, Y. Kawamura, A. Inoue and T. Masumoto Mat. Sci. Eng. A. A197-A180 (1994) 112.

[99] Y. Kawamura, A. Inoue, K. Sasamori and T. Masumoto, Mat. Sci. Eng. A. A181-A182 (1994) 1174.

[100] O.N. Senkov, S.V. Senkova, J.M. Scott and D.B. Miracle, Mat. Sci. Eng. A. A393 (2005) 12.

VITA

Suveen Nigel Mathaudhu was born in Takoma Park, Maryland. He was the first born son of Mr. Sukhdev Mathaudhu and Mrs. Veena Mathaudhu. He attended elementary and high school in Riverside, CA. He earned his Bachelor of Science degree in mechanical engineering in June 1998 from Walla Walla College, Walla Walla, WA. In order to pursue a Master of Science degree, he enrolled in Texas A&M University, College Station, TX in the fall of 1998. He earned his Master of Science degree in mechanical engineering in December 2001 from Texas A&M University, specializing in the area of materials science. Suveen pursued a Ph.D degree immediately following receiving his M.S. degree, again under Dr. K.T. Hartwig and received his Ph.D degree in August 2006.

His permanent address is:

Suveen Mathaudhu

5394 College Ave.

Riverside, CA, 92505

USA